



Circuits and Systems

Mekelweg 4,
2628 CD Delft
The Netherlands
<http://ens.ewi.tudelft.nl/>

BME-2019

M.Sc. Thesis

Investigating brain function and anatomy through ICA-based functional ultrasound imaging

Mandani Ntekouli

Abstract

Understanding the hidden organizational principles existing in the human brain was always one of the great challenges in Neuroscience. To uncover the way the brain functions, a new promising method, functional ultrasound (fUS) is used. fUS is capable of imaging even the microvasculature blood-flow dynamics in response to brain activation with high spatiotemporal resolution. The wealth of fUS-acquired data calls for advanced data-analytic methods to uncover new information, beyond the well-applied simple univariant correlation method. This is the main goal of this MSc thesis, to use a proper analysis technique, mainly borrowed from the same-principle functional magnetic resonance imaging (fMRI) technique, in order to produce powerful inferences. For this reason, a detailed literature review regarding fUS imaging and fMRI analysis methods is introduced. Then, the main analysis part is focused on the Independent Component Analysis (ICA) method, trying to segregate the brain into spatially independent components that share a similar activity response. The effectiveness of the methods is assessed based on the collected results on different datasets, obtained from 2D visual-stimulation as well as 3D resting-state experiments conducted on mice at the Neuroscience department of the Erasmus MC.

Investigating brain function and anatomy through ICA-based functional ultrasound imaging

THESIS

submitted in partial fulfillment of the
requirements for the degree of

MASTER OF SCIENCE

in

BIOMEDICAL ENGINEERING

by

Mandani Ntekouli
born in Athens, Greece

This work was performed in:

Circuits and Systems Group
Department of Microelectronics & Computer Engineering
Faculty of Electrical Engineering, Mathematics and Computer Science
Delft University of Technology



Delft University of Technology

Copyright © 2019 Circuits and Systems Group
All rights reserved.

DELFT UNIVERSITY OF TECHNOLOGY
DEPARTMENT OF
MICROELECTRONICS & COMPUTER ENGINEERING

The undersigned hereby certify that they have read and recommend to the Faculty of Electrical Engineering, Mathematics and Computer Science for acceptance a thesis entitled **“Investigating brain function and anatomy through ICA-based functional ultrasound imaging”** by **Mandani Ntekouli** in partial fulfillment of the requirements for the degree of **Master of Science**.

Dated: 11/12/2019

Chairman:

prof.dr.ir. G.J.T. Leus

Advisors:

dr. B. Hunyadi

dr.ir. M.A.P. Pertijs

Committee Members:

dr.ir. C. Strydis

dr.ir. P. Kruizinga

Abstract

Understanding the hidden organizational principles existing in the human brain was always one of the great challenges in Neuroscience. To uncover the way the brain functions, advancements in the fields of Medical Imaging and Computational Science have been of great importance. Powerful imaging tools, such as functional magnetic resonance imaging (fMRI) and positron emission tomography (PET), have already enabled scanning the whole brain volume and visualizing the brain functioning, both at rest and during task execution, to a significant degree. However, several limitations especially in spatiotemporal resolution led to the need for further advancements in the field of functional imaging. An alternative technique, that overcomes most of the previously existing problems, is functional ultrasound (fUS). fUS is capable of imaging even the microvasculature blood-flow dynamics in response to brain activation with high spatiotemporal resolution. The wealth of fUS-acquired data calls for advanced data-analytic methods to uncover new information, beyond the well-applied simple univariate correlation method. This is the main goal of this MSc thesis, to use a proper analysis technique, mainly borrowed from the same-principle fMRI technique, in order to produce powerful inferences. For this reason, a detailed literature review regarding fUS imaging and fMRI analysis methods is introduced. Then, the main analysis part is focused on the Independent Component Analysis (ICA) method, trying to segregate the brain into spatially independent components that share a similar activity response. Here, the whole processing pipeline is established, describing all the necessary preprocessing steps along with ICA parameters and approaches (single- and group-ICA) using the ICASSO software package. As a post-processing step, functional images-to-Allen brain atlas registration is also performed in order to identify the different regions represented in the ICA-derived spatial components. The effectiveness of the methods is assessed based on the collected results on different datasets, obtained from 2D visual-stimulation as well as 3D resting-state experiments conducted on mice at the Neuroscience department of the Erasmus MC. As a conclusion, ICA was able to separate different anatomical and functional sub-networks. More specifically, from the visual-stimulation experiments, brain regions such as Lateral geniculate nucleus (LGN) that play a role in the visual pathway are identified, while from the resting-state the spatial continuity of different regions is confirmed.

Acknowledgments

I would like to express my deepest gratitude to all the people who have become a big part of my studies.

I would first like to thank my thesis supervisor Christos Strydis for his guidance and detailed feedback throughout the entire period of my research, from internship to thesis. More importantly, Christos was the person who provided me the great opportunity to start my internship at the Neuroscience department of the Erasmus MC. There, I joined the CUBE team working on functional ultrasound. It was great working with the whole team during the last 1.5 years.

Moreover, I would like to thank my daily supervisors, Pieter Kruizinga and Bori Hunyadi. Pieter Kruizinga, as the expert of the fUS field at the Erasmus MC, helped me in all the time of my research. His insightful comments and encouragement were very useful, driving me to the right direction when needed. Then, Bori Hunyadi, my TU Delft supervisor, was involved in all aspects of my project from the literature review to the colloquium and to the thesis. I am gratefully indebted to her for her very valuable inputs and guidance during research and writing of this thesis.

Last but not least, I would like to express my gratitude to my family and friends. I would like to thank my parents and my sister whose love and support are with me in whatever I pursue. Also, special thanks to my good friends who were always there, physically or spiritually, for me throughout my years of study. We have shared a lot of moments of studying at the library, working together before deadlines, but also for all the fun we have had. This accomplishment would not have been possible without all of them.

Mandani Ntekouli
Delft, The Netherlands
11/12/2019

Contents

Abstract	v
Acknowledgments	vii
List of Figures	xi
List of Tables	xiii
List of Acronyms	xv
1 Introduction	1
1.1 Motivation and Problem Statement	1
1.2 Thesis Research Statement	3
1.2.1 Thesis Goal	4
1.3 Thesis Outline	4
2 Background	5
2.1 fUS	5
2.1.1 Physiological-Parameter Extraction	6
2.1.2 Fast fUS Processing	7
2.2 ICA Analysis Method	9
2.2.1 Introduction	9
2.2.2 Methodology	9
2.2.3 ICA Assumptions - Ambiguities	11
2.2.4 ICA Approaches	12
3 Related Work	15
3.1 Applications of fUS in Neuroscience	15
3.1.1 Research Use	15
3.1.2 Clinical Use	18
3.2 Literature Shortcomings in fUS-data Analysis	19
3.3 fMRI-data Analysis Methods	19
4 Materials and Methods	23
4.1 fUS Set-up and Imaging Parameters	23
4.2 Functional Experiments	23
4.2.1 Task-based Experiments	23
4.2.2 Resting-state Experiments	26
4.3 Overall Analysis Strategy	26

4.3.1	Input Data	26
4.3.2	Data Pre-processing	27
4.3.3	ICA Analysis	27
4.3.4	PDI-Atlas Registration	27
4.4	ICA Implementation	28
4.4.1	Preprocessing Steps	28
4.4.2	Processing Tools	30
4.4.3	Processing Algorithm	30
4.4.4	Number of Independent Components (ICs) – Model Order	32
4.4.5	Group-ICA	40
4.4.6	Post-processing Steps	42
5	Experimental Results	45
5.1	2D Visual-Stimulation Experiment	45
5.1.1	Single-ICA	46
5.1.2	Group-ICA	58
5.2	3D Resting-state Experiment	64
6	Conclusions	69
6.1	Thesis Overview	69
6.2	Scientific Contributions	71
6.3	Future Directions	72
A	Appendix	75
A.1	Gaussian Smoothing	75
A.2	Infomax Algorithm	76
A.3	Fast-ICA Methodology	77
A.4	Components Reliability	78
A.5	Components Reproducibility	78
B	Appendix	85
B.1	Correlation of components' time-series with the stimulus pattern	85
B.2	Group-ICA	86
B.3	Allen Brain Atlas Labels	88
B.4	Resting-state Experiment	89
	Bibliography	91

List of Figures

1.1	Main brain functional-imaging techniques	3
2.1	Doppler Principles	6
2.2	The processing procedure during conventional Doppler and μ Doppler modes	8
2.3	sICA model	11
2.4	Group-ICA Approaches	13
3.1	Examples of fUS processing	17
3.2	Comparison between GLM and sICA	21
4.1	Mean of PDI frames in the visual-stimulation experiment. The vasculature structure of a mouse brain is shown.	25
4.2	Mouse visual pathway	25
4.3	ICASSO: ICA spatial maps and their estimate clusters	35
4.4	Stability index (Iq) graph for each estimate-cluster	35
4.5	Components' Stability	36
4.6	Spatial and temporal correlation comparisons	37
4.7	Components' Stability for PCA	38
4.8	Spatial Correlation Coefficients for PCA	38
4.9	Datasets' Reproducibility	39
4.10	Spatial correlations between all the datasets	40
4.11	Atlas: structural slice and its annotated volume	42
4.12	Control Point Selection Tool user interface	43
4.13	PDI-Registered to Atlas	44
5.1	The seven interesting spatial maps	46
5.2	Shape of the brain after merging the components' maps	47
5.3	Spatial maps of Component 1	48
5.4	Spatial maps of Component 2	49
5.5	Spatial maps of Component 6	50
5.6	Spatial maps of Component 7	51
5.7	Spatial maps of Component 9	51
5.8	Spatial maps of Component 12	52
5.9	Spatial maps of Component 17	53
5.10	Shape of the brain after merging the labels' maps	53
5.11	Similarity matrix for single-ICA	54
5.12	Components' Task-relevance	56
5.13	Task-relevance-based ranking	56

5.14	LGN time-series	57
5.15	Stability-based ranking	58
5.16	Group-ICA common spatial maps	59
5.17	Correlation between single- and Group-ICA in the datasets	60
5.18	Group-ICA: Correlation of the time-series with the stimulus pattern	61
5.19	Group-ICA common spatial maps of the right-visual stimulation experiment	62
5.20	Correlation of the time-series with the stimulus pattern for all five datasets	62
5.21	Labels' similarity matrix in case of the first experiment	63
5.22	Labels' similarity matrix in case of the second experiment	64
5.23	Resting-state spatial maps of the 1st slice	65
5.24	Brain structure mapping of Slices 1 and 2	65
5.25	Reference Slice 4 and the corresponding ones of the adjacent slices .	67
5.26	Reference Slice 9 and the corresponding ones of the adjacent slices .	68
A.1	ICA components without smoothing	75
A.2	ICA components after being smoothed with a large Gaussian kernel	76
A.3	ICA components using the Infomax algorithm	77
A.4	Reliability: ICASSO-10	79
A.5	Reliability: ICASSO-15	79
A.6	Reliability: ICASSO-30	80
A.7	Reliability: ICASSO-50	80
A.8	Reliability: ICASSO-100	81
A.9	Reproducibility: Dataset 1	81
A.10	Reproducibility: Dataset 2	82
A.11	Reproducibility: Dataset 3	82
A.12	Reproducibility: Dataset 4	83
A.13	Reproducibility: Dataset 5	83
B.1	Temporal Correlation of the reference dataset with the stimulus pattern	85
B.2	Group-ICA: Back-reconstructed individual-specific maps (1)	86
B.3	Group-ICA: Back-reconstructed individual-specific maps (2)	87
B.4	Structure of Brain Labels Segmantation	88
B.5	Reliability values for the resting-state dataset	89

List of Tables

3.1	Published papers on fUS	16
3.2	Main methods used for fMRI methods	20
4.1	Summary of experiments and datasets employed in the current thesis.	26
5.1	Labels and names of Component 1	48
5.2	Labels and names of Component 2	49
5.3	Labels and names of Component 6	50
5.4	Labels and names of Component 7	51
5.5	Labels and names of Component 9	52
5.6	Labels and names of Component 12	52
5.7	Labels and names of Component 17	53
5.8	Acronyms of the interesting components	54
5.9	Correlation of the LGN of each dataset with the stimulus	57

List of Acronyms

AIC	Akaike's information criterion
ARA	Allen Mouse Brain Reference Atlas
BIC	Bayesian information criterion
BOLD	blood-oxygen level-dependent
CA	Ammon's horn
CBV	cerebral blood volume
CT	Computed Tomography
DCM	Dynamic Causal Modelling
DG	Dentate gyrus
EEG	Electroencephalographic activity
FCMA	Full correlation matrix analysis
FC	Functional-connectivity
fMRI	functional magnetic resonance imaging
fUS	functional ultrasound
FWHM	full width at half maximum
GCM	Granger Causality Mapping
GIFT	Group ICA Of fMRI Toolbox
GLM	General Linear Model
Hip	Hippocampal area
HRF	Hemodynamic response function
ICA	Independent Component Analysis
IC	Independent component
Iq	Cluster quality (stability) index
LAT	Lateral group of the dorsal thalamus
LD	Lateral dorsal nucleus of thalamus
LGd	Dorsal part of the lateral geniculate complex
LGN	Lateral Geniculate Nuclei
MDL	minimum description length
mfUS	mobile fUS

MVPA Multi-Voxel Pattern Analysis
NIRS Near Infrared Spectroscopy
NVC Neurovascular coupling
PCA Principal Component Analysis
PDI Power-doppler imaging
PET Positron Emission Tomography
PPI Psychophysiological interactions
PRF Pulse Repetition Frequency
PTLp Posterior parietal association areas
ROI Region of interest
rs-fMRI resting-state fMRI
RSNs Resting-state networks
RSPd Retrosplenial area, dorsal part
RSPv Retrosplenial area, ventral part
RSP Retrosplenial area
SC Superior Colliculus
SEM Structural Equation Modeling
sICA spatial Independent Component Analysis
SMs Spatial maps
SNR Signal-to-Noise Ratio
SPM Statistical Parametric Mapping
SSp-bfd Primary somatosensory area, barrel field
SSp-tr Primary somatosensory area, trunk
SSp Primary somatosensory area
SVD Singular Value Decomposition
TCs Time courses
tICA temporal Independent Component Analysis

The biological brain is a network consisting of a large number of different functionally and structurally interconnected regions. Each region has its own function, but they are all continuously communicating and sharing information with each other. Technological progress over the years has led to a plethora of computational methods and tools in the field of imaging that contributed to improved visualization of brain activity as well as to the inference of possible conclusions regarding its internal connections. These connections constitute one of the fundamental questions that neuroscientists are keen on investigating. In other words, they wish to explore where the brain is activated, its regions' interconnections and how these functionally connected brain regions interact with each other when triggered by executing a task or by a direct stimulus.

Despite the variety of imaging techniques currently available, in this work, a new promising method, functional ultrasound (fUS), will be presented as well as its large potential for unveiling neuronal activation and functional connectivity of spatially distributed brain regions.

1.1 Motivation and Problem Statement

Brain functional activation can be derived either directly by imaging the electrical activity of neurons (by using techniques like voltage-sensitive dyes, calcium imaging, electroencephalography mapping) or indirectly by detecting changes in blood flow [1]. These hemodynamic changes are known to be induced by neurovascular coupling, that is local perfusion alterations in the blood vessels located near the activated neurons in response to an increase in neuronal activity. This kind of information can be collected by methods of functional imaging. Some well-known methods used are functional magnetic resonance imaging (fMRI), positron emission tomography (PET), intrinsic optical imaging, photoacoustic imaging or near infrared spectroscopy (NIRS). In addition, more recently, the functional ultrasound (fUS) method (well-described by [2], [1], [3]) is capable of detecting and imaging the cerebral blood volume (CBV) over the entire brain area.

Methods based on optics provide the highest temporal resolution ($\sim 10ms$) and spatial resolution, ranging from some sub-millimeters, with intrinsic optical imaging, to micrometers with two-photon microscopy. However, optical methods come at the cost of removing an area of the skull in order for the light to penetrate tissue and these are only capable of investigating the cortex. On the contrary, methods

based on photo-acoustics can penetrate in a deeper level, but their penetration is still poor ($\sim 1mm$). Until recently, the only methods that could image the brain in a depth suitable to detect brain activation were fMRI and PET. PET uses injected radioactive and biologically active tracers, so to image brain molecular processes in three dimensions. Nevertheless, PET suffers from a poor spatial resolution and must be combined with a complementary anatomical imaging modality, such as MRI or Computed Tomography (CT).

The spatial-resolution issue is solved in case of fMRI. fMRI constitutes one of the most well-applied techniques inferring neuronal activation from an increase in the blood-oxygen level-dependent (BOLD) signal. The BOLD signal reflects inhomogeneities in the magnetic field due to changes in the level of blood oxygen, relying on the magnetization difference between oxy- and deoxy-haemoglobin in order to generate the fMRI signal.

Nevertheless, fMRI faces several limitations. Apart from the fact that it is quite expensive and also not applicable in several cases (e.g. in an operating theater to monitor the brain function), the issue of temporal resolution is of paramount importance. For instance, in research, for imaging small animals, high magnetic fields are needed to achieve high spatial resolutions in the order of $150 - 300\mu m$, but that comes at the cost of a substantial decrease in temporal resolution and/or Signal-to-Noise Ratio (SNR).

Another promising candidate that seems to have the potential to complement these existing techniques is functional ultrasound (fUS) [2], [1], [3]. Instead of using conventional Doppler ultrasound, fUS is preferred as its high frame rate improves the sensitivity and allows the imaging of smaller than the major cerebral arteries. Thus, it is a good, low cost, candidate for real-time and in-depth imaging of brain hemodynamic functions without the need for contrast agents. It is very crucial to capture the blood motion in these small vessel branches because in such depth motion is considered to be modulated by local neuronal activity, as further described in Chapter 2.

An illustration of the main brain functional imaging techniques¹ regarding temporal resolution, spatial resolution and portability is given in figure 1.1, taken from [5]. fUS appears to be in the center of the chart, addressing the shortcomings of fMRI and optical methods as well as whole-brain imaging and microscopy.

Furthermore, in order to acquire unique insights into brain functions and derive data-interpretation conclusions, the recorded data need to be processed using proper computational algorithms. Due to being in the early days of fUS-based brain imaging, it is assumed and investigated that algorithms could be borrowed from those that have already been implemented on fMRI pipelines, as the main principles remain the same. In this work, we started our exploration by adopting the Independent Component Analysis (ICA) method for trying to uncover new

¹Another intuitive classification has been given by [4] including several in vivo microvascular imaging techniques.

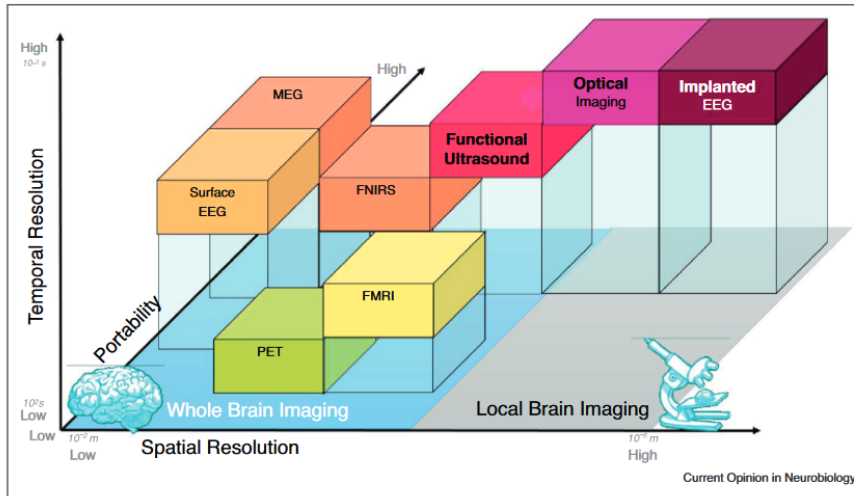


Figure 1.1: A comparison of the main brain functional-imaging techniques on a three-axis chart comparing temporal resolution, spatial resolution and portability. These techniques are also distinguished between whole-brain and localized-brain imaging [5].

information extracted from fUS data. In the absence of prior art and the novelty of the modality, we opted for ICA which (a) makes no prior assumptions on data structure and (b) has been successfully used in fMRI.

1.2 Thesis Research Statement

Due to the limited number of papers published on fUS for brain imaging, and the fact that their focus was mostly on examining its performance, this thesis addresses the current gap in the analysis of fUS data. This work requires research in multiple areas including fUS, fMRI and data-analysis methods making the selected topic very exploratory and multidisciplinary.

After extensive research work on all these areas, the current thesis is focused on the method of ICA decomposition. ICA is investigated, considering that it has already been used successfully in various fMRI applications in order to finally segregate the brain into different functional and anatomical components. In more detail, the whole processing pipeline for using the ICA algorithm is explored, configuring all the necessary preprocessing and ICA parameters. Then, its effectiveness is checked by inspecting the analysis results from multiple experiments, such as 2D visual-stimulation and 3D resting-state experiments. In the case of visual-input where five different datasets are available, firstly the reproducibility of the ICA components is checked. Secondly, the ICA findings are compared in space and time. The spatial components are assessed according to the atlas-based

anatomical regions, while the temporal components according to the ground-truth stimulus pattern. Finally, in the case of 3D resting-state dataset the ICA components are examined for their spatial continuity in adjacent brain slices.

1.2.1 Thesis Goal

The purpose of this thesis work can be summarized as follows:

“How can applying ICA on the microvasculature blood-flow information captured by fUS, can lead to conclusions regarding brain activations and deactivations and subsequently, help distinguish the different anatomical regions therein.”

1.3 Thesis Outline

The thesis work is organized in six chapters. Chapter 2 will give a theoretical background on some of the basic concepts that are used in this work. For instance, the physical principles of fUS and the proposed ICA data-analysis method are mainly described.

Chapter 3 includes a concise review on the existing research and clinical applications of fUS in Neuroscience.

Chapter 4 focuses on investigating the whole ICA processing pipeline that will be applied on fUS data. The appropriate preprocessing steps are established while the ICA optimal parameters are extensively explored.

Chapter 5 presents evaluation results of running ICA on different 2D and 3D datasets. The components extracted from both ICA and Group-ICA analysis are inspected as well as the decomposed brain regions are anatomically examined.

Finally, Section 6 concludes this work summarizing the experimental observations attained and proposes interesting topics to be explored in the future.

This chapter introduces all the essential concepts on which this work will be based. The main focuses of this work, fUS imaging method followed by the data-analysis ICA method, are presented. In more detail, fUS advantages, physical principles and processing procedure are described in Section 2.1, while the ICA methodology is presented in Section 2.2.

2.1 fUS

The fUS method relies on ultrafast power-Doppler imaging (PDI, producing the also called μ Doppler images) which gives the opportunity to detect blood flow in very small vessels in order to measure cerebral blood volume (CBV), or in other words the number of moving red blood cells in the sample volume. In power-Doppler imaging, we can take advantage of the Doppler frequency shift of the ultrasound wave caused by the moving red blood cells, shown in figure 2.1. Consequently, the measured signal power of the Doppler-shifted ultrasound is proportional to the volume of moving blood. In other words, an increase in blood volume locally induces a higher power of the Doppler-shifted ultrasound signal which is reflected from the larger number of moving erythrocytes (i.e. red blood cells) in the imaged microvasculature.

These changes in CBV are further associated with activated neurons in the specific area due to neurovascular coupling. The link between local neural activity and the resulting changes in the cerebral blood flow is defined as neurovascular coupling (NVC). This homeostatic physiological phenomenon assures the necessary blood supply in case of a metabolic demand, translated into increased neuronal activity in a specific area. Thus, through neurovascular control mechanisms, blood flow also increases in order to provide the essential amount of oxygen and nutrients to cover the energy needs of the local cells.

fUS is preferred over conventional Doppler ultrasound as it improves the sensitivity and it also allows the imaging of smaller than the major cerebral arteries. Thus, it is a good, low-cost, candidate for real-time and in-depth imaging of brain hemodynamic functions without the need for contrast agents. Penetrating even deeper into smaller branches of blood vessels provides us with more reliable data regarding the neurovascular-coupling phenomena, as the detection of smaller shift changes is more probable to be connected and modulated by neuronal activity.

In contrast to conventional ultrasound where focused beams are used, ultrafast

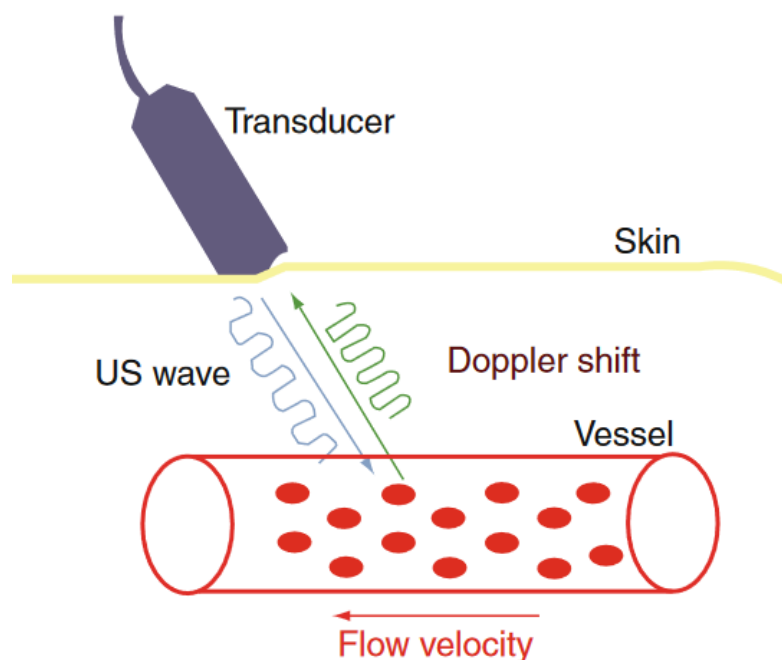


Figure 2.1: Doppler Principles: The probe transmits ultrasound waves and when these waves strike a moving structure (e.g. red blood cells), their frequency is shifted. The induced frequency shift is proportional to the velocity of the moving red blood cells. [6]

imaging can be performed by emitting a single plane-wave to the medium at a very high frame rate (firing rate), ranging from several hundred Hz up to around $38kHz$ depending on the imaging depth. The method of plane-wave imaging is used as the most efficient way to increase frame rate, at the expense of image contrast and spatial resolution.

In [2], a first experimental comparison between the PDIs obtained by fUS and conventional ultrasound is investigated on the rat brain. The tests showed that detection sensitivity increased by a factor of 47 in case of fUS, as the minimal intensity I_{Bmin} (minimum blood volume) that can be detected decreased by that factor. That value is proportional to noise intensity and inversely proportional to the number of sample images, which decreases and increases, respectively, in fUS tests.

2.1.1 Physiological-Parameter Extraction

In all functional-imaging modalities, being aware of which physiological parameter is measured, as well as its range and the assumptions made, is of paramount importance as that can facilitate the interpretation of the acquired data. The most relevant hemodynamic parameters that are usually reflected in a Doppler image

are blood volume, blood velocity, and flow direction. However, the association of these three parameters with the mean intensity of the Doppler signal which is measured in a PDI, is not trivial and is not taken into account.

Instead, and according to the literature, the values measured in power Doppler are proportional to cerebral blood volume (CBV), that is the number of moving RBCs in the sample volume. That concept is considered valid under the assumption that the hematocrit is constant in time and all the possible variations of RBC backscattering properties (e.g. shear rate - rate of velocity change) are ignored.

Furthermore, it should be clearly noted that there is a detection limit regarding the RBCs whose velocity can be detected. This limit exists because of the clutter filter that is used to reject the slow-moving tissue signal [7]. Thus, slow-moving RBC echoes are cut off as well. The detectable axial blood velocity is dependent on the applied filter. For instance, on that paper, for a 75Hz filter, the detectable velocity has to be higher than 4mm/s . As a result, blood inside capillaries, the smallest diameter vessels ($< 10\mu\text{m}$), is not detected by the $\mu\text{Doppler}$. Nevertheless, in some publications, it is reported that CBV in small arterioles is detectable. That fact is important because arterioles significantly contribute to the regulation of blood volume as a response to an activation at a fine local level.

That makes CBV a significant parameter to be captured for functional imaging. It is also already used by other modalities, such as intrinsic optical imaging or CBV-weighted fMRI (based on the vascular injection of iron oxide particles). As reported by [8], [9], CBV-based fMRI is often preferred to BOLD-fMRI in cases of small animal studies. The reason behind this is that the two measured signals originate in different parts of the vascular network. The CBV-weighted method is more sensitive to localize signals at feeding arterioles. There, the neurovascular coupling phenomena are more reflected according to many studies, like [10], as arteries and arterioles supply the essential nutrients to the activated neurons. Specifically, the proportion of CBV measured in arteries and veins is 3/1. On the contrary, the BOLD-based signal is mainly detected at venules and its arterial component can be diminished [11].

2.1.2 Fast fUS Processing

As already mentioned, ultrafast imaging can be performed by emitting only a single plane-wave pulse and scanning the whole field of view. However, the quality of the obtained image is quite low because the wave is not focused but spread in the whole scanning area. To overcome that limitation, the advanced fUS technique can give a solution by emitting a set of different-angled plane-waves. In that way, the frame rate is decreased by the number of angles in order to increase image contrast and resolution.

The main steps of the whole acquisition and processing procedure and the result of a PDI are illustrated in figure 2.2 and are followingly described. In the figure,

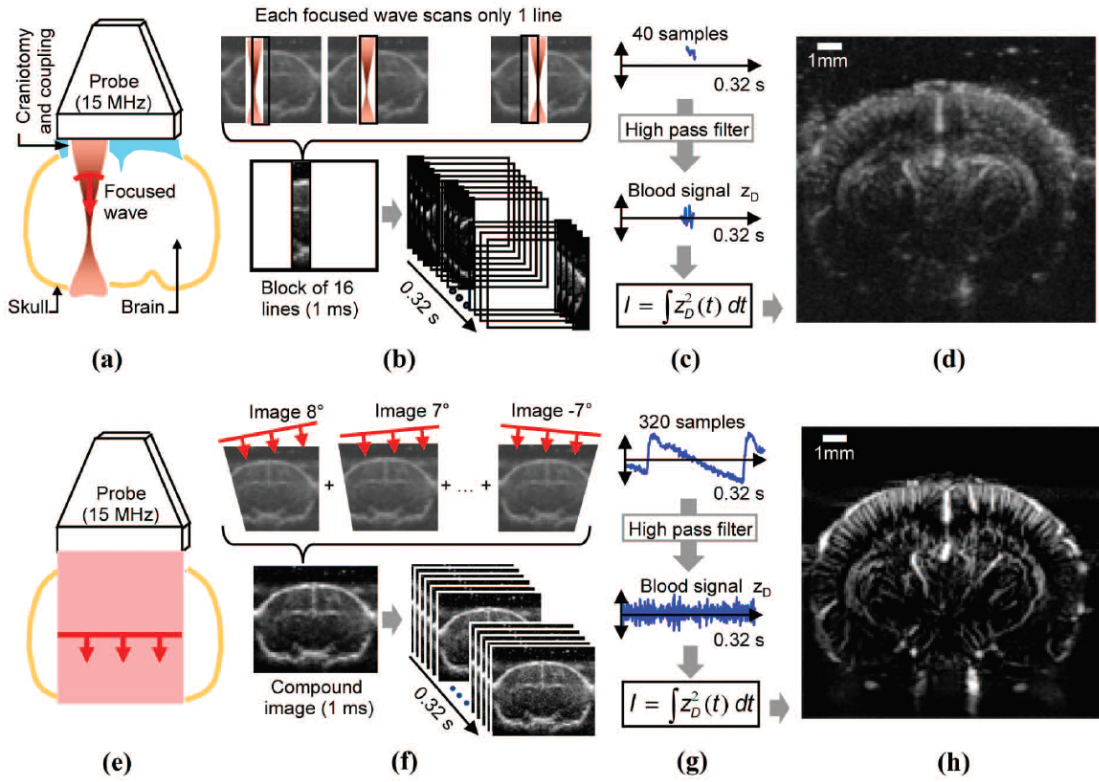


Figure 2.2: A schematic description of the processing procedure during conventional Doppler (top row) and μ Doppler (bottom row) modes [1]. (a) Experimental setup: The probe is placed on top of the cranial window. (b) Acquisition sequence: The image is captured block by block using focused waves. (c) Signal processing: A high-pass filter is applied to reject tissue-motion and then the mean intensity is calculated from the blood signal. (d) Example of a conventionally acquired PDI. (e) Same experimental setup. (f) Acquisition sequence: Plane-waves of different angles construct a compounded image. A PDI is then resulted after 320 compounded images. (g) Same signal processing. (h) Example of a μ Doppler (high frame-rate PDI) image.

that procedure is compared to that of conventional ultrasound.

More specifically, for fUS acquisition, a number of tilted plane-waves is emitted, and the raw backscattered echoes are firstly beamformed (each using a parallel beamforming procedure) to a set of images that is then coherently summed in a composite image called a compound ultrasonic image. Each compound image constitutes an image frame of the final dataset, containing a sample of the signal for each pixel. These images have better contrast, resolution and reduced noise levels opposite to conventional ultrasound - although using much more emitted waves - or to single plane-waves, that are quite unfocused.

Then, the compounded, beamformed frames are filtered in parallel in order

to distinguish between blood and slow-moving tissue signals. Because of cardiac pulsatility and respiration, tissue motion cannot be ignored. As indicated by their different spectral characteristics, an initial idea, proposed in the first fUS paper by [2], was to use a high-pass filter in order to cut off the tissue low frequencies. However, that frequency threshold is not always easily defined. A more promising solution was given later on by [4] regarding the use of a Singular Value Decomposition (SVD) method. This method could benefit from the temporal and spatial differences between the motion of blood, tissue as well as noise.

As a result, regarding the information contained in a PDI, the value of a pixel is calculated as the mean intensity of the Doppler signal in that pixel at a given time:

$$I(x, z) = \frac{1}{N} \sum_{i=1}^N s_F^2(x, z, t_i) \quad (2.1)$$

where I is Power Doppler intensity; x, z , coordinates of the pixel in the imaging plane; N is the number of samples acquired; s_F is the amplitude of the compound B-mode image after filtering; t_i time, where $t_i = i/f_{samp}, i = 1..N$ and f_{samp} the frame rate.

2.2 ICA Analysis Method

At this point of the report, after having explained the imaging modality used, the main method used for data analysis, the Independent Component Analysis (ICA) will be described. I cover ICA-related topics including the definition as well as underlying principles and assumptions, important for the rest of the thesis.

2.2.1 Introduction

ICA is a data-driven and blind-source-separation method which does not require any prior information or a previously defined model. This means that, by attempting to find common feature patterns within data, it can reveal networks that cannot be easily modeled without any assumed anatomically-based information. So, task-relevant as well as task-unrelated networks are discovered and may lead to connections that could not have been assumed based on theoretical principles.

2.2.2 Methodology

The basic theoretical concept underlying ICA is the unmixing of a multivariate signal into multiple independent sub-components, using a linear model [12], [13]. In other words, its goal is to decompose the vectorized two-dimensional matrix of the stack of measured image data (ICA input vector's dimensions are time by pixels) into two other matrices, the time courses and the associated spatial maps of the

underlying “hidden” signal sources (components), whose combination can produce the actual measured signal. Without the independence constraint, the equation 2.2 (which is also called as a matrix factorization in the literature) has infinite number of solutions. So, ICA models the data as a fixed number of spatially or temporally independent components (ICA dimensionality), which then are linearly mixed [13]. The produced model will not include any noise term, since the noise is assumed here to have an unknown distribution and it can only be treated as a nuisance.

The ICA linear model is described by:

$$Y = A \cdot X \quad (2.2)$$

where Y is the 2D space-time matrix of the collected fUS data, A is a mixing matrix and X is the matrix of the sources or independent components. If we denote with $W = A^{-1}$ the weighting matrix, then it is called the unmixing or separating matrix. So, by observing only the X data, both A and X have to be estimated. To achieve that, some important assumptions need to be made. The main assumptions are that the estimated sources are statistically mutually independent and are non-Gaussian.

Regarding to the sources’ independence, spatial or temporal independence can be also assumed. In the first case, spatial ICA (sICA) takes into account the sparse distributed nature of the spatial patterns, whereas in the second case, temporal ICA (tICA) the temporal evolution of a small number of pixels in a region of interest. In most works, sICA is the preferable way to apply ICA as spatially distributed and temporally coherent brain networks are often the research goal of fMRI studies. Then, equation 2.2, more specifically, is formed as

$$Y_{t,j} = \sum_{k=1}^K A_{t,k} \cdot X_{k,j} \quad (2.3)$$

where Y is the matrix of the collected data, of dimension equal to the number of time points ($t = 1, \dots, T$) by the number of pixels ($j = 1, \dots, J$), A is a mixing matrix of dimension equal to the number of time points by the number of independent components - ICs ($k = 1, \dots, K$), and X is the matrix of the sources of dimension equal to the number of ICs by the number of pixels. Then, the extracted spatial maps and their time-series are described by matrices X and A , respectively, shown also in figure 2.3. In tICA, the content of the two matrices is reversed.

In [15], a way to exploit both spatial and temporal independence was proposed, where tICA was applied to regions of interest that were first determined by sICA, yielding a set of temporally independent modes.

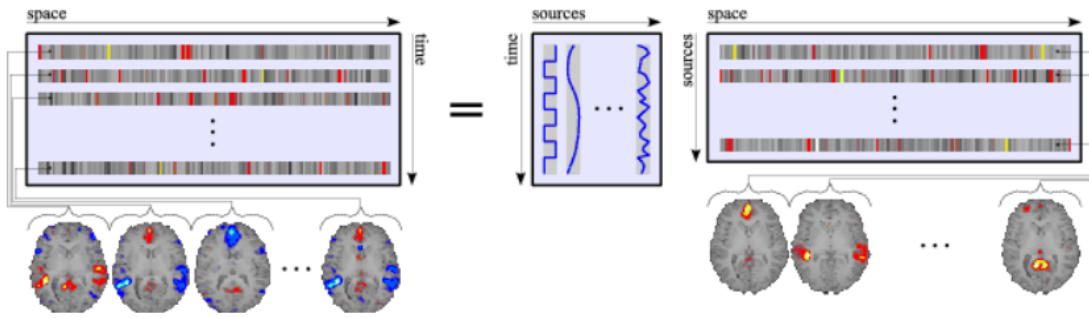


Figure 2.3: sICA model [14]

2.2.3 ICA Assumptions - Ambiguities

A number of challenges have to be addressed when an ICA approach is applied for standard fMRI data analysis. That is achieved by choosing some parameters as initial assumptions. Some of the most common assumptions that seem logical also in the context of fUS are as follows:

- The fundamental assumption in ICA is that the independent components must be non-Gaussian distributed. Typically, the signals of interest in fMRI are focal and thus have a sub-Gaussian spatial distribution (with the probability distribution having a strong tail decay property). However, the artifactual signals will be more varied and potentially super-Gaussian (with probability density functions - PDFs - heavier-tailed and peakier than the Gaussian). These interesting distribution types, sub-Gaussian and super-Gaussian sources can be extracted from ICA. The Gaussian signals cannot be separated so Gaussian physiological noise can be included in the extracted components and it can contaminate them.
- ICA is a stochastic algorithm which means that its output components may not be the same during every run and may appear in a different order, independently of the task-relevance. This is happening since the unmixing matrix W is iteratively updated until the optimization measure, like maximum non-gaussianity, is achieved. With the iterative procedure being a stochastic gradient-based optimization, W is usually initialized with random numbers at the beginning of the iteration, introducing randomness into the decomposition. Thus, ICA does not provide any information about the ordering or the variances of its components, which makes it impossible to distinguish strong and weak components. Some solutions are given in [13], including the computing of components' variance, or cross-correlation of each component's time-course with the behavioral experiment pattern for ordering the correlation coefficients.

As far as the ICA algorithm is concerned, there are various ways for the signals to be separated and the ICA model to be estimated. The main approaches used are maximum non-gaussianity, minimum mutual information and maximum likelihood. The typical way for measuring non-gaussianity is by using the value of kurtosis (or the fourth-order cumulant) or optimally by negentropy (negative entropy or differential entropy), that is based on the entropy-concept of information theory. Negentropy can be implemented with great difficulty, but it can be approximated by higher-order statistics which for instance is used in the well-known Fast-ICA [16] and Jade [17] algorithm. Moreover, the way of maximizing likelihood relates to the concept of infomax principle, used by the Infomax algorithm [18].

- The number of components (model order) is a free parameter defined empirically or estimated. According to [19], a way to estimate the order is by using information-theoretic approaches, such as Akaike’s information criterion (AIC) [20], minimum description length (MDL) criterion [21] and the Bayesian information criterion (BIC) [22]. In the same work, the software package ICASSO was also suggested to analyze the independent component (IC) estimates at different orders. ICASSO [23] is a clustering software providing an explorative visualization method for investigating the relations between estimates after running ICA multiple times¹. The authors showed that the overestimation of the number of selected components can decrease the stability of the IC estimates as the task-related components may not be compact but unnecessarily split in more than one.
- Before applying an ICA algorithm, it is commonly necessary to do some preprocessing on the input data. The main two preprocessing methods that make the ICA application better conditioned are data centering and whitening. These two methods make input data zero-mean as well as uncorrelated and with unit variances, respectively. One popular method for whitening is PCA. The aforementioned methods along with several others are further described in Section 4.4.4.

2.2.4 ICA Approaches

Two strategies are commonly used in studies where multiple subjects are involved [24]. In the first strategy, ICA is applied separately on each subject’s signals (single-ICA) [25]. The second strategy is called Group-ICA. Group-ICA is applied on the whole set of group data.

¹The way ICASSO can be used for selecting the number of components is described in more detail in Section 4.4.4

2.2.4.1 Group-ICA Approach

Apart from the variability arisen from the different discussed parameters² of the ICA algorithm, there is also inter-subject variability in the results derived from single-ICA runs. So, a Group ICA approach is reasonable to be applied in order to find reproducible components after combining data from different subjects. Group analysis of fMRI is another important strategy for studying specific conditions within or between groups of subjects and draw inferences between them.

However, the application of ICA to different subjects in a group is not so straightforward. After single-ICA, each subject's sources will be sorted in a different way, having different mixing matrices. In 2001, the first approach for applying ICA to multi-subject data was published by [25], followed later by a series of other approaches by [26], [27], [28], [29].

The stages for implementing Group ICA include data-reduction, forward-estimation and back-reconstruction, then followed by a statistical analysis of output results.

Data-reduction stage: It is typically performed using a two-stage PCA. One PCA at single-subject level and a second one at group level. After having the results of the first PCA, that can be performed in a common space or individually to each subject, the data is concatenated temporally or spatially.

Forward-estimation stage: There are at least five approaches, gathered in the following schematic figure 2.4. The existing approaches mainly differ in the way the multi-subject data is organized before being input to the ICA and in some assumptions regarding how group estimates are computed and what output is eventually extracted (for example, single-subject contributions, group averages, etc).

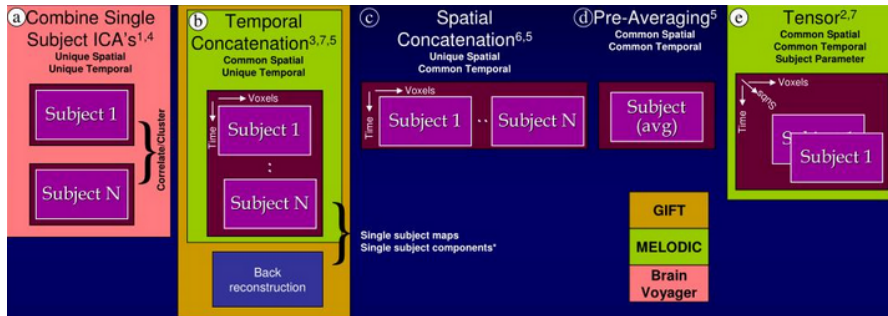


Figure 2.4: Five Group ICA Approaches: a) single-ICA on each subject, followed by correlation or clustering, b) temporal concatenation followed by an aggregate ICA analysis and a back-reconstruction step to compute subject-specific maps and timecourses, c) spatial concatenation or d) pre-averaging prior to ICA, and e) tensor-based approaches stack the data into a cube

²The ICA parameters will be further discussed in Section 4.4.3

The first method shown performs single-ICA to every subject and then attempt to combine these into group results post hoc, for example using spatial correlation or clustering between components.

All the other methods, mentioned above and shown in figure 2.4, include an ICA computed directly on group data. The temporal concatenation approach allows for unique time-courses for each subject but assumes common group maps, whereas the spatial concatenation approach allows for unique maps but assumes common time-courses. The fourth method, that includes pre-averaging all subjects' data and performing ICA on the mean dataset, constitutes the least computational method. However, it makes a strong assumption that all subjects have both common time courses (TCs) and spatial maps (SMs). The fifth approach attempts to make no assumptions between subjects. It is based on a three-dimensional tensor to estimate a single spatial, temporal, and subject-specific "mode" for each component.

Back-reconstruction stage: The subject-specific TCs and SMs are estimated by back-projection using inverse PCA projection [24] or regression-based methods [30].

In this chapter, the literature behind fUS imaging and data-analysis methods is going to be explored. In Section 3.1, an overview of the fUS-related works is presented, revealing a big gap in more advanced analysis methods in Section 3.2. That led to the need for further exploration on data-analysis methods. The methods that have already been reported in fMRI studies are reviewed in Section 3.3, leading also to the motivation regarding the choice of ICA.

3.1 Applications of fUS in Neuroscience

The development of robust fUS imaging can have a wide range of possible applications. It has already been studied for small animal models, like rodents (mice and rats), small mammals as well as in human clinical experiments. More recently, the first experiments on non-human primates were demonstrated in [31]. In this section, we will briefly summarize the work done on functional brain imaging with fUS. Most of the following described scientific publications are well reviewed also in [5]. Additionally, in the current survey, we have compiled a cumulative table of papers on fUS (Table 3.1) regarding details about every experiment and fUS set-up parameters.

3.1.1 Research Use

In [2], the first in vivo proof of this concept was shown by imaging micro-vascular changes in the trepanned brain of anesthetized rat adults during whisker stimulation or induced epileptic seizures. During whisker-stimulation experiments, the related regions were discovered after constructing activation maps by correlating the stimulus pattern used and the time-series of each pixel. In the same study, another very important asset of fUS was exploited which is its compatibility with other techniques commonly used, like electrophysiological recordings. For instance, fUS was easily combined with EEG recordings to study the epilepsy disorder. Activation maps were constructed in case of artificially epileptic rats. In that case, different activation patterns were apparent, all related to the theoretically connected cortex and thalamus regions.

In [32], the fUS method was extended to portable systems and applied to awake and mobile rats, using a small ultrasonic probe fixed on the rat head, a method called mobile fUS (or mfUS). The testing on awake mice is important as the use of anesthesia excludes behavioral and cognitive experiments and raises questions

Publication	Animal	2D/3D/4D	Experiment	Skull Preparation	US Device	US Frequency	Spatial Resolution
Macé et al. (2011)	Rat	2D	Whisker Stimulation & Epilepsy	Craniotomy	Aixplorer; Supersonic Imagine ¹	14.4MHz	100µm
Demené et al. (2014)	Human	2D	Without Stimulation	Intact Skull	Aixplorer; Supersonic Imagine	6MHz	250µm
Urban et al. (2014)	Rat	2D	Electrical Stimulation of the Forepaw	Thinned-skull Window	V1; Verasonics, USA	15MHz	100µm
Osmański et al. (2014)	Rat	2D	Electrical Stimulation of Sciatic Nerve & Without Stimuli	Thinned-skull Window	Aixplorer; Supersonic Imagine	15MHz	100µm
Osmański et al. (2014)	Rat	2D	Olfactory Stimulation	Craniotomy	Aixplorer; Supersonic Imagine	20MHz	100µm
Sien et al. (2015)	Rat	3D	Epilepsy & Behavior Tasks	Craniotomy & PMP ²	Aixplorer; Supersonic Imagine	15MHz	100µm
Demené et al. (2016)	Rat	3D-4D	Without Stimulation	Craniotomy	Aixplorer; Supersonic Imagine	15MHz	100µm
Enrico et al. (2016)	Rat	2D	Sciatic-Nerve Stimulation	Thinned-skull Window/Intact & Contrast Agents	Aixplorer; Supersonic Imagine	20.3MHz	100µm
Gsenik et al. (2017)	Rat	3D	Visual Stimulation	Craniotomy	Aixplorer; Supersonic Imagine	15MHz	110µm
Imbault et al. (2017)	Human	2D	Cortical Stimulation	Craniotomy & Durotomy	Aixplorer; Supersonic Imagine	6MHz	250µm
Tian et al. (2017)	Mouse & Rat	3D	Without Stimulation	Intact Skull	Aixplorer; Supersonic Imagine	15MHz	100µm
Demeue et al. (2017)	Human	2D	Epilepsy	Intact Skull	Aixplorer; Supersonic Imagine	6MHz	200µm
Macé et al. (2018)	Mouse	3D	Visual Stimulation	Craniotomy	Vantage 128; Verasonics, USA	15MHz	100µm
Bimbard et al. (2018)	Ferret	3D	Frontal & Auditory Cortex Stimulation	Craniotomy	Aixplorer; Supersonic Imagine	15MHz	100/300µm
Demené et al. (2018)	Rabbit	2D	Without Stimulation	Craniotomy	-	6.4MHz	~250µm
Rau et al. (2018)	Pigeon	3D	Visual & Acoustic Stimulation	Thinned-skull Window	Vantage 128; Verasonics, USA	16MHz	100µm
Dizeux et al. (2019)	Monkey	2D	Complex Cognitive Tasks	Craniotomy	-	15MHz	100µm

Table 3.1: Published papers on fUS and categorization depending on the animal species used, the set-up parameters of the conducted experiment and details about the ultrasound (US) device and probe used.

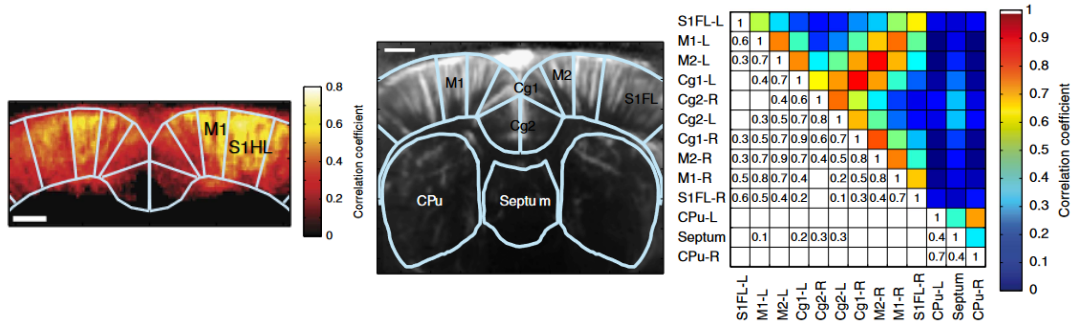


Figure 3.1: Example results from [35]. Left: Averaged spatial map of cortical regions correlated to the right S1HL+M1 seed region. Middle: Anatomical regions used for FC analysis. Right: Correlation matrix showing FC

about modification of neuronal metabolism and cerebral blood flow, according to [46]. Then, mfUS was further combined with electroencephalographic activity (EEG) for investigating the detected hemodynamic brain states on both spatial-navigation tasks and absence seizures, in case of epileptic rats, over repeated and prolonged periods of time, for acquiring 3D images. At the same year, another study, [4], achieved to generate 3D fUS imaging as well as to propose a novel tomographic strategy for 4D (3D images in time) imaging. It is worth noting that the study contains a compact summary table regarding the in vivo microvascular imaging technique. Moreover, in [38], 3D functional images of the whole rat brain activity were successfully obtained during a visual-task stimulus, and the influence of the activated regions was examined with changes made in some of the stimulus parameters.

As far as the fUS post-processing analysis is concerned, in [35], apart from the detection of the functionally correlated contralateral cortical areas when activated by electrical stimulation of the right and left sciatic nerve, a new insight about fUS was tested. That was the identification of intrinsic functional-connectivity (FC) patterns derived from the above experiment using a seed-based and an SVD data-driven approach on each pixel's time-series, without using information regarding the stimulation pattern as before. In other words, functionally and/or anatomically connected regions were investigated for showing similar changes in the spontaneous fUS signals. An example of the results collected in that study is shown in figure 3.1. The results were similar to those obtained after resting-state fMRI (rs-fMRI). Additionally, the paper concludes that fUS is a promising method to be performed complementary to fMRI in clinical applications. During the same year, the same scientific team investigated the odor-activated zones in response to two different odorants. The spatial-activation maps were created after correlating the fUS signals with the stimulation pattern.

Despite the aforementioned resolution drawbacks of non-invasive fUS, non-

invasive methods were further investigated by [37] with the use of a contrast agent in rats, such as inert gas microbubbles for enhancing the fUS signals, and also without by [40] in mice and young rats. In the latter study, imaging of the entire brain under anesthesia through the intact skull and skin, and without any contrast agents was performed, possibly giving the opportunity for future longitudinal³ studies of brain vascularization. Moreover, fUS has been tested on a thinned-skull window [35] as an alternative choice for both the fully non-invasive and also the craniotomy methods. The advantage of the less invasive thinning procedure is significant compared to a complete craniotomy as it facilitates the conductance of longitudinal studies as well, yet the low image quality becomes a problem over time [34]. Thus, the superior performance of a craniotomy commonly dominates.

Apart from the physiological stimuli mostly used, electrical stimuli were also employed in the work of [34]. The spatio-temporal evolution of the CBV hemodynamic response function (HRF, that is, the obtained fUS signal response) was investigated in response to sensory-evoked electrical stimulus in the thinned-skull rat forepaw for different time durations. It was noted that even for short stimuli, for example for a single pulse, significant hemodynamic changes can be observed.

Furthermore, as already mentioned, fUS studies have been successfully applied on different species rather than only on rodents and humans. Small mammals, such as rabbits [44], have been used while they underwent cardiac arrest and a cardiopulmonary resuscitation. Also, pigeons [45] were tested during auditory and visual experiments as well as ferrets during auditory stimulation. The most recent study (2019) was on monkeys [31] whose hemodynamic responses were visualized during cognitive tasks. In that study, the analysis method of Multi-Voxel Pattern Analysis (MVPA) was used to decode the stimulus frequency from the hemodynamic signal.

3.1.2 Clinical Use

Beyond research purposes, fUS is also a promising method applied in clinical practice. In [39], fUS was used to image task-evoked brain activation during tumor surgery after opening the skull and the dura mater of the patients, while in [33], fUS was used to scan brains of awake newborns. The first work concluded that, after stimulation induced by motor and sensory tasks, a steady signal increase in the associated cortical area was observed in a range of 20% compared to baseline. Also, fUS was successfully applied on both awake and anaesthetized patients. On the other hand, in the latter study, an extensive spectral analysis of the signal in each pixel was performed via a fast Fourier transform, for computing blood parameters, such as the maximum speed and the time to systolic peak. Recently, another work conducted by [41] was about brain activity in human newborns. In

³involving continuous or repeated measures

that study, fUS was accompanied by EEG in order to discriminate sleep states, and also during interictal periods to determine the ictal foci of the newborns' seizures.

3.2 Literature Shortcomings in fUS-data Analysis

fUS research has essentially started in 2011 through the seminal work of [2]. To date, there is a limited number of papers published, but they are rapidly increasing as more and more research teams around the world are involved with fUS imaging and search its potential uses. Most works first focus on investigating fUS performance and optimizing parameters for different experimental conditions. For instance, fUS works described in [40], [36], [38], [34], [47], mainly examined the sensitivity in capturing coarse-grained sensory hemodynamic responses. Then, only a few studies have proceeded to a first-level analysis, exploring brain connectivity using mainly correlation or statistical methods, with [35] being the first one, and later on followed by others, like [47], [38], [31]. Then, beyond the time domain, a spectral analysis in the frequency domain was done in [33]. Thus, the previous review-section 3.1 on fUS work revealed a big gap in more advanced analysis methods.

3.3 fMRI-data Analysis Methods

To fill this gap and exploit other aspects of the data, I also reviewed what it is mostly reported in studies regarding the similar-principle technique of fMRI. Detailed review studies on fMRI analysis methods have been conducted by [48], [49], [50], [51]. Table 3.2 summarizes some of the main methods used for fMRI analysis. On its horizontal axis, the various computational methods used for fMRI-signal analysis are shown, while on its vertical axis appears a grouping of their characteristics. Here, we are interested in methods applied to both task-based and resting-state experiments, so the type of experiment will not play a significant role. The remaining characteristics that are presented on the table will be mainly examined.

In practice, in fMRI studies the first idea is to process the data with simple univariate analysis methods. With widely-applied methods, such as t-tests, correlation analysis (seed- or stimulus-based) and the General Linear Model (GLM), each brain voxel is examined independently, and its intensity differences are measured and interpreted irrespectively of all the other voxels. The first two methods have been widely used in fUS studies, but it is commonly claimed that the derived results have not yielded robust and definitive conclusions, because these strongly depend on the a priori selected region of interest (ROI) used as a reference for the other pixels. This is valid especially in neuroscientific studies, given that the brain is a system with complex organization and tight interconnections between different cortical regions. The third-mentioned method, GLM, has not been applied

Characteristics/Methods	T-test	GLM	PPI	SEM	DCM	GCM	MVPA	Correlation-based	PCA	ICA	FCMA	Graph Theory
Resting-state fMRI		x		x	x	x	x	x	x	x	x	x
Task-based fMRI	x	x	x	x	x	x	x	x	x	x	x	x
Functional Connectivity	x	x						x	x	x	x	x
Effective Connectivity			x	x	x	x						x
No a priori data					x	x	x		x	x	x	x
A priori data available	x	x	x	x				x				
Model-based	x	x	x	x	x	x		x			x	
Data-driven							x		x	x		x

Table 3.2: This table summarizes some of the main methods used for fMRI methods: T-test, General Linear Model (GLM), Psychophysiological interactions (PPI), Structural Equation Modeling (SEM), Dynamic Causal Modelling (DCM), Granger Causality Mapping (GCM), Correlation-based methods, Multi-voxel Pattern Analysis (MVPA), Principal Component Analysis (PCA), Independent Component Analysis (ICA), Full correlation matrix analysis (FCMA), Graph Theory

yet, because the determination of the model’s parameters, such as experimental paradigm (stimulus pattern) and motion (noise) patterns, is necessary. Since it is a model-based method, we can only study the activation that we have modeled for and, besides, the existing brain models are not so well-parametrized. As also proven for fMRI, traditional GLM-based analysis is not so sensitive in detecting task-related changes in fMRI signals compared to data-driven methods, such as spatial Independent component analysis (sICA), which performs much better [52].

A comparison between GLM and sICA for fMRI data is shown in figure 3.2, depicting clearly the GLM-requirement for a reference temporal-model (design matrix) in contrast to sICA. Additionally, the fact that in most studies, an experimental task condition modulates the activity pattern among multiple distinct voxels makes the application of multivariate and data-driven methods a more appropriate way of analysis. Thus, it would be more beneficial to statistically examine simultaneously different groups of voxels instead of intensity values on a per-voxel basis. These are the main reasons that we need more advanced analysis methods in the case of fUS, moving to multivariate and data-driven methods.

Furthermore, considering that the brain is organized into a number of different functional networks, an optimal analysis technique would be able to distinguish these networks and extract the common signals of each one directly from the data. The ICA method has been already utilized for various fMRI applications resulting to a significant degree of understanding the hidden spatiotemporal network structures in the brain. Thus, ICA seems as a good candidate to be tested on fUS data as well. As already described, FC constitutes the analysis of correlations between measured function of distinct regions of the brain. By evaluating the calculated correlations, some forms of associations between different voxels or regions can be uncovered as well as activated and deactivated brain areas can be identified.

Thus, a method that would lead to FC conclusions was considered a strong initial argument for the proposed fUS data-analysis. In the current work, I am

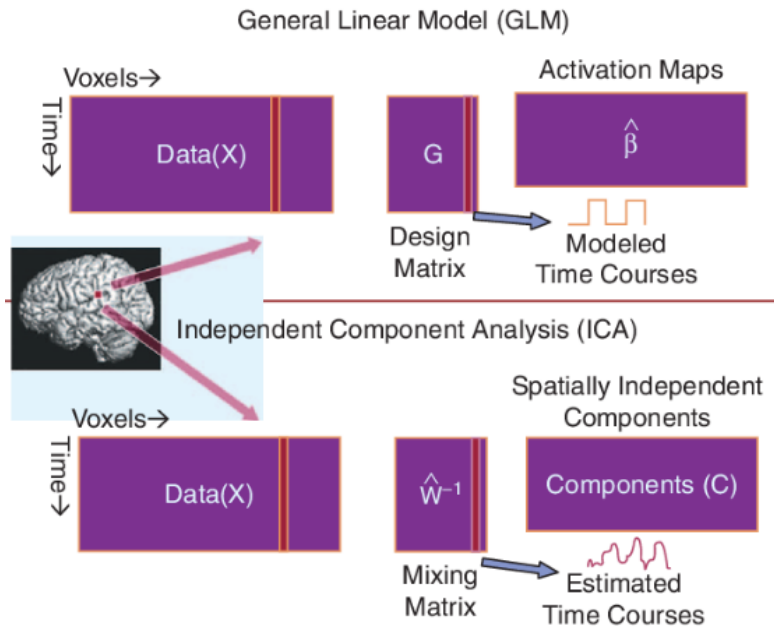


Figure 3.2: A comparison between GLM and sICA showing their different data-modelling. [12]

not considering approaches for effective (dynamic) connectivity leading to directional and causal relationships among brain regions, such as dynamic causal modeling (DCM), Granger causality mapping (GCM), structural equation modeling (SEM), psychophysiological interaction (PPI), graphical causal modelling (GCM), dynamic Bayesian networks, and switching linear dynamic systems [49], [53].

Compared to other methods used for FC inferences (shown in Table 3.2), ICA is regarded as preferable to PCA in fMRI cases, where the intention is to estimate only a number of linearly uncorrelated components and not the independent ones. Both properties are valid when the multivariate normality assumption is met, that is not the case with fMRI and fUS data. The spatial independence enforced upon components is a more appropriate assumption for blind-source separation of the data compared to PCA: Spatial ICA demands only that components' time-courses not be highly co-linear, resulting in a more biologically plausible systems model than that derived from a PCA decomposition where the analysis enforces orthogonality between time courses, precluding the detection of signals which are partially associated in the temporal domain. The above statement is also supported by [54] for fMRI cases, so the same is expected for the same-principle fUS cases.

Regarding Multi-Voxel Pattern Analysis (MVPA) and Full correlation matrix analysis (FCMA), although these methods seem quite promising for fMRI, and subsequently for fUS, they are very computationally demanding and data- and memory-intensive, as they need large datasets [55].

Moreover, approaches based on graph theory are very computationally complex, compared to ICA, making the application on the whole brain currently intractable [56]. Thus, the computational complexity, along with the size of data which is quite high, preventing these from being the first choice for multivariate analysis.

Alterations of neural activity may be affected by asking the subject to perform a task designed to target a specific cognitive process or can also be evoked spontaneously while the subject is resting in the absence of conscious mentation, that is called resting state. These two types of functional experiments, task-based and resting state, were conducted on mice and further analyzed using the ICA method. In this Chapter the imaging and experimental-setup parameters of all the experiments are given, and the overall analysis strategy is described. Regarding the ICA algorithm, all of the free parameters, assumptions as well as any pre-processing and processing steps are explained and justified in great detail. A set of five datasets obtained from a 2D visual-stimulation experiment was used for testing reliability and reproducibility of the ICA significant results.

4.1 fUS Set-up and Imaging Parameters

For the recording of the functional ultrasound data, an ultrafast ultrasonic device, Vantage 64-LE, was used as well as a 30MHz linear array transducer in order to obtain the angled plane-wave images. The transducer of the system was placed on top of the brain, after part of the skull was removed, cleansed, and covered with a plastic acoustic window (that fits the cranial window) as well as a gel to couple the ultrasound to the skull. In this work, all the experiments were conducted on awake mice.

For the experiments, we used 14 angled (-5 to 5 degrees) plane waves with a Pulse Repetition Frequency (PRF) of 8 kHz . After every transmitted wave, the raw backscattered echoes are firstly beamformed to a set of images that is then, coherently summed to maintain high temporal resolution, forming a compound image. Afterwards, the temporal resolution is $PRF/N_a = 8000/14 = 571.43\text{Hz}$. Finally, a total of 120 compound images were used to compute one Power Doppler image (PDI), resulting in a final temporal resolution of 4.7619Hz .

4.2 Functional Experiments

4.2.1 Task-based Experiments

In fMRI studies, task-based or stimulus-driven experiments have been widely explored in order to offer a deeper understanding of the brain functioning. Using

the relative changes from baseline in the collected signal during a given task, or in response to a stimulus, can straightforwardly lead to inferences regarding several activated and deactivated brain areas.

A typical task-based experiment employs sensory stimuli, such as visual or auditory stimulus, for a fixed duration of time, in which case a large number of PDIs can be acquired.

4.2.1.1 Visual-stimulation Paradigm

Here, the well-studied visual stimulation was applied, where the vision-related regions are going to be further investigated. Several visual-stimulation experiments took place, by showing images in one or both screens which were located in front of the mouse. Consequently, one or both mouse’s eyes and visual fields were stimulated, respectively.

Moreover, the visual experiments were recorded both on a single coronal slice (2D-dataset) and on multiple coronal slices (3D-dataset). In the 2D fUS acquisition set-up, one mouse was used and a total of 5 datasets per experiment were recorded, each one consisted of 1143 time-frames representing a duration of 240s. Regarding the stimulation pattern, the subject (mouse) performed a task in a block design paradigm, which means that the stimulation pattern included blocks of both rest (“off”) and task (“on”) periods. The stimulation was a set of 8 grey images shown on a computer monitor for 5 seconds, followed by 10 “dead” seconds where the screen went blank, and repeated after that.

A visual example of the mean of the collected PDIs in a fUS visual-stimulation dataset is depicted in figure 4.1.

4.2.1.2 Visual-information Chain Pathway

The visual-stimulation experiments are commonly used in literature, as they can be easily carried out by providing a physical visual input. A stimulus, such as displaying an image, can be applied in one visual field or simultaneously in both visual fields to test the way neural activation in different brain regions is influenced.

Moreover, during such a visual task, neural activation can be evaluated by taking into account the well-studied visual pathway and the known brain regions which are chiefly involved [57]. A schematic illustration of the processing pathway of visual information is given in figure 4.2. This complex pathway begins with the collection of photons on the retina. Visual information travels along the optic nerves, is pre-processed in sub-cortical relays, such as the left and right Lateral Geniculate Nuclei (LGN) or the Superior Colliculus (SC), and is finally processed in the Visual Cortex. The so-processed information is then sent to other cerebral areas that will for instance trigger an action or a memorization. These regions were well-reported in case of fMRI, for example in [58] and [59].

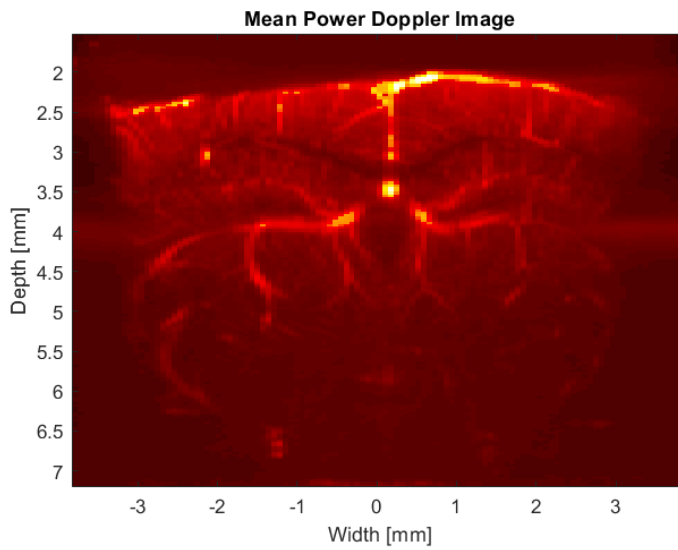


Figure 4.1: Mean of PDI frames in the visual-stimulation experiment. The vasculature structure of a mouse brain is shown.

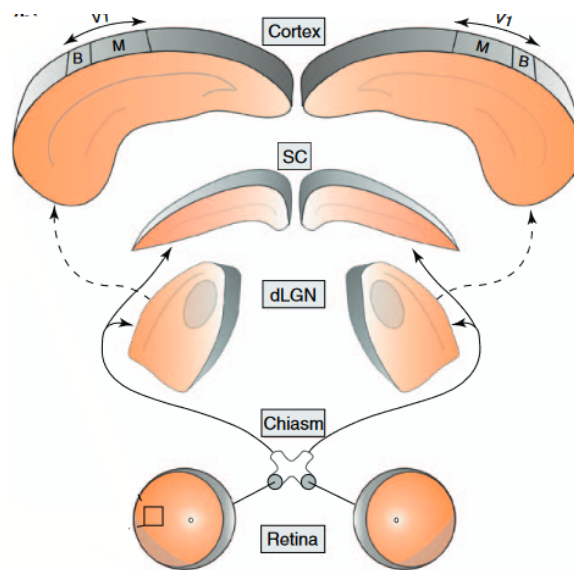


Figure 4.2: Mouse visual pathway, showing direct (solid arrows) and indirect (dashed arrows) retinal projections [57]

Especially in the case of fUS, visual-stimulation studies are generally preferred for another reason as well. Through the open skull, the (task-related) visual cortex is easily accessible for acquiring functional images.

4.2.2 Resting-state Experiments

Resting-state experiments also took place, providing new insights on the functional architecture of healthy brains. That type of studies investigates synchronous activations – between regions that are spatially distributed across the brain– occurring in the absence of a task or stimulus. Therefore, resting-state experiments are widely tested as they require the least effort of the subjects involved.

With these experiments we focus on the discovery of functional networks across the whole brain, as opposed to distinct functional areas that are activated, for example, by a specific visual stimulus paradigm. On the other hand, this means that the ground-truth of the stimulation pattern is missing, leading to a difficulty in evaluating the obtained functional networks.

In recent years, the resting-state fMRI (rs-fMRI) experiments have gained in popularity and are used to identify resting-state networks (RSNs), so fUS resting-state experiments is useful to be also examined. In addition, the characterization of consistent and robust resting state networks are still quite unexplored, especially in rodent models. Some examples of a fMRI work revealing the functionally connected mouse brain regions mappings was given in [60], [61], [62].

Here, a 3D dataset was collected comprising images from 18 coronal slices, insted of only one. The whole experiments lasted for 6,300*seconds*, obtaining approximately 2000 images (PDIs) in each slice position.

A summary of all the experiments conducted and used for the thesis’ data analysis is given in Table 4.1.

Experiment	2D/3D	Number of mice	Number of trials/datasets
Visual-stimulation (both-side screen)	2D	1	5
Visual-stimulation (single-side screen)	2D	1	5
Resting-state	3D	1	1

Table 4.1: Summary of experiments and datasets employed in the current thesis.

4.3 Overall Analysis Strategy

4.3.1 Input Data

A set of five datasets obtained from a 2D visual-stimulation experiment is used for determining and testing the selected parameters. Each dataset contains a set of 1143 frames or PDIs capturing the vascularization of one specific (2D) coronal slice. An illustration of the information contained in a PDI is shown in figure 4.1.

4.3.2 Data Pre-processing

As done with fMRI signals, fUS signals have to be preprocessed before being analyzed. So, prior to ICA, the raw data should be subjected to preprocessing methods, such as those included in a standard SPM (Statistical Parametric Mapping) pipeline¹, since the main principles of fUS and fMRI are similar. The choices of the preprocessing parameters and steps is investigated to discover the most appropriate preprocessing pipelines.

In every neuroscientific study, the types of pre-processing methods, as described in [63], as well as the order that they will be used should be chosen appropriately as they can be influenced by several aspects, such as the type of stimulus, the experimental hypothesis, and the acquisition environment.

The preprocessing pipeline finally adopted and the configuration of the optimal parameters are described in more detail in Section 4.4.4.

4.3.3 ICA Analysis

Both single- and group-ICA strategies are commonly used in studies where multiple datasets are available. In the first strategy, ICA is applied separately on each subject's signals, and afterwards the relationship between subjects' - or within a single subject's recordings - independent components is examined by the means of subjective identification [25]. In the second strategy, Group-ICA is applied directly on the group data, and then common ICs as well as individual subject's specific ICs can be further obtained and examined. Although Group-ICA seems to be superior than single-ICA, both strategies is important to be tested in the case of fUS images as well as when not a lot of datasets are available and then group-ICA is not feasible.

4.3.4 PDI-Atlas Registration

In the proposed strategy, the next step after having extracted the ICA spatial maps is to anatomically evaluate them in order to better interpret the ICA performance and the produced spatial brain areas between multiple subjects. The evaluation can be performed by a technique registering a fUS image to a brain-atlas image, leading to a geometrical alignment of the two different images. There are many examples of brain atlases, including 3D tomographic images, anatomic specimens as well as several histologic preparations regarding regional cytoarchitecture information [64]. In this work, registration is performed to align a functional PDI to a reference anatomical brain atlas image.

An anatomical atlas is usually encoded as a pair of two image volumes, an intensity or anatomical image and a label-annotated image. Both images have the same axis dimensions, so the label of a region in the first type of image can

¹<https://www.fil.ion.ucl.ac.uk/spm/>

be easily identified, a concept called label propagation. Assuming that the fUS images (thus the ICA spatial maps) are aligned with the atlas images, we can use label propagation to identify the anatomical regions that appear activated in the ICA spatial maps. However, most of the times, the new target images do not directly spatially correspond to the atlas images. This problem can be solved by image registration. The atlas image is then used as a reference image and the other, target, image is geometrically transformed in different ways, e.g. rotated, in order for these two images to be aligned. The detailed methodology of image registration is given later, in Section 4.4.6.

4.4 ICA Implementation

4.4.1 Preprocessing Steps

In this section, the proposed preprocessing pipeline is thoroughly presented.

4.4.1.1 Image-boundary Removal

One of the first tasks that should be applied to the fUS images is removing a number of pixels that are located at the edges of the images as these correspond to regions outside the brain. The exact number is dependent on the current imaging. This step not only removes useless information but also allows for faster computations in the analysis part, since image frame size is reduced.

For our experiments, to isolate the brain region, we typically discarded approximately the first and the last 50 pixels in the z-axis and 10 pixels in the x-axis.

4.4.1.2 Time-point Removal

The first few frames of the functional images are often discarded for signal equilibrium and for allowing the adaptation of each subject to the scanning noise. Similarly, some frames at the end of the imaging acquisition will also be removed, as these frames may contain some noise when the acquisition stops.

In that way, a specific number of time points for each subject will be removed for the next steps of the analysis. In the current preprocessing pipeline, four frames in total will be removed, two from the beginning and two from the end of each recording.

In addition, this step is repeated after the spatial Gaussian-smoothing step where the number of removed frames is dependent on the size of Gaussian kernel used.

4.4.1.3 Smoothing

Due to the necessity of optimizing temporal measurements, spatial resolution is usually sacrificed as part of a trade-off. A way to improve the latter is by a simple

process during which data points are averaged with their neighbours. In so doing, high-frequency signals are suppressed while low-frequency ones are enhanced.

Firstly, one of the benefits of spatial smoothing is that it can improve the SNR of the data. Because adjacent brain areas show functional similarity in their received signal data and because of signal blurring due to vascularity, fUS data is supposed to be inherently spatially correlated as collected. As a result, the most common smoothing technique is implemented by convolving the data with a Gaussian kernel (shape of a normal distribution) that matches the inherent spatial correlation of the collected fUS data. This can suppress noise sources uncorrelated among adjacent imaging voxels and increase the SNR of the data.

Secondly, spatial smoothing may also improve the validity of subsequent statistical analysis by reducing the difference between inherent spatial structure of the data and the assumed model, e.g., increasing the Gaussianity (approximation of a Gaussian distribution [65]) of the data (a key assumption of the general linear model, and random-field theory). Additionally, it is used to suppress noise and effects due to residual differences in functional anatomy during inter-subject averaging.

The optimal size of smoothing kernel is not standard, and it can be determined by the goal of the current experiment. For example, for maximizing SNR, the kernel size should match the spatial correlations of each region, while for approximating the assumed smooth Gaussian field, the ideal kernel size should be at least twice the size of a voxel. However, by using a larger kernel size, the spatial resolution of the data is reduced, the functional boundaries may be blurred, and the activation loci of a task may be shifted.

There are two choices that should be made regarding the Gaussian kernel which are the full width at half maximum (FWHM) value and the kernel size. The FWHM value is related to standard deviation s value and their relationship is $FWHM = 2.35s$. However, there is no standard way to define these parameters. After having examined the effects of different parameters' values (some of these are depicted in the Appendix A), a 3D $3 \times 3 \times 3$ kernel with $\sigma = 3$ was selected.

After the spatial smoothing, again, a number of pixels in the edges of the images and some frames in the beginning and end of the sequence are removed as the filter effect on pixels of the image boundaries is quite apparent.

4.4.1.4 Centering

Centering is a useful step applied on data, so as to make the input data a zero-mean variable. This is generally achieved by subtracting the mean of each pixel's time-course.

4.4.1.5 Whitening or Sphering

Another useful and necessary preprocessing step in ICA is to whiten the observed signals after centering. This means that before the application of the ICA algorithm (and after centering), the input vector is linearly transformed to a new vector using PCA, whose principal components are uncorrelated and their variances equal unity. Whitening has the effect of equalizing variances across all principal components, a necessary step in order to counter the fact that only a few PCA components with the largest variances are dominating the ICA components.

4.4.2 Processing Tools

For processing the fUS data, the well-known and various software packages that exist for fMRI cases were checked. In [66] a comprehensive summary of algorithms, as well as software toolboxes used for fMRI supporting different processing strategies, is presented.

In my work, ICA is performed using the Group ICA Of fMRI Toolbox (GIFT)² toolbox [67] implemented in MATLAB. It was released in 2004 and by now (October 2019) it has been downloaded 15503 times independently by researchers all over the world. Its most recent stable version that is currently used is GroupICAT v4.0b (Feb 20, 2017).

The GIFT toolbox is widely used in fMRI works for applying ICA, as it incorporates many ICA algorithms, Group ICA implementations as well as the ICASSO software [68] necessary for determining the reliability of the ICA components, as will be further described in Section 4.4.4.

4.4.3 Processing Algorithm

Algorithms that use nonlinear functions to generate higher-order statistics have been the most popular ICA approaches. There is a number of algorithms based on (i) maximum-likelihood estimation, (ii) maximization of information transfer, (iii) mutual information minimization, and (iv) maximization of non-Gaussianity. It is worth mentioning that these algorithms differ in the way that they find the directions in which the projections of the input multidimensional data have “interesting” distributions. In the ICA model, it is assumed that the least interesting distributions are those that resemble a Gaussian.

In GIFT, algorithms belonging to all four categories have been implemented. It is possible to choose between 12 implemented ICA algorithms, including Infomax, Fast-ICA, ERICA, SIMBEC, EVD, JADE OPAC, AMUSE, SDDICA, Semi-blind Infomax, Constrained ICA, Radical ICA and COMBI. As already shown by [69], FastICA and Infomax³ are the most commonly used and give the best overall

²GIFT: <http://trendscenter.org/software/gift/>

³An example of applying the Infomax algorithm is given in the Appendix A

performance when being applied to fMRI data. Thus, these two were mostly explored for being applied to fUS data, concluding to the choice of Fast-ICA [16].

4.4.3.1 Fast-ICA

Fast-ICA is a fixed-point algorithm proposed by Hyvärinen and Oja [16]. It is based on the optimization of a nonlinear contrast function measuring the non-Gaussianity of the source. The popularity of the FastICA can be attributed to its simplicity and flexibility in choosing the nonlinearity function.

More specifically, FastICA is based on a fixed-point iteration scheme for finding a maximum of the non-Gaussianity of $w^T x$. For one-unit (one-component) estimation, the Fast-ICA learning rule finds a direction, i.e. a unit vector w such that the projection $w^T x$ maximizes non-Gaussianity. Non-Gaussianity cannot be directly measured, so the approximation of negentropy or kurtosis is commonly used. In the current implementation, the use of negentropy, is considered the optimal estimator of non-Gaussianity, as it is justified by its statistical properties. Negentropy is based on the information-theoretic quantity of differential entropy.

So, the approximation of negentropy used, called also contrast (contrast to Gaussian distributions) function, is $J(w^T x)$ given as follows:

$$J_G(w^T X) \propto [E(G(w^T X)) - E(G(v))]^2 \quad (4.1)$$

where G is a non-linear function used for measuring non-Gaussianity, and v is a Gaussian variable of zero mean and unit variance.

4.4.3.2 Advantages of Fast-ICA

The selection of the Fast-ICA algorithm is also based on the following three points:

- Faster convergence:
FastICA allows for fast rates of convergence, even faster than of the other algorithm widely used in fMRI data, Infomax. The reason why the algorithm converges quickly is that it seeks for a component one by one. The convergence speed is cubic (or at least quadratic), whereas in other ordinary ICA algorithms based on (stochastic) gradient-descent methods, the convergence is linear.
- Less free parameters:
Contrary to gradient-based algorithms, there are no step-size parameters to choose for achieving convergence.
- More component distributions possible:
FastICA can estimate both sub- and super-Gaussian independent components, which contrasts with the ordinary maximum-likelihood algorithms that only work for a given class of distributions.

4.4.3.3 Fast-ICA Parameters

- Symmetrical or deflatory strategy:

There are two different approaches in order for the components to be extracted, the deflation and the symmetric algorithm. The deflation approach extracts successively the ICs one by one under orthogonality conditions. This is the way followed by the majority of ICA algorithms. The symmetric approach extracts the components simultaneously or in parallel.

Both approaches were tested on fUS data without observing any significant differences in the spatial maps. So, the symmetrical approach was used as being usually considered superior to the deflation-based FastICA and to check one of the main characteristics that changes in contrast to Infomax [70].

- Non-linear function:

When applying ICA, a suitable non-linearity measure g should be selected [71], [72]. To measure non-Gaussianity, FastICA relies on a non-quadratic nonlinear function G , its first derivative g , and its second derivative g' . There are four options for the nonlinearity function depending on the nature of the extracted sources. The first function is the nonlinearity $g(z) = z^3$ (pow3), using the kurtosis measure as an optimizing criterion. The classical skewness measure uses the function $g(z) = z^2$ (skew). The more slowly G grows as its argument increases, the more robust is the estimator. Then, the functions $g(z) = \tanh(az)$ (tanh) and $g(z) = z \exp(-az^2/2)$ (gaus) grow, too, more slowly and thus they give more robust estimators and are well-applied functions in fMRI cases.

However, it is not very likely that all sources are either light-tailed, heavy-tailed or skewed or even that the knowledge about these properties is available. So, the use of only a single nonlinearity g for all different components seems questionable. An advantage of Fast-ICA is that the algorithm finds directly independent components of any non-Gaussian distribution using any non-linearity g .

In this work, the “tanh” nonlinearity measure is used for the ICA implementation.

4.4.4 Number of Independent Components (ICs) – Model Order

The fundamental question is the determination of the number of independent components (ICs) to produce. ICA analysis can produce a large number of components. Based on literature and given the multiple ICA variability sources, the main goal is to extract the most robust and reproducible components and determine the ones with biological relevance [73], [74].

This problem can be split into two parts:

1. what dimension should be selected for reducing the fUS data into before applying ICA (i.e. determining the effective data dimension), and
2. what is the most informative number of components to use in ICA analysis

For ICA, it has been shown that choosing a too small effective data-dimension might generate “fused components”, not reflecting the real data heterogeneity and leading to a at reduction of the interesting sources (under-decomposition). On the other hand, choosing a too high number as the effective dimension may lead to signal-to-noise ratio deterioration, overfitting and splitting of the meaningful components (over-decomposition). Thus, it was decided to use only the number of reproducible components as the optimal estimate of the data dimensionality.

Methods based on the application of information-theoretic criteria to the eigen-spectrum (already mentioned in Section 2.2.3) can provide a good estimate of the dimensionality of the data, but only if the covariance of the noise is known [75]. In most cases, when noise is not known, the estimated number of sources tends to be equal to the number of time points, which is considered an unrealistic condition. Then, when ICA is applied on the original high-dimensional data, the extracted sources may have been split into multiple components; a fact which leads to the need of prior data reduction.

Consequently, in my work, to evaluate the performance of ICA, I mainly examined the three following aspects:

1. the stability of the computed components after multiple runs of ICA
2. the conservation of the computed components by varying the choice of the reduced-data dimension
3. the reproducibility of the resulting set of ICA components across multiple datasets of the same experiment.

4.4.4.1 Components Stability

The quantitative measures of IC stability obtained with the software package, ICASSO, were used to facilitate the determination of the optimal number of components to be extracted by the ICA algorithm. Through ICASSO, ICA is run multiple times using the selected training parameters, but the data is bootstrapped and/or the initial conditions of ICA are changed each time. The estimates are clustered according to their mutual similarities. More specifically, absolute correlation is used as the similarity measure among the IC estimates and agglomerative clustering with average-linkage criterion in order to identify the cluster of IC estimates attributing to the same underlying independent source. The reliable IC estimates are obtained by retrieving the centrotpe of each cluster, in other words the estimate that is most similar to other estimates in the cluster.

ICASSO also provides quantitative evaluations on the compactness of the clusters of IC estimates, which is useful for validating components' order with respect to the stability of ICA estimation. A compactness index close to unity indicates that the estimation is stable and consistent, i.e., similar components are estimated at each run of the ICA algorithm. As a result, ICASSO can rank the estimates accordingly and visualize the similarity graph between all the estimates and their partition into clusters (as shown in figures 4.3, and 4.4). Clusters are indicated by convex hulls.

Based on the principles of ICASSO, a comparison of different ICASSO results is further presented in order to improve the components' estimation, to rank the components based on their stability and finally to select the optimal number of ICs. The proposed pipeline was dependent on a fundamental parameter M , that is defined as the effective dimension of the data and, at the same time, on the number of computed independent components whose effect on the stability of the ICs is investigated. The values of M equal to 20, 30, 50 and 100 were considered, keeping data variance at around 37%, 41%, 46% and 56%, respectively. For each value of M , the data dimension was reduced to M by PCA after the appropriate pre-processing steps had been applied. Then, ICASSO was applied on each fUS dataset separately, running ICA 100 times (i.e. 100 resampling cycles).

Results

More specifically, in this work, the cluster quality index (Iq) of the selected components from ICASSO-runs was used to assess the ICs individual stability and the average of all Iq's was used to measure the overall stability of the whole ICA decomposition. Thus, after comparing the ICASSO runs with different IC-parameters according to that perspective, the selection of a number of ICs around 20 was considered the optimal choice which will be further supported by the following visualization results.

In case of 20 ICs, the extracted results of ICASSO are shown in figures 4.3 and 4.4.

In figure 4.4, the curve formed from the individual components as a function of the quality index is an L-curve, which is a trade-off curve between the two quantities, the total number of ICS and Iq values, that should be both optimized. As also shown in the results in Appendix A, in cases where more ICs are estimated, the ordered stability index generally drops off sharply. That allows us to estimate the optimal number of components, by keeping those whose stability index is above a cut-off point. Visual inspection of the ordered stability plot facilitates the selection of the cut-off point. As a visually inspected result, a number of 15-20 ICs was optimally selected.

The set of spatial maps, derived from the ICA algorithm when searching for 20 components will be further used as a reference in the rest of the thesis. The spatial maps depicted in figure 4.3 are shown in a descending order based on

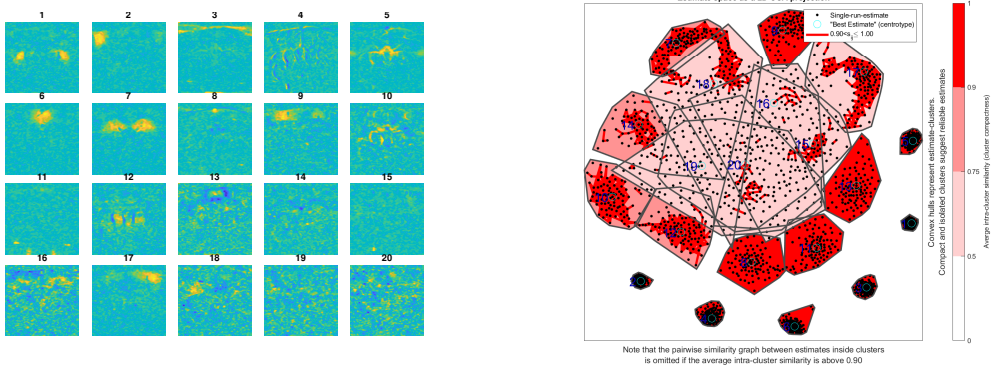


Figure 4.3: A visualization of the produced ICA spatial maps and their estimate clusters produced by ICASSO. The most stable components are shown first in the left sub-figure, and in more dense clusters in the right sub-figure.

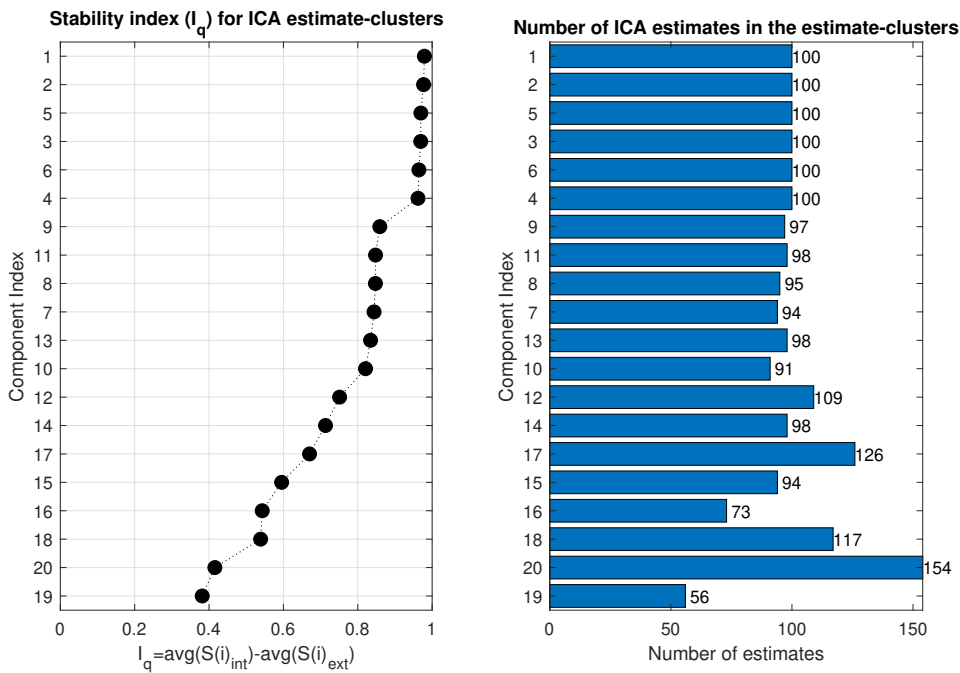


Figure 4.4: Stability (quality) index (I_q) graph for each estimate-cluster, ranking the corresponding ICA estimate (left) and indicating how many times each estimate was found (right).

their I_q values. So, the most stable components are displayed first. The number above each map represents the order that they were extracted from ICA, and in all the other figures they are characterized by that number. Moreover, the maps'

intensities were normalized to have a maximum value of 1, a procedure followed in all the spatial maps in the rest of the thesis. The corresponding results obtained for ICs equal to 10, 15, 30, 50 and 100 are given in the Appendix A for further visual inspection.

The stability of the components derived from ICASSO runs with different IC parameters was checked by comparing the produced by ICASSO index quality (Iq) values and components' similarity. For similarity, correlation in both space and time was computed. In all correlation-based comparisons, the absolute value of the correlation coefficient was used. From the set of 20 spatial maps, some were observed to represent a clear anatomical region, some followed the vessels structure and some were more noisy without specific activations. The most compact and clear ones, that seem to represent particular anatomical regions, were selected as the most "interesting" components to be further analysed. More specifically, as displayed in figure 4.3, the spatial maps with numbers 1, 2, 6, 9, 7, 12, 17 were selected.

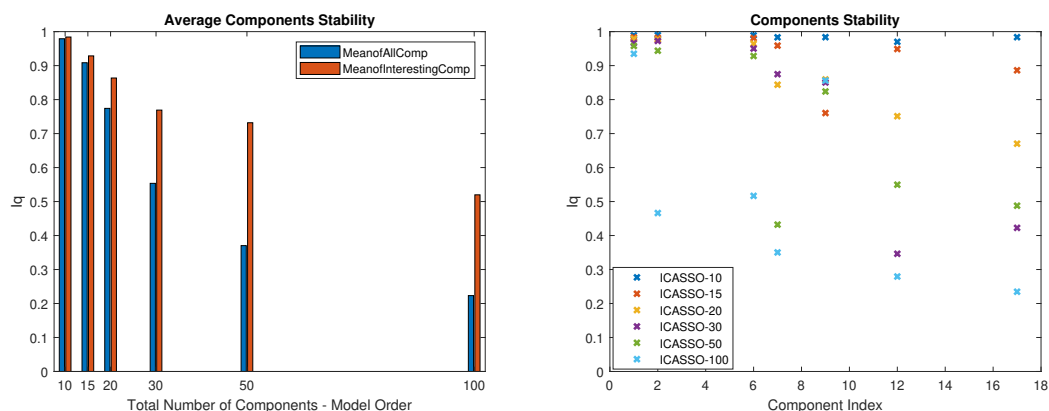


Figure 4.5: Components' Stability. Left: Mean Iq values for all and a subset of interesting components when running for 10, 15, 20, 30, 50 and 100 ICs. These 6 cases are called ICASSO-10, ICASSO-15, ICASSO-20, ICASSO-30, ICASSO-50 and ICASSO-100 respectively. Right: Iq values separately for all the interesting components in each different ICASSO case.

The graphs in figure 4.5 can justify the selection of components in a range of 15-30 because of the high Iq values. On the left side of figure 4.5, the mean Iq values of all extracted components is almost linearly decreasing when searching for a higher total number of ICs. That is a reasonable result because, when extracting more ICs, we expect a high number of them to be less significant and so the mean Iq value will decrease. The mean Iq value of the corresponding interesting components found in all different ICASSO runs was also decreasing when searching for more ICs. On the right side of figure 4.5 are depicted the Iq values of each component separately. It is again justified that, mostly when searching for ICs 50

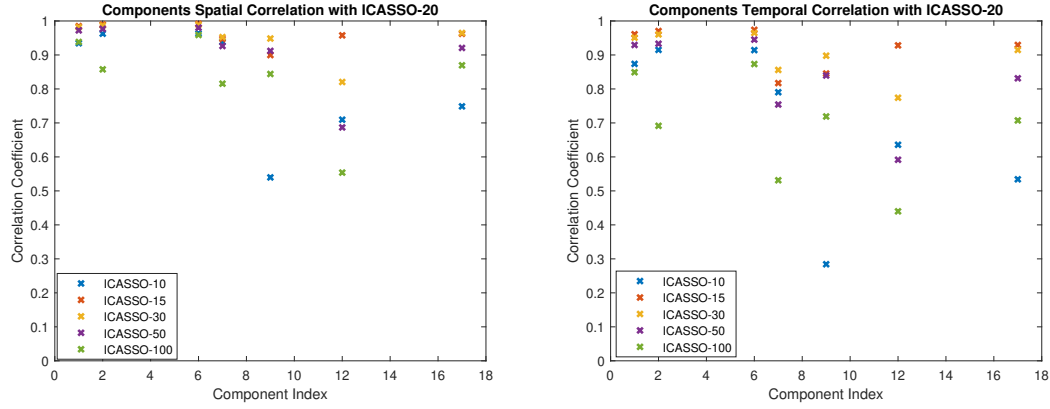


Figure 4.6: Correlation Comparisons. Left: Spatial correlation coefficients of all the interesting components when running for 10, 15, 30, 50 and 100 ICs with the case of 20 ICs. Right: Temporal correlation coefficients of all the interesting components when running for 10, 15, 30, 50 and 100 ICs with the case of 20 ICs.

and 100, some low I_q values were observed. In case of 10, 15 and 20 ICs, all the I_q values are above 0.7. Thus, the initial choice of 20 ICs was proven reasonable.

Regarding only the corresponding interesting components, the spatial and temporal corresponding correlation of ICASSO-10, ICASSO-15, ICASSO-30, ICASSO-50 and ICASSO-100 with the optimal ICASSO-20 were examined. Corresponding correlation, derived when a component is correlated with all the components in another set and the maximum correlation found are selected. The spatial correlation, in figure 4.6, showed that the spatial maps were quite similar, all having a correlation coefficient above 0.5, and apart from one map, the rest had a value higher than 0.8. From the temporal correlation in figure 4.6, it is indicated that the closer the number of components goes to 20, the more it differs in their corresponding time-series.

4.4.4.2 Component Conservation

Moreover, the effect of several different PCA components was investigated by repeating ICA analysis using a fixed number of ICs. For example, for the reference dataset previously used, the number of 20 ICs was selected in an ad-hoc manner. Subsequently, the results of a prior data reduction using 20, 30, 50 and 100 PCA components were compared for a final 20-ICs decomposition. The optimal choice of PCA components relied always on finding the most reliable components and for keeping the computational complexity as low as possible. The complexity and processing time increases with the number of PCA components, especially when running ICA for 100 times using ICASSO.

On the left side of figure 4.7, only the average I_q values of the interesting

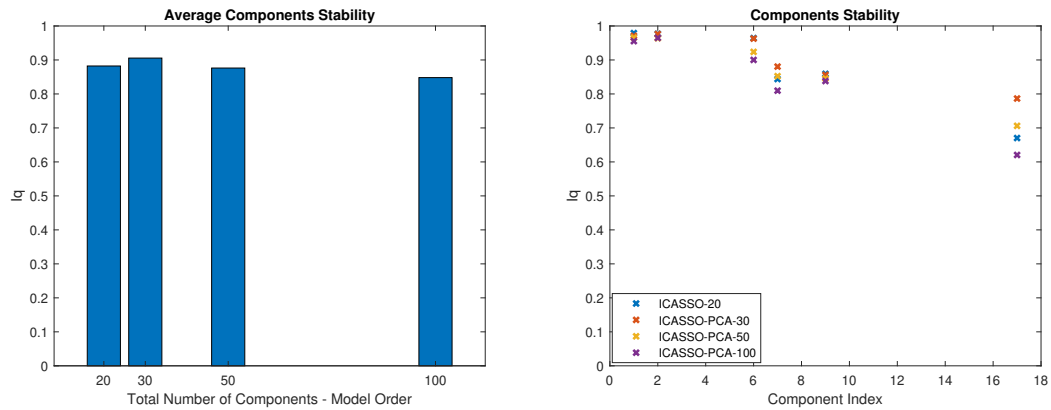


Figure 4.7: Components' Stability for PCA. Left: Average Iq values for all the subset of interesting components when using 20, 30, 50 and 100 PCA components. Right: Iq values separately for all the interesting components in each different ICASSO case.

components are shown, instead of displaying the Iq values of all the components like in figure 4.6. When PCA dimensionality was increased, more components were found with infinite index quality, making it impossible to compute the average of all. This occurred when components appeared only once (number of estimates = 1) in all the resampling cycles.

Here, the maximum Iq was found for 30 PCA components, but in all other cases Iq values were close, all above 0.8. However, as shown on the right side of figure 4.7, when examining the Iq values of the interesting components separately, these were mostly higher in case of using 20 PCA components.

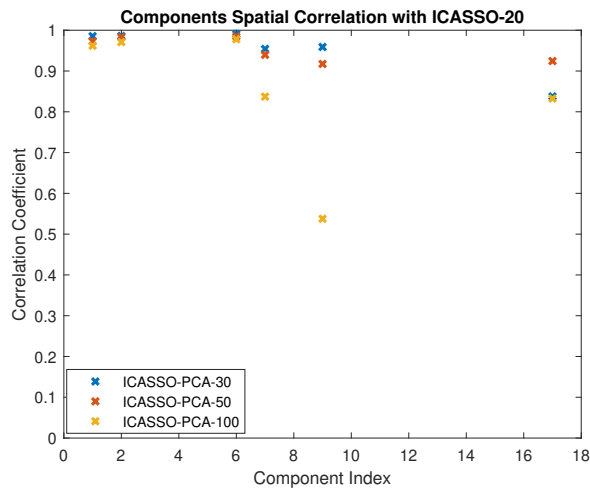


Figure 4.8: Spatial Correlation of each of the interesting components when using 30, 50, 100 PCA components with the case of 20

A number of PCA components close to the range of 20-30 seems a reasonable choice for a data-reduction, prior to applying ICA, without having significant invariances in the produced results. Thus, the same number of PCA and ICA components (20) was kept in the following analysis of the same type of datasets. That was confirmed by several studies which also used the same number for PCA and ICA components [76].

Besides, it is believed that the most interesting components for interpretation are usually positioned within the first few top ranks (components), therefore 100 seems to be a quite high limit for testing dimension reduction when applying ICA to fUS data.

4.4.4.3 Component Reproducibility

Subsequently, the components' reproducibility across the 5 datasets was examined. The detected as "interesting" components were checked for whether they can be found in different datasets.

To identify the reproducible components, we applied the same methodology for ICASSO with the previously set parameters, reduction to 20 PCA components and search for 20 ICs. That methodology was applied to five different datasets obtained from the same experiment and the same animal subject.

For the reproductivity evaluation, the five datasets were decomposed separately and then the "interesting" components were examined for their stability values (figure 4.9) and their corresponding correlations (figure 4.9) were calculated.

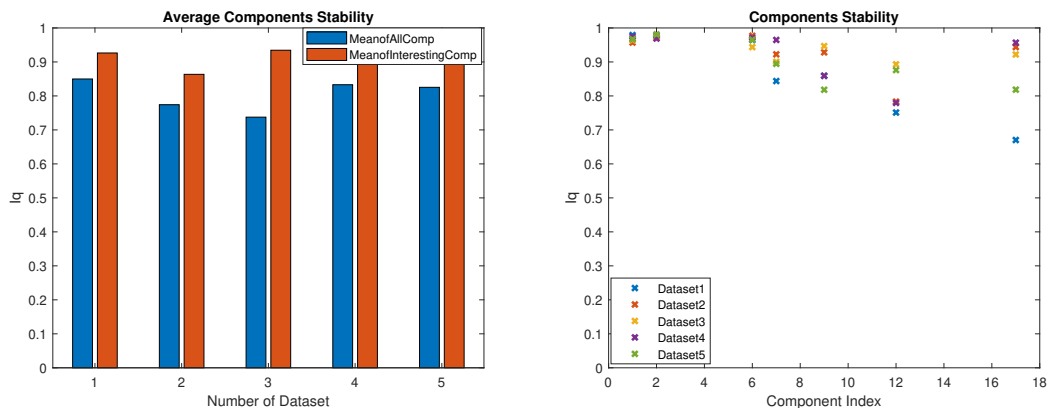


Figure 4.9: Datasets' Reproducibility. Left: Average Iq values for all and a subset of interesting components, when running for 20 ICs in each different dataset. Right: Iq values separately for all the interesting components in each different dataset.

The reproducibility analysis indicated that all the components recognized as interesting were found highly accurately in all five datasets. In figure 4.9, the mean stability value of the interesting components was approximately 0.9 in all datasets

and it was also higher than the overall mean stability in each dataset.

On the right side of figure 4.9, the stability iq value of each interesting component was examined separately and was found to be quite high. The first three components (1, 2, 5 in order) were the most stable ones reaching an Iq value above 0.95 while the values of the other ones were more spread out, but apart from one case, all were above 0.75.

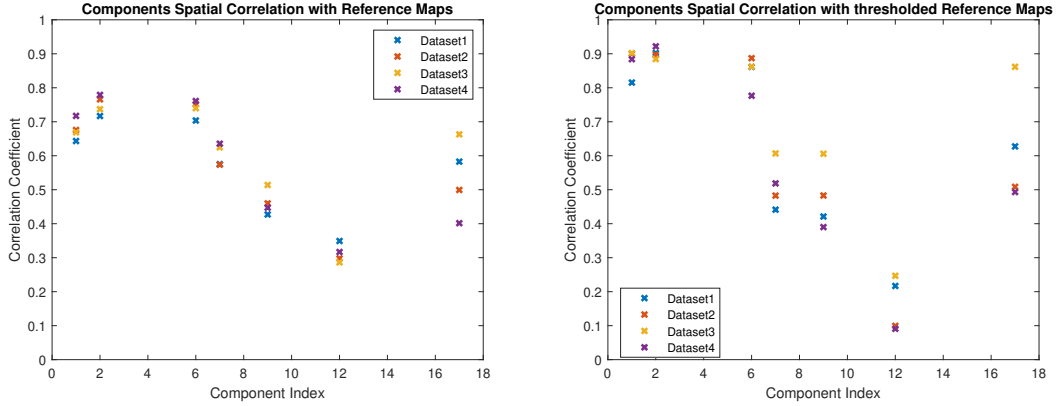


Figure 4.10: Spatial correlations between all the datasets with the reference dataset, analyzed in Section 4.4.4. Left: The reference maps were unthresholded. Right: The reference maps were thresholded.

Then, the spatial accuracy of the sources was evaluated by performing a spatial correlation with each of the originally selected template maps. The corresponding correlations of the interesting components' unthresholded spatial maps are shown in figure 4.10. The correlation values of each component were quite close for each dataset. However, their values were found not to be very high, ranging from around 0.3 to 0.8. These low values may have been influenced by the low-intensity pixels, although visually the components seemed very similar (see Appendix A). These pixels were around the main anatomical high-intensity region and were differed in each dataset. Thus, it was important for the thresholded spatial maps to be examined as well. The corresponding spatial correlations in that case are shown on the right side of figure 4.10. The values were relatively higher, especially for the clearer components.

4.4.5 Group-ICA

4.4.5.1 Group-ICA Methodology

The data is organized in a temporal-concatenation mode and then the subject-specific results are derived by back-reconstruction using a PCA-based approach. It is indicated that temporal concatenation usually works better for fMRI data, mainly because the temporal variations in the fMRI signals are much larger than

the spatial variations [30]. Therefore, the same concept is believed to be valid for fUS data as well.

Regarding the formulation of the mathematical problem, we denote Y_i as the preprocessed data matrix of each subject i , of T -by- V dimension, where T is the number of time-points and V is the number of voxels. After the first PCA-reduction step, Y_i^* represent the T_1 -by- V PCA-reduced data for each subject i , where $Y_i^* = F_i^T Y_i$, F_i^T is the T_1 -by- T standardized reducing matrix and T_1 is the selected number of principal components retained for each subject.

The same data is collected on M subjects and are temporally concatenated in

$$Y^* = [Y_1^*, Y_2^*, \dots, Y_M^*]^T \quad (4.2)$$

Then, the aggregated data is again PCA-reduced, represented by

$$X = G^T Y^* = [G_1^T, \dots, G_M^T] \begin{bmatrix} F_1^T Y_1 \\ \vdots \\ F_M^T Y_M \end{bmatrix} = \sum_{i=1}^M G_i^T F_i^T Y_i^T \quad (4.3)$$

where G^{-1} is the T_2 -by- MT_1 standardized reducing matrix. As reported in [30], ideally T_2 is selected to be equal to the true number of ICs for all subjects, and each subject has the same components. The X matrix is then used as the ICA input to be decomposed. In a noise-free ICA model, we estimate the mixing matrix \hat{A} and the common between subjects SMs \hat{S} according to:

$$X = \sum_{i=1}^M X_i = \sum_{i=1}^M G_i^T F_i^T Y_i = \hat{A} \sum_{i=1}^M S_i = \hat{A} \hat{S} \quad (4.4)$$

To back-reconstruct the subject-specific SMs S_i and TCs R_i using the GICA3 approach, it is assumed that subject-specific TCs are the subject-specific PCA back-projected mixing matrix

$$R_i = F_i G_i^T \hat{A} \quad (4.5)$$

$$S_i = \hat{A}^T G_i^T F_i^T Y_i = \hat{A}^T G_i^T Y_i^* \quad (4.6)$$

Moreover, it should be noted that the ‘‘common’’ SM \hat{S} is the sum of the subject-specific SMs,

$$\hat{S} = \sum_{i=1}^M S_i \quad (4.7)$$

4.4.5.2 Group-ICA Parameters

First, a PCA data reduction was done in two steps where firstly the data were reduced, followed by their concatenation in groups. Each individual-subject dataset was PCA-reduced selecting 20 as the number of components, resulting from 1,143 timepoints to 20 timepoints. Then, the reduced datasets of every subject were concatenated together into an aggregate dataset, resulting in an 18,939-by-100 (pixel-by-time) matrix. That matrix was further reduced, using PCA, to a dimension equal to 20 that is equal to the number of ICs. Consequently, that matrix represents the input of the ICA algorithm for estimating the SMs and TCs at a group level. Lastly, a back reconstruction of the data to single-subject SMs and TCs was implemented.

It is obvious that the final between-subject differences and resulted inferences become dependent on the initial subject-specific reduction stage.

4.4.6 Post-processing Steps

The well-applied methods used in fMRI were difficult to be applied in our case, because the two images, that were about to be registered, were not only multimodal, meaning that were captured by a different imaging modality, but also contained information of different formats. The reference image was a labeled map and the target image was the vascular map of the brain (PDI). The atlas used was the Allen Mouse Brain Reference Atlas⁴ (ARA). An example of the digital information incorporated into the atlas is given in figure 4.11.

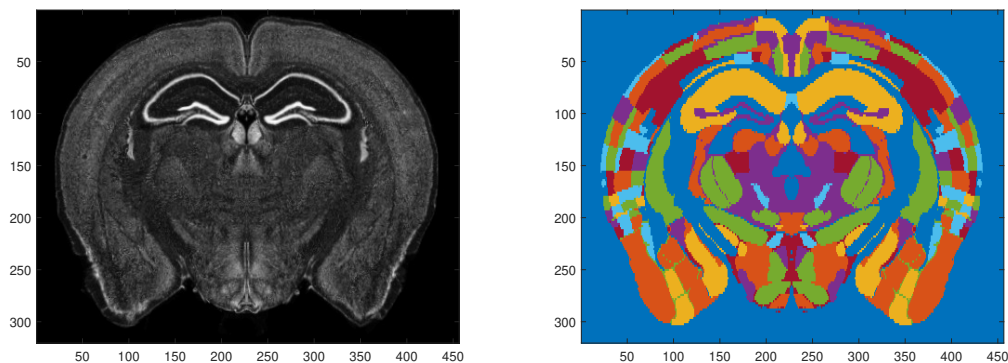


Figure 4.11: The corresponding to our dataset structural slice (left) in atlas and its annotated volume (right). Every color has a different label number that represents a brain region.

So, a simple solution to that could be the usage of some landmarks in the vascular map corresponding to specific points in the reference image. As landmarks

⁴<https://portal.brain-map.org/>

were defined some of the detected blood vessels approximating the shape of known and well-identifiable structures in the brain.

In Matlab, that was performed using the Control Point Selection Tool which has a user interface in order to manually select control points in the PDI (moving image) and the corresponding slice in atlas (fixed image). The selection procedure is shown in figure 4.12. Then, an appropriate estimation of the geometric transformation (like similarity, affine, projective) was selected to bring the moving image into alignment with the fixed one. In our case, after similarity, the result was a transformation matrix that was further used for PDIs as well as ICA spatial maps of the same dimensions. The registered PDI is shown in figure 4.13.

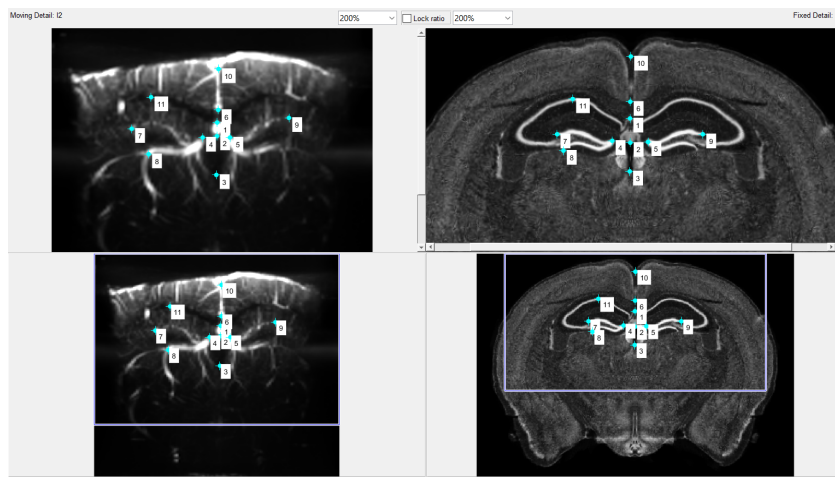


Figure 4.12: Control Point Selection Tool user interface

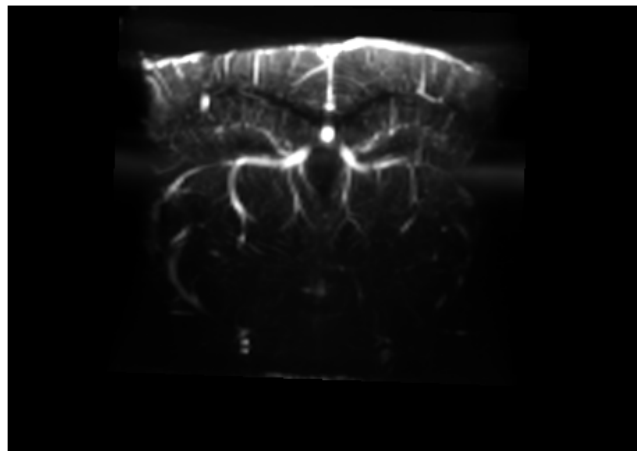


Figure 4.13: PDI-Registered to Atlas

After the experimental process we follow has been established in Chapter 4, through appropriate use of ICA, we proceed in this chapter to investigate different fUS experiments and assess our method's performance and findings. The first experiment was a 2D visual-stimulation experiment, for which 5 different datasets were obtained in order to be examined separately as well as in a group. On these five datasets, the produced components were examined, first with regard to the spatial domain by interpreting the anatomical regions represented, and then to the temporal domain by investigating their task relevance. Afterwards, the differences in spatial maps as well as in temporal-series were tested on an ICA group approach. For an additional group comparison, a slightly different experimental condition (one-side visual stimulation) was also examined. Finally, a 3D (or 4D, space by time) resting-state experiment was conducted for examining the discrimination of regions in adjacent brain positions. All the experiments were obtained from the fUS setup building at the Erasmus MC.

5.1 2D Visual-Stimulation Experiment

The 2D visual-stimulation data was first analysed in Chapter 4 for determining all the ICA key choices, such as the optimal number of ICs. ICA was applied separately in each dataset and the results were assessed for reliability and reproducibility due to the advantage of having multiple similar datasets of the same subject. Each dataset contained 1,143 PDIs, with a frame size of 256×128 pixels.

In this chapter, single-ICA was used for the first-level analysis of the produced components. The components were investigated in space and time for the anatomical regions represented and their task relevance, respectively. However, single-ICA cannot be used for reliable inter-group comparisons because finding the corresponding ones across subjects is not so straightforward [77]. Sometimes, merging some of the produced components is a necessary strategy to deal with that problem.

Subsequently, these five datasets could be easily tested for the effects that Group-ICA has on them. Group-ICA has been well-studied in the case of fMRI and the Group-ICA's results can be better compared than when separately analysed. Although the estimated spatial patterns of the most clear components are well-represented, in general subject variability in space, time and amplitude leads to a great components-matching problem.

5.1.1 Single-ICA

ICA was performed separately on each of the five datasets. The ICs used were derived after 100 ICA runs through ICASSO because they are considered as more reliable results than those from an arbitrary run. From the 20 reference spatial maps (shown in figure 4.3), the seven most “interesting” components with numbers 1, 2, 6, 7, 9, 12, 17 are shown in figure 5.1, and are further used in this chapter as well. The seven most interesting components were selected for further analysis as they were the most dense and distinct distributed maps, consider to resembling separate anatomical regions.

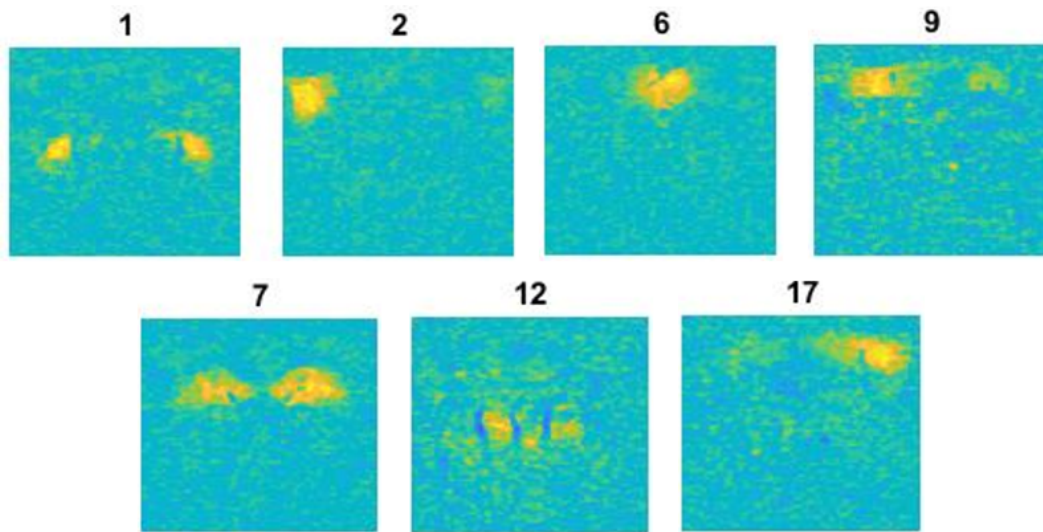


Figure 5.1: The seven interesting spatial maps derived from Section 4.4.4, selected as the most dense and distinct distributed maps

5.1.1.1 Components Anatomical Interpretation

The first approach in analyzing the produced components was through their spatial maps. Thus, according to their activated regions, the interpretation of the interesting ones against actual anatomy was investigated. The spatial analysis aimed to provide an anatomical understanding of each one of the already recognized as interesting ICA components.

After combining the seven components, it is quite clear that they together shape the structure of the brain. Brain structure of the reference dataset’s components is depicted in figure 5.2.

It is obvious that a part in the center of the brain structure of figure 5.2 was not discovered in the components. This is anatomically explained because that region

is part of the cerebral ventricles network (third ventricle¹). Ventricles are brain cavities where no vessels exist and so cannot be captured by fUS.

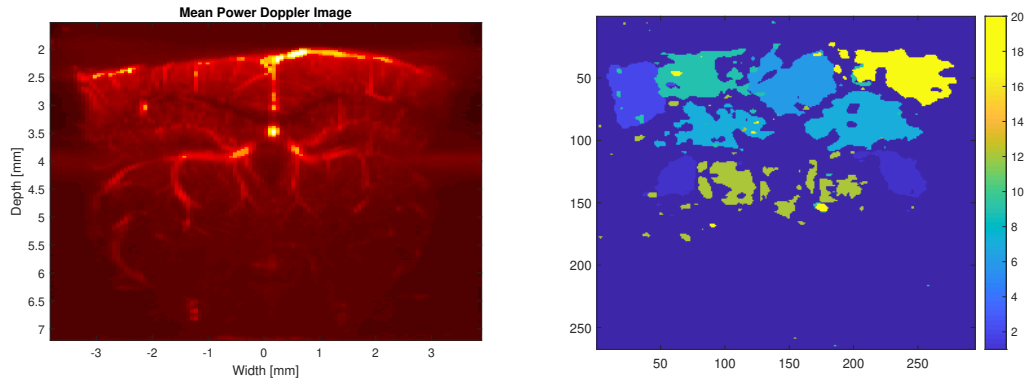


Figure 5.2: Left: Vessels structure originally captured by fUS. Right: Shape of brain structure after merging the 7 interesting components (shown in figure 5.1).

Each component was separately examined for identifying the real anatomical region that they represent. In each case, the activated region was superimposed with the annotated atlas slice and the underlying atlas labels were selected and gathered to a matrix.

Due of the atlas structure, for each component the labels of very small regions were uncovered, so these labels were further grouped into bigger brain regions. To achieve that, additional information was used regarding the hierarchical organization of brain structures; the atlas brain structures were stored in a deeply nested data structure which held the needed hierarchy. A schematical representation of the brain structure hierarchical tree is shown in the Appendix B.

Regarding this procedure, label merging was performed after first checking the parent labels of the ones initially found (low-level labels in hierarchy). According to the atlas structure, if all the labels with the same parent label that are present in the particular slice were found, these could be replaced with the parent label. Thus, higher-level and more recognizable regions were finally identified in each component. The same procedure was repeated until finding the labels of the highest possible level in the atlas structure hierarchy. The final sub-regions of each component are analyzed in more detail in the following part.

Despite the merging of smaller regions into bigger ones, the total number of labels found for each component was still high. As the map has activated pixels, whose intensity is not zero, scattered all over the brain, less significant labels have

¹<http://atlas.brain-map.org/atlas>

also been found. Thus, a proper measure had to be established in order to keep only the significant ones. For this reason, additional information regarding each label was also collected for each component's label, such as mean intensity value, number of activated pixels (label's coverage) and the spatial overlap between PDI and atlas label's region using the dice similarity measure. Dice similarity is a common computational way to measure the level of spatial overlap between two binary maps [78]. The value of that ranges from 0, indicating no overlap between the spatial map of the component and the label's region, to 1, indicating complete overlap.

From all this information, two filtering strategies to make the co-registration process less noisy were finally used (i) the overlap between PDI and atlas pixels and (ii) mean intensity. For every label found, dice similarity of the real label map and the component spatial map was computed. More specifically, labels with similarity larger than 0.2 were kept, after having examined different values of similarity threshold. Additionally, the mean intensity of each label's region plays an important role. So, for calculating the similarity values, the whole component map was thresholded (intensity values $|z| < 0.3$ were cut-off) to isolate the most activated area.

For each of the seven interesting components, the maps of the most significant low-level labels and the subsequently merged regions are shown next, in figures 5.3-5.9 along with matching tables which include their corresponding names and acronyms.

Component 1

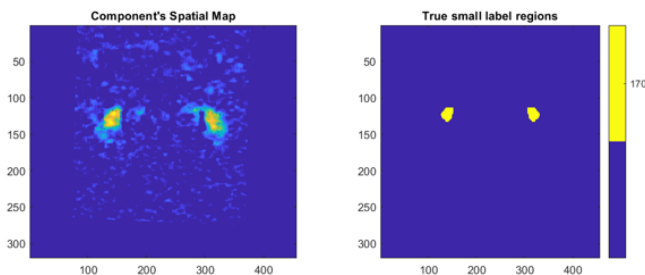


Figure 5.3: Component 1: the IC spatial map, all the low-level labels and the interesting labels finally selected

Label	Name
170	Dorsal part of the lateral geniculate complex (LGd)

Table 5.1: Component 1: Labels and names of the interesting regions

In this case, the bigger regions found after grouping correspond to only one lower-level (in atlas hierarchy) region, so the latter regions were considered and kept as the interesting ones. Thus, only the low-level regions maps appear in figure 5.3.

The well-identifiable LGN region from the literature is not apparent in the atlas labels. However, it is known from [79] that LGN is subdivided into two different sub-regions, the dorsal (LGv) and the ventral part (LGd). As the latter region was revealed in ICA component 1, the spatial map of this component is called LGN in the rest of the thesis.

Component 2

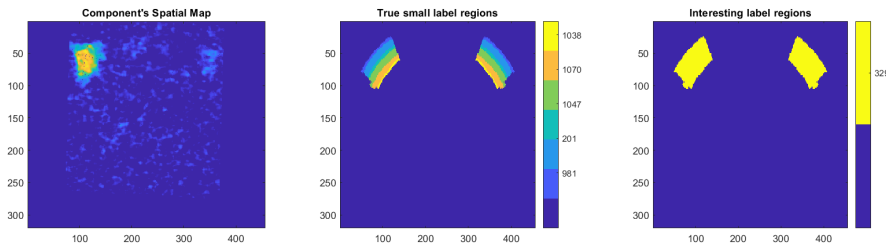


Figure 5.4: Component 2: the IC spatial map, all the low-level labels and the interesting labels finally selected

Label	Name
329	Primary somatosensory area, barrel field (SSp-bfd)
981	Primary somatosensory area, barrel field, layer 1
201	Primary somatosensory area, barrel field, layer 2/3
1047	Primary somatosensory area, barrel field, layer 4
1070	Primary somatosensory area, barrel field, layer 5
1038	Primary somatosensory area, barrel field, layer 6a
1062	Primary somatosensory area, barrel field, layer 6b

Table 5.2: Component 2: Labels and names of the interesting regions as well as their sub-regions

Since only one part of the primary somatosensory area, the primary somatosensory area - barrel field, was identified in all the interesting activated regions, label 329 will be called with the **SSp** acronym. According to anatomy, the primary somatosensory barrel cortex processes tactile vibrissae (whiskers) information, allowing mice to actively perceive spatial features of their surroundings [80].

Component 6

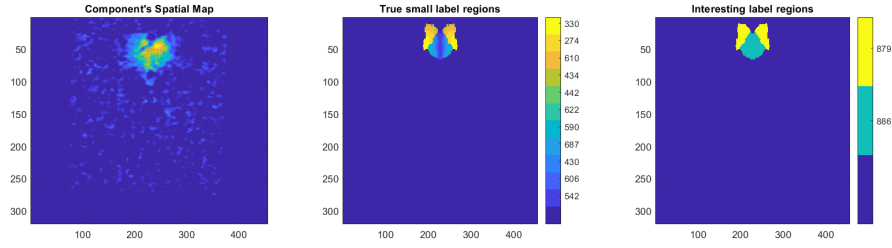


Figure 5.5: Component 6: the IC spatial map, all the low-level labels and the interesting labels finally selected

Label	Name
879	Retrosplenial area, dorsal part (RSPd)
442	Retrosplenial area, dorsal part, layer 1
434	Retrosplenial area, dorsal part, layer 2/3
610	Retrosplenial area, dorsal part, layer 5
274	Retrosplenial area, dorsal part, layer 6a
330	Retrosplenial area, dorsal part, layer 6b
886	Retrosplenial area, ventral part (RSPv)
542	Retrosplenial area, ventral part, layer 1
606	Retrosplenial area, ventral part, layer 2
430	Retrosplenial area, ventral part, layer 2/3
687	Retrosplenial area, ventral part, layer 5
590	Retrosplenial area, ventral part, layer 6a
622	Retrosplenial area, ventral part, layer 6b

Table 5.3: Component 6: Labels and names of the interesting regions as well as their underlying sub-regions

According to the atlas structure of the examined coronal slice, the RSPv and RSPd regions form the bigger Retrosplenial area (**RSP**). RSP is part of the Default mode network (DMN) and it plays an important role in spatial learning [81]. It mainly processes and stores spatial information.

Component 7

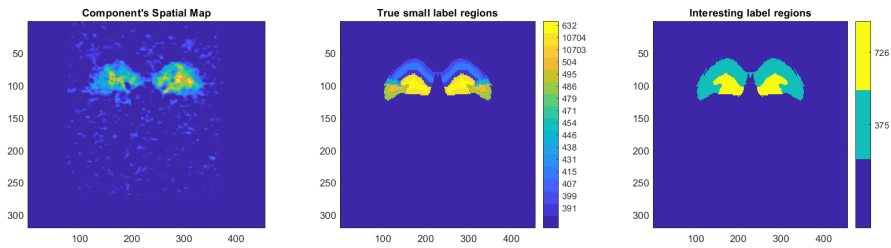


Figure 5.6: Component 7: the IC spatial map, all the low-level labels and the interesting labels finally selected

Label	Name
375	Ammon's horn (CA)
726	Dentate gyrus (DG)

Table 5.4: Component 7: Labels and names of the interesting regions.

The CA and DG regions are the most significant sub-regions of hippocampal area (Hip) because they cover most of its total map. According to the atlas structure, two other sub-regions must exist to form the whole hippocampal area, the Fasciola sinerea and Induseum griseum. However, because they are very small regions, component 7 is called **Hip** in the rest of the thesis. According to anatomy, hippocampus plays an important role in learning and memory.

Component 9

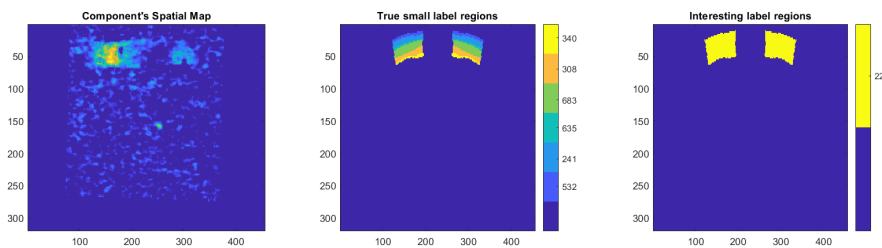


Figure 5.7: Component 9: the IC spatial map, all the low-level labels and the interesting labels finally selected.

Label	Name
22	Posterior parietal association areas (PTLp)

Table 5.5: Component 9: Labels and names of the interesting regions as well as their sub-regions

In case of a visual input, the parietal areas play a role in spatial cognition and motor control of the eyes [82]. It is known that these areas are connected with the Hippocampus for long-term memory formation.

Component 12

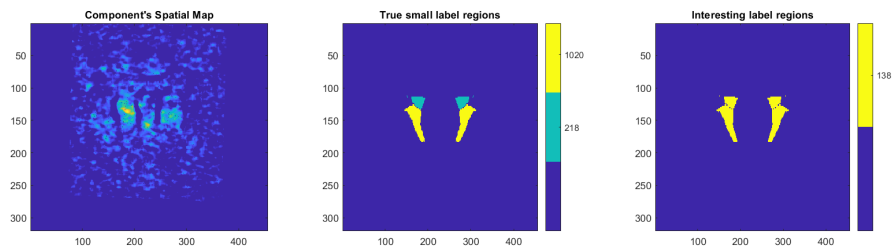


Figure 5.8: Component 12: the IC spatial map, all the low-level labels and the interesting labels finally selected

Label	Name
138	Lateral group of the dorsal thalamus (LAT)
218	Lateral posterior nucleus of the thalamus
1020	Posterior complex of the thalamus

Table 5.6: Component 12: Labels and names of the interesting regions as well as their sub-regions

The LAT region is part of the thalamus that receives input from several subdivisions of the visual cortex. It is also very close to the LGN, so it is interesting to be examined.

Component 17

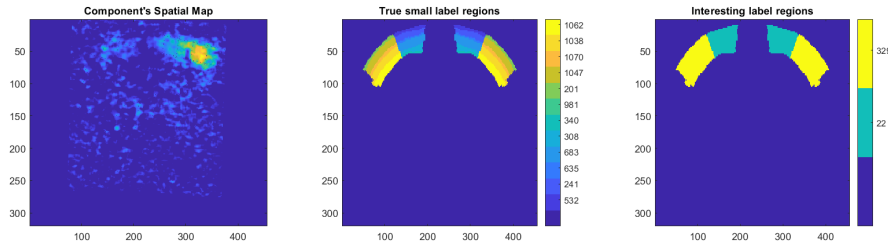


Figure 5.9: Component 17: the IC spatial map, all the low-level labels and the interesting labels finally selected

Label	Name
22	Posterior parietal association areas (PTLp)
329	Primary somatosensory area, barrel field (SSp-bfd)

Table 5.7: Component 17: Labels and names of the interesting regions as well as their sub-regions

In total, a set of 8 labels was derived. These 8 labels will be used in the rest of the analysis section. The spatial maps of the 8 labels merged in one map is given in figure 5.10, closely identifying the brain structures and resembling the ICA produced map of figure 5.2.

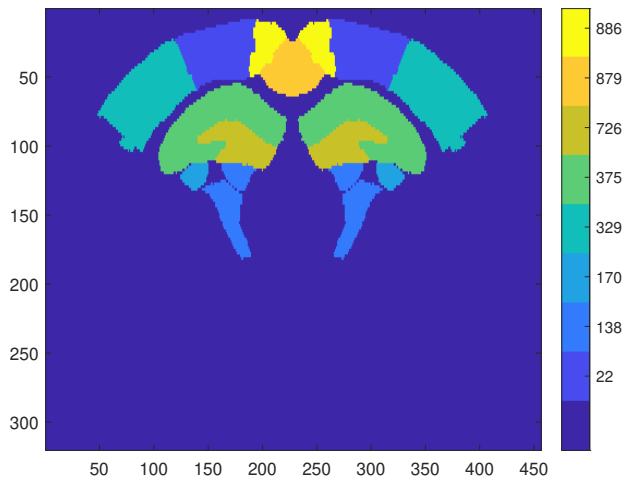


Figure 5.10: Shape of brain structures after merging the 8 interesting labels' maps

For the rest of the thesis, the seven interesting ICs will be called with the

acronyms of the regions they mostly represent. The acronym of each component is given in table 5.8.

Component	Acronym
1	LGN
2	SSp-L
6	RSP
7	Hip
9	PTL-L
12	LAT
17	PTL-R + SSp-R

Table 5.8: Acronyms of the interesting components. When a bilateral region is split into left and right sides, the acronyms contain also the letter L and R, respectively.

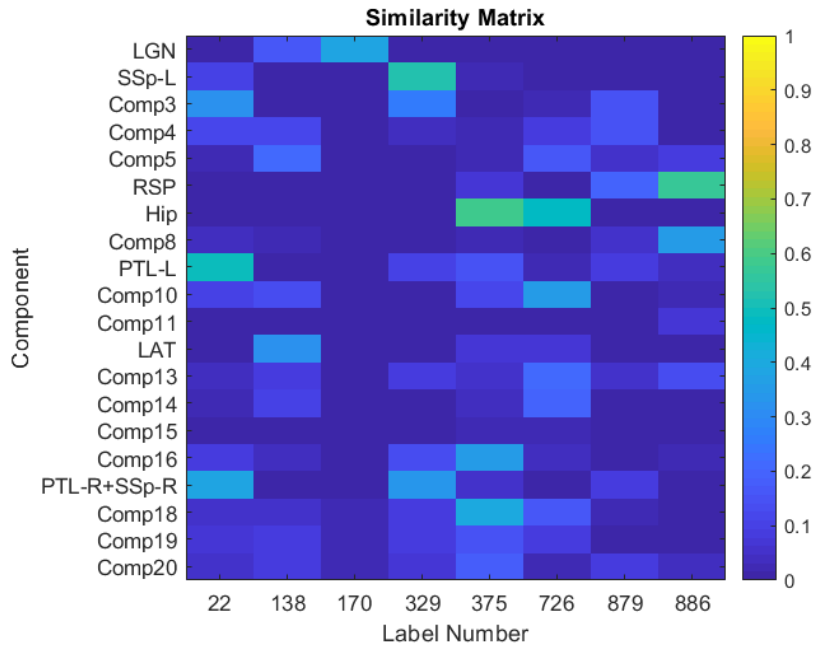


Figure 5.11: Similarity matrix of the components extracted from the reference dataset with the spatial maps of the true labels. The numbering of the components is according to figure 4.3

As a result, a similarity matrix can be constructed to summarize the labels which are represented in all the 20 ICs. The matrix, shown in figure 5.11, exhibits the dice similarity between all the components' maps (thresholded) and the 8 interesting labels-regions. That measure was the main criterion, previously used,

to collect the interesting labels of each component.

As expected, the highest values appeared in the interesting components because for these the labels were found. However, some of the labels were also found in the other components. This mostly occurs because all the maps' activated pixels are quite spread (resembling the vessels' structure, like 4, 5, 10), but there are cases where pixels' intensity in specific areas is higher. For example, label 375, initially found in the hippocampus component, was quite high for components 16 and 18, as well. After being visually checked, these components seem to have a great number of activated pixels in the same region as the hippocampus.

Furthermore, there were cases where the same labels were found in multiple components with quite high values. For instance, labels 22, 329 and 361 were all appeared in components 2, 9 and 17. These regions seemed related, being quite close to each other in the cortex area.

5.1.1.2 Component Task Relevance

Subsequently, quantitative validation results were obtained for the extracted temporal components. To examine the task relevance of the components, correlation of the time-series was computed with the pattern of the stimulus. Regarding correlation, we are interested in checking both the computed values and whether the values are scattered between datasets.

Because of the single-ICA inherent variability in the time-series, we cannot always find the corresponding components. Thus, the correlation values of the interesting components² of all the five datasets are displayed in figure 5.12. In all the datasets, the corresponding components were found based on the maximum correlation of the spatial maps with the interesting reference components.

Based on correlation, a method for ordering the components is proposed and so the general problem of the components' ordering is approached. As already described, the order of the extracted components has no particular meaning. Most of the ICA algorithms are iterative in nature so the results are based on the initial conditions of every ICA run and the components appear in a random order each time. Therefore, two different measures are proposed for solving the ambiguity of IC ordering. The first measure is the correlation of components' time-series with the stimulus pattern and the second one is the stability Iq values produced from ICASSO.

Regarding the first measure, in figure 5.13, the 7 interesting components of all five datasets are ordered based on their correlation with the stimulus pattern. As a clear result of figure 5.13, the LGN component was always found in the first rank position, meaning that it is the most task-relevant one. The LGN's relevance is confirmed neuro-scientifically by its role in the visual pathway. However, a similar

²See in Appendix B the correlation values of all the reference dataset' s temporal components with the stimulus pattern.

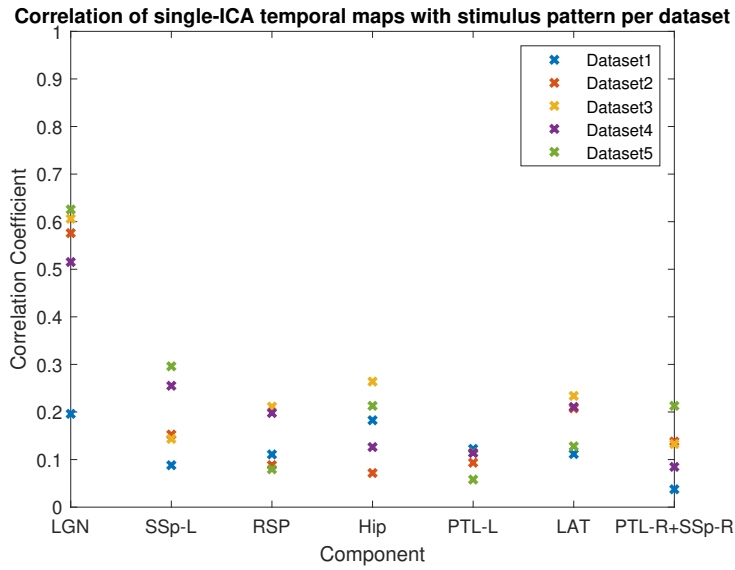


Figure 5.12: Temporal correlation of the corresponding interesting components of all the five dataset with the stimulus pattern. LGN revealed the most-task relevant component.

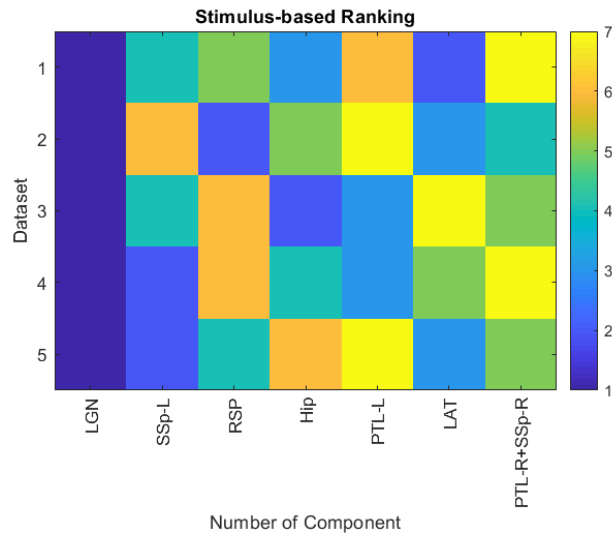


Figure 5.13: Task-relevance-based ranking of the seven interesting components in the five different datasets. In all datasets, LGN was found first in ranking.

pattern in the ordering of the other components is not apparent. This may occur because all the other regions are not known to be directly task-relevant.

Here, the fact that some sources may exhibit a relative delay in the hemody-

dynamic response compared to the supposed on-periods of the stimulation pattern was taken into account. Cross-correlation of the components' time-series with the stimulus pattern was calculated by shifting the stimulus' signal by a small number of time-frames in order to find the maximum correlation. In fMRI, it has been reported that the onset of signal activation can vary across regions [83].

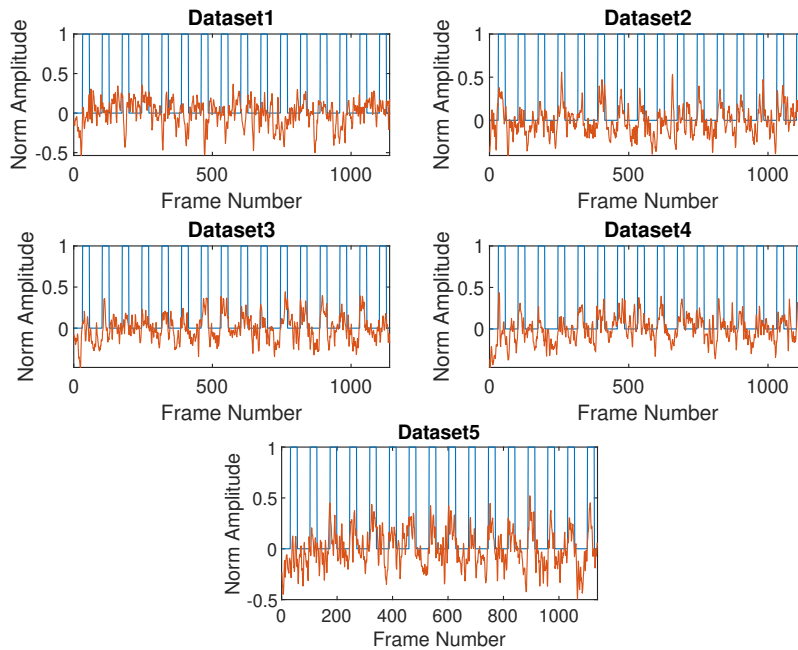


Figure 5.14: Stimulation pattern shifted by 10 time-frames is superimposed with the time-series of each dataset's LGN.

In figure 5.14, we can observe how similar the time-series of the most task-relevant LGN component is with the stimulus pattern. The corresponding correlation coefficients are shown in table 5.9. Although a low value was found in the first dataset, probably because of an acquisition problem, the LGN was found in the first rank.

	Dataset 1	Dataset 2	Dataset 3	Dataset 4	Dataset 5
Correlation Coefficient	0.20	0.58	0.61	0.52	0.63

Table 5.9: Correlation Coefficients of the LGN of each dataset with the stimulus pattern

As far as the second measure is concerned, the ambiguity of the components' ordering was considered to be approached through the stability Iq values produced from ICASSO. According to that value, the extracted components can be ordered

from the most stable to the least stable ones for each dataset. As shown in figure 5.15, we cannot easily draw a straightforward conclusion. Because Iq values were very high and very close to each other, components were not found in the same stability-based order. However, it is observed that Iq-based ranking shows much higher cohesion than the stimulus-based one. The LGN, SSP-L and RSP were almost always found to be in the first 3 positions, while the other components in the last positions.

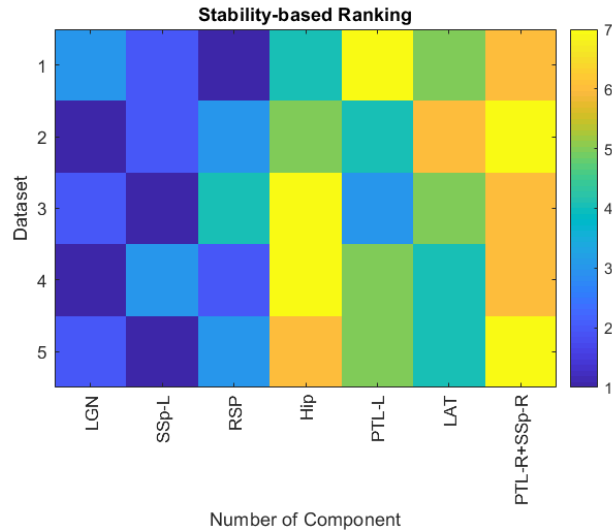


Figure 5.15: Stability-based ranking of the seven interesting components in all the different datasets

5.1.2 Group-ICA

In Group-ICA, the spatial maps and time-series of different datasets can be directly compared, because common as well as subject-specific components are presented in the same order. Thus, the group-case approach permits the identification of experiments' differences in a way that makes them comparable. Two cases of experiments were applied to group-ICA. The first case was the within-experiment group-ICA, using the 5 datasets of the same experiment and the second case was the between-experiment group-ICA examining the differences obtained in two slightly different conditions. Being in the same way stimulated, it is interesting to check the differences occurring in the task-relevant spatial maps and time-series of both experiments.

5.1.2.1 Within-Experiment

The 5 datasets obtained from the both-side visual stimulation experiment, that were separately analysed before, are applied to group-ICA after being temporal concatenated. The common spatial maps that were produced after Group-ICA analysis are shown in figure 5.16.

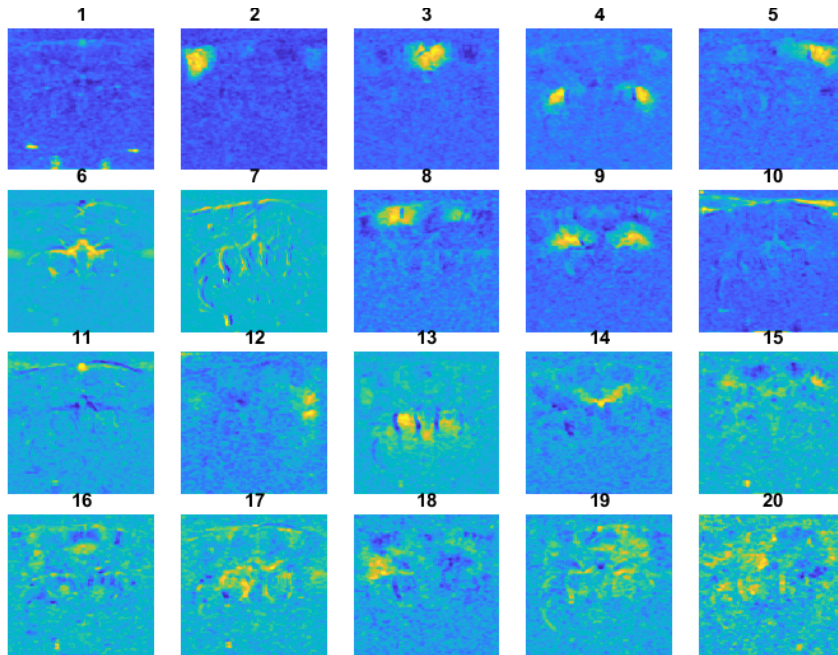


Figure 5.16: Group-ICA common spatial maps. The components that correspond to the interesting reference ones are denoted with numbers 2, 3, 4, 5, 8, 9, 13 above each map.

A comparison important to be conducted is between single- and group-ICA results. In other words, examining whether, and to what extent, the sources that were back-reconstructed from the group mixing matrix are similar to the sources yielded from a single-ICA analysis performed separately on each subject's dataset.

In figure 5.17, the spatial and temporal correlations for all components are depicted. Regarding the similarity of the spatial maps, we observed a high correlation value for the first 10 components as well as LAT, which more likely represent distinct anatomical and functional networks as visually checked. However, a wide variation is observed for the remaining 9 components. These components' values were both lower and more scattered for the 5 datasets, because their spatial maps were quite noisier.

On the other hand, the values of the temporal correlation for all the components significantly varied between datasets. It is obvious that several components' values

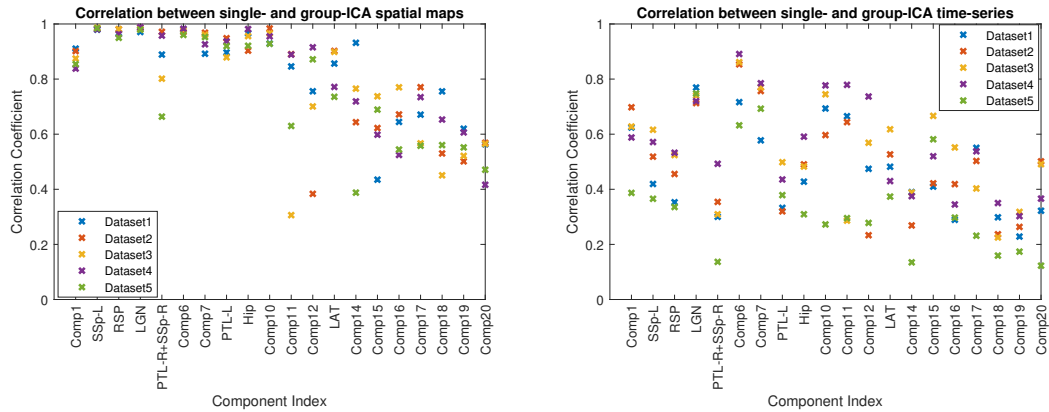


Figure 5.17: Correlation between single- and Group-ICA in the five datasets. Left: Correlation between the spatial maps. The first 10 components are found to be more consistent and correlated. Right: Correlation between the time-series. Only the LGN time-series are found similar to each other.

were found to be high (e.g. above 0.6) but not consistent for the whole dataset. Only the LGN component is found the most robust one, because its time-series are high and similar to each other, all ranging between 0.7 and 0.8. This means that many differences appeared in the produced time-series by single- and group-ICA.

Subsequently, the temporal sources were further investigated for their task relevance. Components' time-series were correlated with the stimulus pattern, as calculated for single-ICA analysis (figure 5.12) and are shown in figure 5.18.

Again the LGN component is highlighted as the most task-relevant one, having a correlation coefficient above 0.6. However, there must be a problem with the first dataset because the LGN time-series is not so highly correlated both in case of single- and Group-ICA. Furthermore, the values calculated in case of group-ICA subject-specific time-series (0.6 – 0.8) were higher than those obtained from single-ICA results, mostly ranging from 0.5 – 0.6 as shown in figure 5.12. This fact confirms that Group-ICA analysis yields more consistent results suitable for drawing conclusions about groups of subjects.

Besides, most of the values of the rest of the components vary a lot and are below 0.4. Nevertheless, apart from LGN, some values that are above 0.4 in some datasets appear in components 5, 7, 10 and 15. For these components, because high values are not found in all five datasets and also couldn't be justified anatomically, it is assumed that these regions are not really task-relevant ones. The high values are due to an increased number of activated pixels in the task-relevant LGN region, after being anatomically examined.

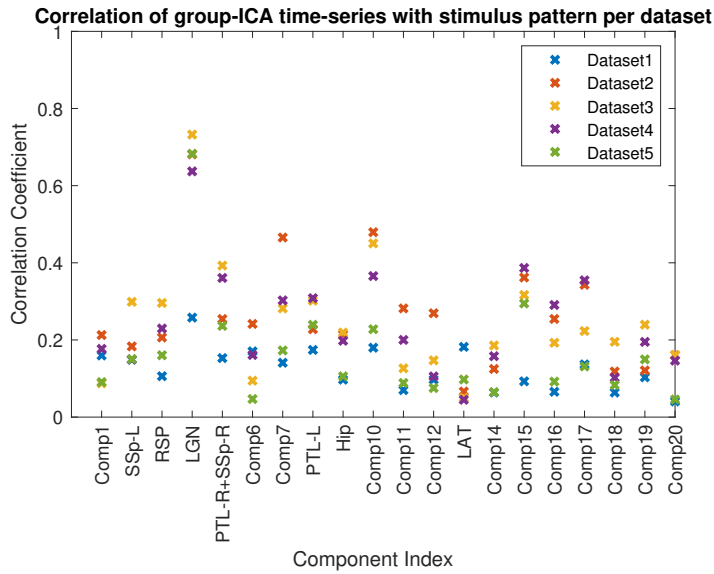


Figure 5.18: Correlation of the time-series with the stimulus pattern for all five datasets. LGN was observed as the highest correlated components.

5.1.2.2 Between-Experiments

Another experiment was also examined for Group-ICA in order to compare the results obtained in different conditions. The experiment was a single-screen visual-stimulation experiment with the same stimulation pattern as before. More specifically, only the right screen was displaying images, so the right visual pathway became stimulated in the mouse subjects. Again, five different datasets were obtained under these conditions. Being in the same way stimulated, it is interesting to check the differences occurring in the task-relevant spatial maps and time-series of both experiments.

After applying temporal Group-ICA, 20 common between-subjects spatial maps and separate mixing matrices were extracted. The produced spatial maps are shown in figure 5.19.

The majority of the most clear and compact components, for instance components 1 – 10, were again extracted similarly as in the other experiment. A big difference was observed in the previously most task-relevant component. In the two-side stimulation, bilateral areas were activated but in this case only one was. Therefore, again it is confirmed that LGN (component 7) was the most significant region, as it was the only one with apparent changes.

Regarding the subject-specific time-series, the differences in the activated components were checked as well. In figure 5.20, the correlation of each component's time-series with the stimulus pattern was depicted. As expected from the other experiment, the LGN area was most strongly correlated with the stimulus pattern.

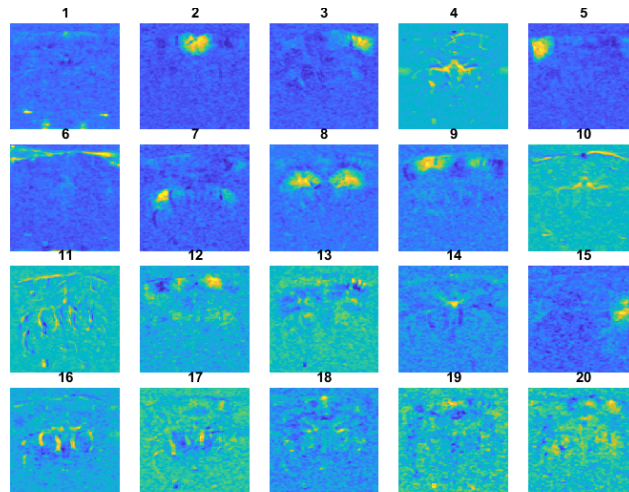


Figure 5.19: Group-ICA common spatial maps of the right-visual stimulation experiment. The components that correspond to the interesting reference ones are denoted with numbers 2, 3, 5, 7, 8, 9 17 above each map.

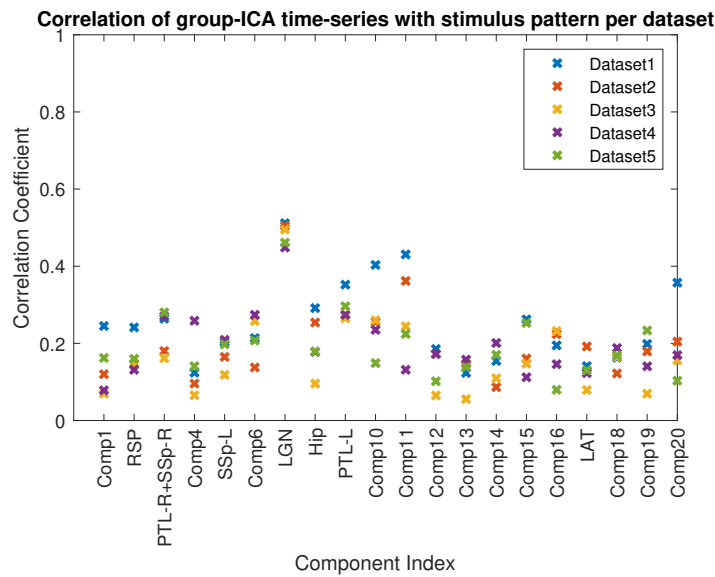


Figure 5.20: Correlation of the time-series with the stimulus pattern for all five datasets. Unilateral LGN was observed as the highest correlated.

However, the values were slightly decreased, ranging from 0.45 to 0.55 for the five datasets. That may have occurred because the other side of LGN was also shown in the same map, even with very low intensity values, so that the time-series of the whole component deviated from the stimulus time-series.

The correlation values of the other components varied and were quite low, most of them below 0.3. Some exceptions, where values exceeded 0.3, were apparent for some datasets in the case of components 8, 9, 10, 11 and 20. The reason behind this was some activated pixels in the LGN region.

5.1.2.3 Group Anatomical-Interpretation Comparison

To verify that the proposed group-ICA procedure is capable of extracting similar spatial patterns, the labels revealed from each component were examined. A similarity matrix was constructed to compare each one of the common components with the previously extracted 8 interesting labels. In figures 5.21 and 5.22, the similarity matrices of the two different experiments are shown.

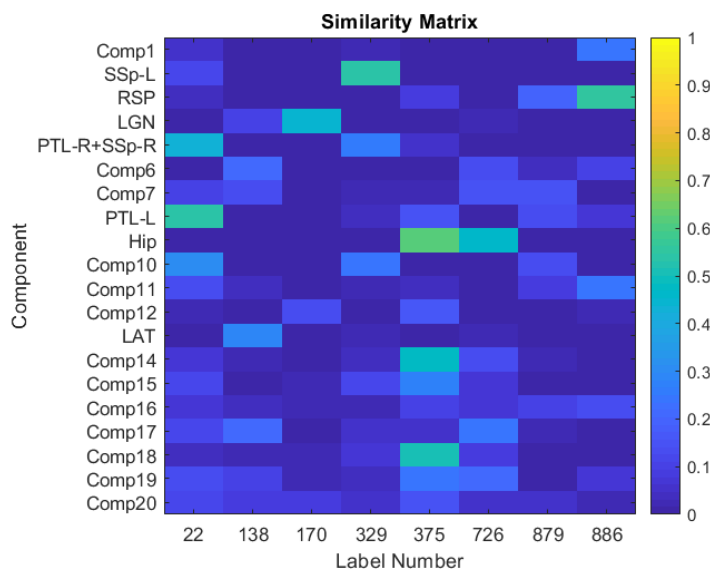


Figure 5.21: Similarity matrix between the components of the both-sides visual stimulation experiment and the atlas' labels maps. The numbering of the components is according to figure 5.16

This type of resulting matrices facilitates finding the most representative components of each region. For example, regarding the hippocampus region, with label 375, apart from the easily found component 9, also components 14 and 18 correspond to parts of that region. This can be directly observed from the similarity matrix, as these components have the highest values for label 375. Thus, when a specific brain area is captured by different components, it can be easily visualized.

Furthermore, comparing to single-ICA, the values found in the Group-ICA matrices were approximately of the same level. No extreme differences were noticed. As expected, only in the second experiment some differences were detected. The LGN component of the second experiment was less similar to the real LGN region

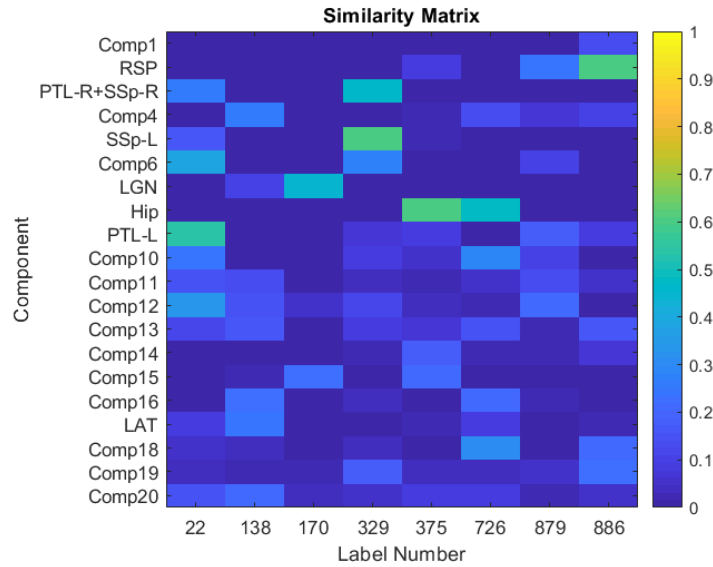


Figure 5.22: Similarity matrix between the components of the right-visual stimulation experiment and the atlas' labels maps. The numbering of the components is according to figure 5.19

because now bilateral regions were not activated and the LAT component was not very distinguishable in the set of components.

5.2 3D Resting-state Experiment

Next, the effects of a different condition were explored. fUS data were acquired from different brain positions, while not setting any specific task for the experimental mouse to execute.

More specifically, a fUS dataset was collected comprising images from 18 coronal slices. After excluding four initial slices that seemed not to be captured correctly, 14 slices remained of approximately 2000 images (PDIs) taken in each slice position, with a matrix size of 256×256 . The PDIs of each slice were fed to the ICA algorithm. The same ICA parameters have been set as before. Specifically for the number of ICs, the same procedure as in Section 4.4.4 was repeated, which involved trying different number of ICs in ICASSO in order to find the most stable and reproducible results. In the 3D resting-state case, a higher number of ICs was selected as optimal compared to the previous 2D visual-stimulation experiment. 20 ICs did not seem enough to clearly separate regions because more distinct anatomical regions were revealed now that more brain positions were examined. An example of the ICASSO results is given in the Appendix B. In figure 5.23, the 30 components of the first slice are shown.

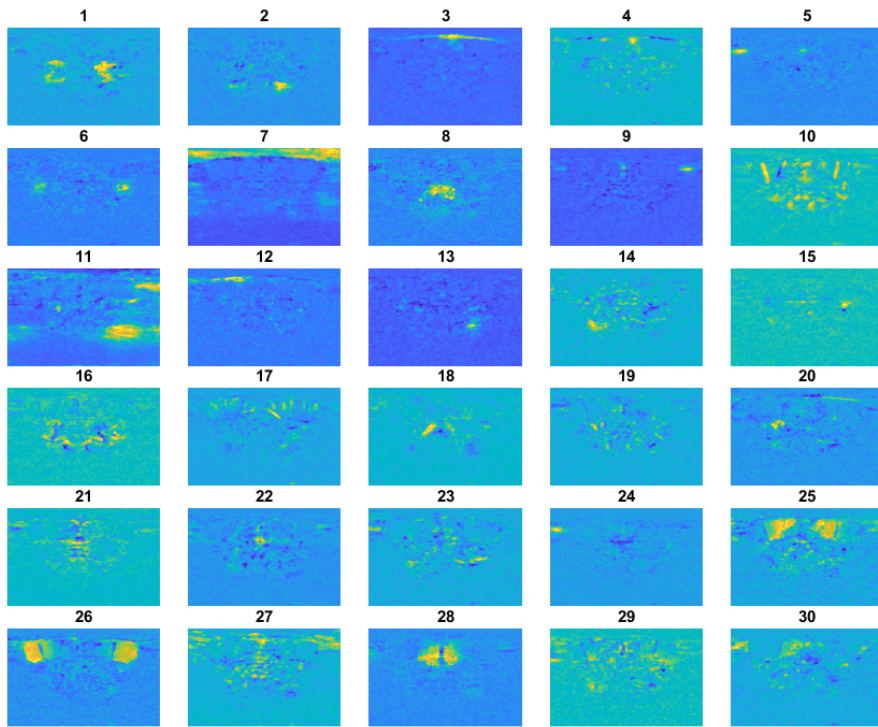


Figure 5.23: Resting-state spatial maps of the 1st slice

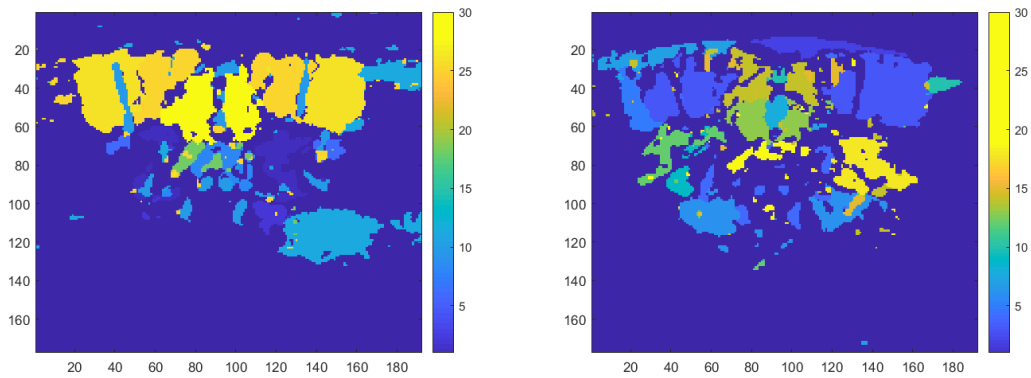


Figure 5.24: Brain structure of Slices 1 and 2 after gathering most interesting components. The color of each region matches the number of the component, ranging each time from 1 to 30.

The clearest and most compact components can be combined while trying to predict the brain structure of the specific slice, as it is demonstrated in figure 5.24 for slices 1 and 2. The main components of slice 1 and 2 appear after being thresholded to isolate the most activated area in each case.

Subsequently, the purpose was to investigate the spatial consistency of several functional and anatomical regions between adjacent slices. To achieve that the functional areas that clearly appeared in the ICA components produced from one reference slice compared to the corresponding areas found in the adjacent slices.

For example, for illustration purposes, the whole set of slices is depicted in two figures, 5.25 and 5.26, where the 4th and the 9th slice were used as a reference slice, respectively. In each figure, the reference slice, as well as 3 preceding and 3 trailing slices, were used for the comparison. The components in the reference slice were selected with regard to how distinctly distributed the maps of some ICA components appear and how much correlated they are with components from adjacent slices. If some components are highly correlated with components in adjacent slices, these become good candidates for further visual inspection.

When matching the corresponding components of different slices, we find that some of them are similar to multiple components of the reference slice. This occurs because ICA does not separate the regions in the same way every time. Therefore, some components represented separate parts of the same anatomical area or did not constitute a so clear region. Some clear examples of each slice are contoured by a grey box.

The components that have been separated in the same way can be found as having high correlation value. The fact that several very high values were found, confirmed the continuity of distinct brain regions in space. In the two figures, it is well noticeable how the regions in the highlighted boxes changed when looking in an adjacent brain slice.

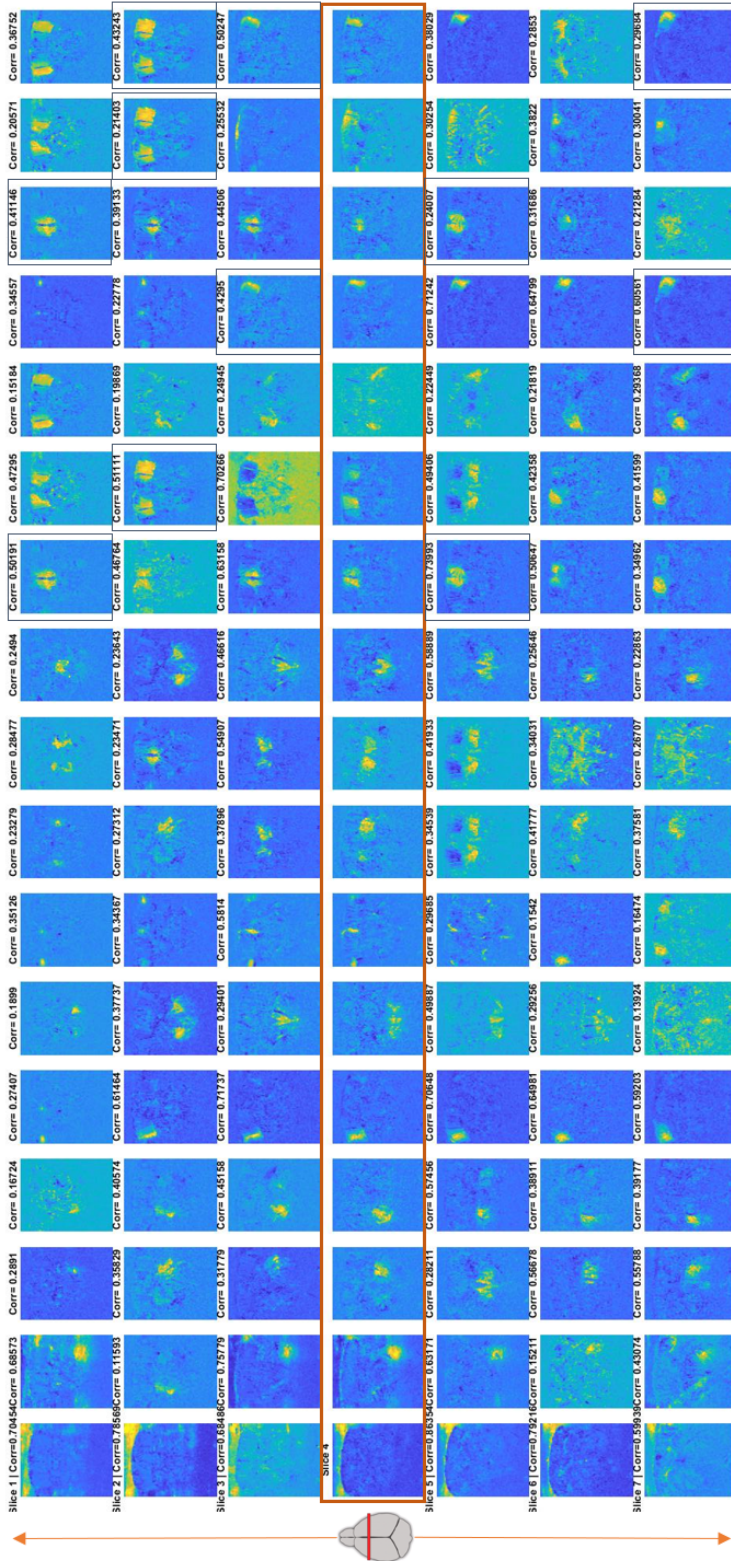


Figure 5.25: The reference slice is Slice 4 and it is located in the middle row (4th row) of the figure. The corresponding components of the reference components that belong to 3 slices before and after that are displayed as well as their correlation coefficient values.

This work is mainly focused on applying the data-driven ICA method to fUS data in order to get access to the different brain anatomical regions. The whole processing pipeline was designed, including all the necessary preprocessing steps, ICA approaches and parameters, as well as the post-processing PDIs-to-atlas registration. The performance of ICA and its results' effectiveness were finally assessed using both task-based and resting-state experiments.

This concluding chapter consists of three sections. In Section 6.1, the overview of this thesis is presented. Section 6.2 summarizes the contributions made in this work, while Section 6.3 provides some recommendations for future work regarding further fUS-data analysis methods.

6.1 Thesis Overview

By moving beyond the gold standard of functional-imaging techniques, that is fMRI, and the concept of conventional ultrasound-imaging acquisitions, ultrafast plane-wave compounding has given rise to a new promising modality, fUS. The combination of high spatiotemporal resolution and sensitivity, deep penetration and portability led to an increasing number of publications and scientific teams exploring fUS imaging as well as its potential applications in the field of Neuroscience. Nevertheless, due to the pioneering nature of this work, the majority of this thesis effort was focused on setup validation and experimental-parameter configuration (Table 3.1) and not so deeply on the data analysis. Thus, the analysis part needs further exploration since, so far, correlation analysis was mostly applied on fUS studies among the obtained signals or the signals and the stimulation pattern. In the current work, the exploration was based on ICA, a more advanced method for decomposing the different brain networks. Extensive fMRI research showed that the ICA method has been successfully used in numerous neurological task-based and resting-state applications. Combined with the fact that ICA makes no assumptions on data models, ICA has been the algorithm of choice for this analysis.

In Chapter 4, the whole analysis strategy proposed was described. The first stage was the determination of the appropriate pre-processing methods. A number of preprocessing steps was chosen, including removing points in space and time, gaussian smoothing, centering, whitening and data reduction, along with their parameters. Then, regarding ICA, the fast-ICA algorithm was used accompanied

by the ICASSO software package to improve the components estimation. A critical step for applying ICA is the optimization of the number of ICs. To address that problem, the question was split into two parts, first defining the effective data-dimension reduction and then the number of ICs in order for the results to be stable as well as reproducible. That was achieved by comparing the effects of different ICs values using the ICASSO software separately for every experiment. That procedure was firstly tested on the 5 datasets acquired from a visual-stimulation experiment. After assessing the quantitative measures of IC stability of the whole set of components, as well as separately for the ones selected as the most clear ones, a range of values from 15 to 30 components was found appropriate. The number of 20 was eventually kept for the rest of these experiments' analysis. Of course, the computation time significantly increased with the number of ICs when running a 100-time ICASSO.

In Chapter 5, the methodology developed previously in Chapter 4 was applied, and the results produced by single- and group-ICA were presented. Firstly, ICA was applied separately to each dataset and the produced results were examined in both the space and time domain. Regarding space, the components' anatomical regions were identified. After the acquired functional images had been aligned with the label-annotated brain atlas, each activated region of the components' spatial maps was matched with the atlas' labels. To isolate only the most significant labels, two filtering strategies were used, (i) the overlap between PDI and atlas' region and (ii) mean intensity. Then, all the labels found were kept and characterized as relevant to the specific component. According to that procedure, 8 interesting labels resulted from all the interesting components segmentation. The brain regions found included the LGN, hippocampus, primary somatosensory areas, retrosplenial areas and parietal association areas.

Regarding the time domain, components derived from single-ICA were examined for their task relevance. The components' time-series were cross-correlated with the given stimulation pattern. Based on the produced correlation coefficients, a type of components ranking was proposed. The signal of the component representing the LGN region was found as the highest correlated in all five datasets, reaching a correlation of a value equal to 0.6. Thus, the most task-relevant component was always the LGN component. The finding of LGN was confirmed by the visual-pathway, where this region is a very significant one during visual processing. However, not the same ordering pattern was derived for the rest of the components as they are not directly associated with the visual-pathway.

Afterwards, the same 5 datasets were examined in a group approach. Using group-ICA, the components were produced in the same order across datasets solving the components correspondence problem and facilitating the comparisons. The differences detected between single- and group-ICA regarding the spatial maps were not significant. Both approaches were capable of discovering the interesting maps, which similarly corresponded to the true labels. Whereas, regarding the

temporal components, in group-ICA the LGN's time-series were correlated with the stimulation pattern in a higher level, ranging from 0.6 – 0.8. Then, the group results in a slightly different condition of the same experiment were evaluated. The most task-relevant LGN component was again identified.

Finally, ICA performance was tested on a single 3D dataset obtained from a resting-state experiment. Then, ICA was performed on the PDIs of each coronal slice resulting in different anatomical and functional networks. The most compact and interesting components were investigated for their spatial consistency. After having selected a reference slice, the corresponding components of the adjacent slices were found. In most cases, the correlation values were high, having an average value around 0.41 and confirming the regions' spatial continuity.

6.2 Scientific Contributions

- An extensive fUS-related literature review was presented, categorizing the various research works that has be done regarding the fUS-setup parameters, experiments and performance (table 3.1)
- Data-analysis methods used in fMRI were explored while checking which could be potentially applied to fUS data in the future. A summary table describing the widely-used fMRI methods was given in table 3.2.
- The whole ICA processing pipeline was established. The appropriate pre-processing steps as well as the free parameters of the ICA algorithm were determined. ICA ambiguities regarding the parameters, such as the number of PCA components and ICs, were examined in great detail after performing a (limited) parameter-space exploration with ICASSO. The ICASSO software package was used to facilitate that procedure, running ICA multiple times. For the determination of the optimal parameters, the same ICASSO procedure should be followed in every experiment separately.
- The ICA performance was tested on 2D datasets of visual-stimulation experiments as well as 3D resting-state experiments.
- The extracted results were assessed both in time and space. Regarding time, the temporal components were correlated with the stimulus pattern. In parallel, regarding space, the spatial maps were validated for the anatomical regions that they represent. Thus, task-relevant brain regions were discovered.
- Both single- and group-ICA approaches were capable of revealing the seven most commonly observed regions without any a priori information.
- ICA results successfully revealed the brain functional segregation into anatomically meaningful regions in the thalamus, such as the LGN and LAT,

the hippocampus and in cortex the parietal, somatosensory and retrosplenial areas.

- The LGN was identified as the most task-relevant component by both approaches, as also proven by the visual-pathway.
- In the case of the resting state experiment, the ICA-derived regions' continuity in space was confirmed.

6.3 Future Directions

Several major limitations within this study are identified. First and foremost, there is the fact that the main analysis was performed on 2D datasets. As 3D fUS imaging (or 4D) is a rapidly evolving field, the proposed methodology should be translated to 3D, as well. In section 5.2, ICA was successfully applied to a 3D resting-state dataset. However, for a better evaluation, a 3D atlas registration is a necessary next step. PDIs from multiple brain slices, forming a 3D fUS vascular atlas, should be aligned with corresponding slices in the annotated brain atlas. This can be achieved by using several landmarks for the observed blood flow that match the shape of brain structures and a proper geometrical transformation. Thus in every new experiment, the 3D fUS atlas will facilitate locating in real time the position of the image plane scanned. More specifically, the brain regions with significant neural activity would be also directly recognized.

Furthermore, for better evaluating the interpretability of the ICA results related to the brain responses, more experiments must take place. Firstly regarding the visual-stimulation one, it is important to examine slices containing all the areas in the visual-pathway, such as primary visual areas and the Superior Colliculus.

Secondly, experiments incorporating data acquired simultaneously from different modalities should take place. For instance, fUS measurements in combination with simultaneous EEG recordings can be investigated in case of epilepsy disorder to validate the activations found. As already tested, the combination of EEG and fMRI has been used extensively to map the hemodynamic changes associated with interictal and ictal epileptic discharges [84].

Regarding the data-analysis method used, some other promising options are also proposed as future work. Some additional steps to ICA as well as other methods for drawing more and stronger conclusions are the following:

- Discover patterns of dynamic functional connectivity

Although the majority of fMRI studies, so far, is based on the fact that the statistical inter-dependence of signals between distinct brain regions is constant throughout a recording, it has been observed that network patterns may undergo substantial fluctuations over time, leading to a paradigm shift from static- to dynamic-analysis methods. In many studies, such as [85], [86],

ICA constitutes a good way for identifying changing patterns of synchrony at a multivariate level, in combination with strategies, such as the well-applied sliding-window approach and time-frequency analysis that are able to detect the dynamic changes and variability over time in inter-region activity (dynamic functional network connectivity - FNC). Therefore in fUS-signals, a dynamic manner should be also examined.

- Incorporate prior information: semi-blind ICA

In some task-based experiments, it would be useful to incorporate additional information into the ICA analysis. As implemented in the semi-blind ICA algorithm on fMRI data [87], information regarding the paradigm pattern could be used to constrain the extracted time-series so to resemble the pre-defined pattern. That way, ICA sets some assumptions upon the extracted hemodynamic response, but not so explicit as in case of GLM.

- Discriminate different types of signal patterns using MVPA (Multi-Voxel Pattern Analysis)

More advanced analysis methods should also be applied to fUS data for further brain-activity interpretation. As already mentioned in Section 3.3, MVPA is a well-known pattern-classification algorithm, used in fMRI to decode the information that is represented in distributed (multi-voxel) data responses. For example, in a visual-stimulation experiment, as the ones conducted in the current work, MVPA could be possibly used to discriminate the type of stimuli. In case of presenting faces and objects or scenes images as visual stimuli, the different neural-activation patterns could be detected. Then, the different brain responses in each region could be distinguished based on the category of a viewed object. In [88], other examples reported where MVPA has been used on human datasets are the (visual) decoding of the orientation of a striped pattern or the movement direction of a field of dots, or even whether the stimuli is a picture or a sentence, and in particular the semantic category of that. Some other studies achieved to examine the subject's cognitive state.

A.1 Gaussian Smoothing

To draw some conclusions regarding the different values of the kernel size and sigma, I checked the collected ICA components in each case for whether all the significant brain regions are appearing and are clearly distinguished.

To verify that a smoothing procedure is a necessary step for our single-subject dataset analysis, I firstly displayed the 20 ICA components without smoothing, shown in figure A.1. In that case, the region of LGN (Lateral Geniculate Nuclei) is not clearly apparent and significantly activated. Despite the original high spatial resolution, that is equal to $1540/(30 \cdot 10^6) = 50 \mu m$ when using a $30 MHz$ probe, spatial smoothing (and a resulting decrease in resolution) seemed necessary.

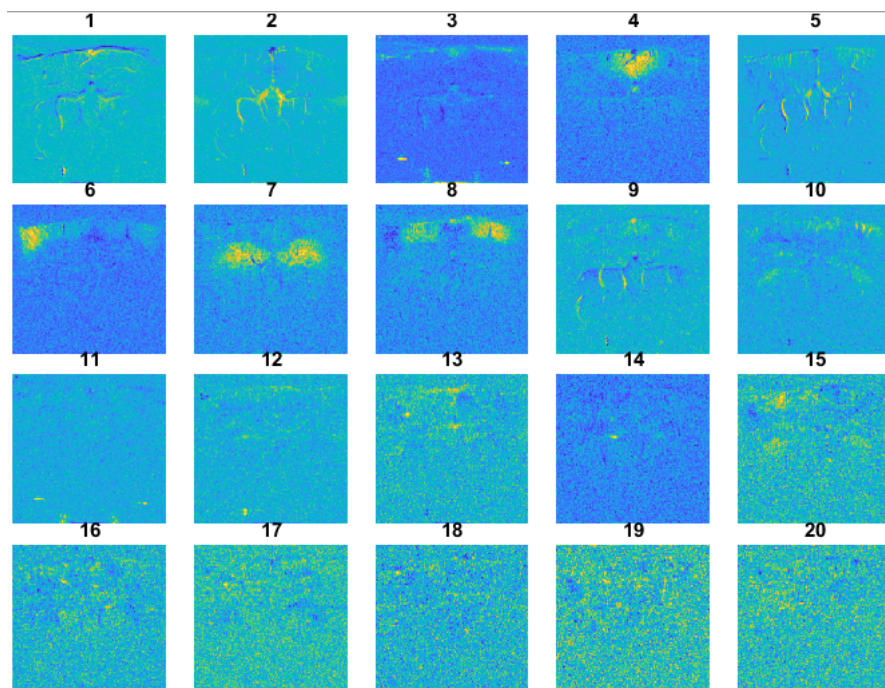


Figure A.1: ICA components without smoothing

To understand the influence of spatial smoothing on the ICA components, different kernel sizes and σ values were tested. In figure A.2, the ICA components

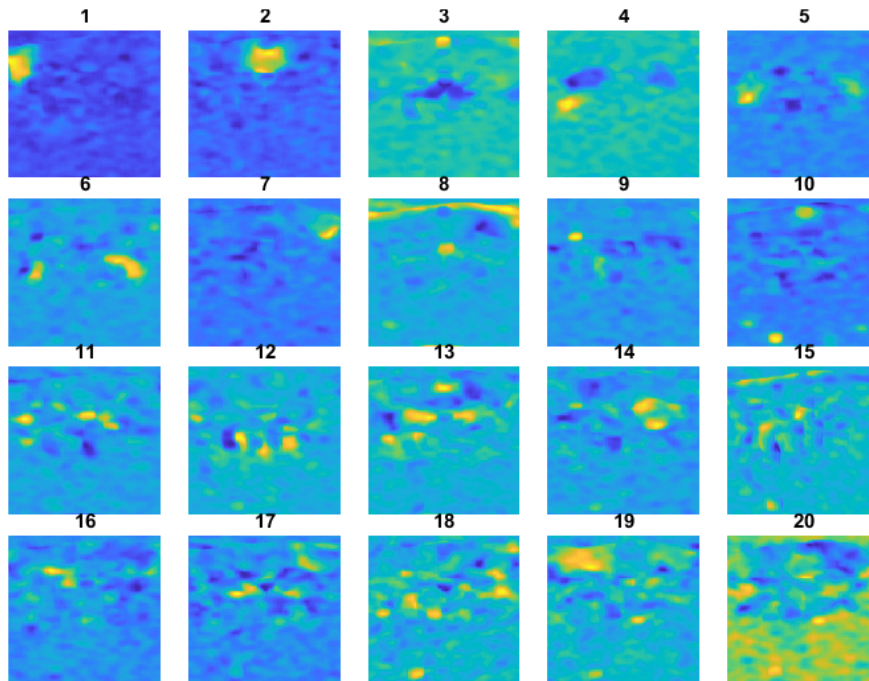


Figure A.2: ICA components after being smoothed with a large Gaussian kernel

are shown in case of having applied a Gaussian kernel of size $10 \times 10 \times 10$ and $\sigma = 3$.

All the interesting components (described in Section 4.4.4) appear, making the kernel values appropriate. Also, the correlation coefficient of the LGN component time-series with the stimulus pattern reaches the value of approximately 0.55, which is close to the highest discovered. Using different but neighboring values to for the Gaussian kernel showed similar outcomes. Thus, without loss of generality, these parameters are chosen for the preprocessing smoothing step.

As it was expected, when the size of the kernel increases, the components appear more blurred and some of them are not clearly distinguished. Thus, a large-size kernel did not seem to be an appropriate choice.

A.2 Infomax Algorithm

As mentioned in the main document, FastICA and Infomax are the most commonly algorithms used and give the best overall performance when being applied to fMRI data. So, Infomax was also tested for fUS data.

Infomax maximizes the information transfer from the input to the output of a network using a non-linear function [67]. However, an important drawback of that method is that it tends to be biased towards a certain type of probability density functions (PDFs) for the extracted sources. That means it can find only

super-Gaussian or sub-Gaussian sources. Most applications of ICA to fMRI cases use Infomax since the sources of interest are mostly super-Gaussian (i.e., PDFs that are heavier-tailed and peakier than the Gaussian) and that algorithm favours that kind of separation.

An example of the extracted ICA components is depicted in figure A.3. In general, we see similar components with Fast-ICA. All the most-common “interesting” components light up again when using the Infomax algorithm. Correlation of the task-relevant LGN time-series with the stimulation pattern = 0.5760.

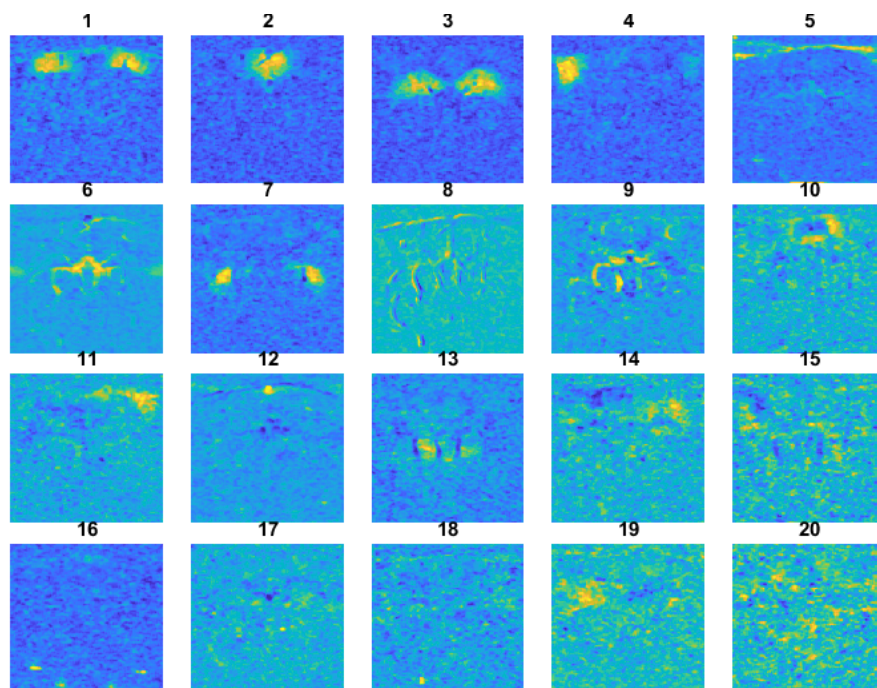


Figure A.3: ICA components using the Infomax algorithm

A.3 Fast-ICA Methodology

The ICA method can give a solution by minimizing or maximizing certain contrast functions. This transforms the ICA problem to a numerical-optimization problem. So, the Fast-ICA algorithms [89] for maximizing the contrast function in case of both deflation-based and symmetrical-based multiple-unit (multiple components) estimation are:

Algorithm 1 Multiple-unit Deflation-based Estimation

Result: $\mathbf{W} \leftarrow [\mathbf{w}_1, \dots, \mathbf{w}_C]$ **Result:** $\mathbf{S} \leftarrow \mathbf{W}^T \mathbf{X}$ **for** p *in* 1 *to* C **do** \mathbf{w}_p initialization **while** \mathbf{w}_p *changes* **do**

$$\mathbf{w}_p \leftarrow \frac{1}{M} \mathbf{X} g(\mathbf{w}_p^T \mathbf{X})^T - \frac{1}{M} g'(\mathbf{w}_p^T \mathbf{X}) \mathbf{1} \mathbf{w}_p$$

$$\mathbf{w}_p \leftarrow \mathbf{w}_p - \sum_{j=1}^{p-1} (\mathbf{w}_p^T \mathbf{w}_j) \mathbf{w}_j$$

$$\mathbf{w}_p \leftarrow \frac{\mathbf{w}_p}{\|\mathbf{w}_p\|}$$

end**end**

Algorithm 2 Multiple-unit Symmetrical Estimation

Result: $\mathbf{W} \leftarrow [\mathbf{w}_1, \dots, \mathbf{w}_C]$ **Result:** $\mathbf{S} \leftarrow \mathbf{W}^T \mathbf{X}$ $\mathbf{W} \leftarrow$ Random vector of length C **while** \mathbf{W} *changes* **do**

$$\mathbf{W}^+ \leftarrow \frac{1}{M} \mathbf{X} g(\mathbf{W}^T \mathbf{X})^T - \frac{1}{M} g'(\mathbf{W}^T \mathbf{X}) \mathbf{1} \mathbf{W}$$

$$\mathbf{W} \leftarrow (\mathbf{W}^+ \mathbf{W}^{+T})^{-1/2} \mathbf{W}^+$$

end

A.4 Components Reliability

The extracted components after searching for a different number of components (10, 15, 30, 50, 100) are shown in figures A.4 - A.7, respectively.

A.5 Components Reproducibility

The extracted components of all the five datasets are presented in figures A.9 - A.13. The spatial maps as well as the Iq values are shown in each case.

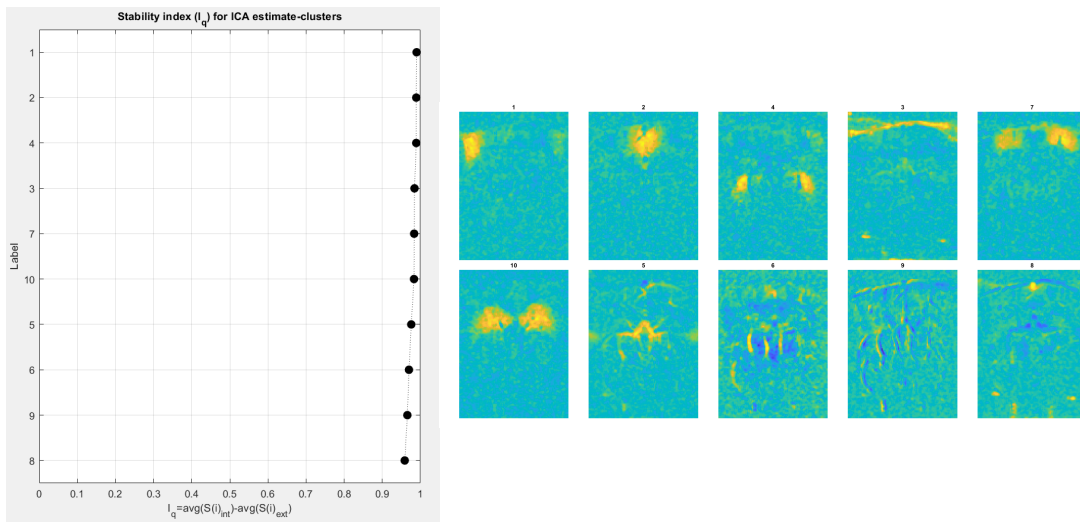


Figure A.4: ICASSO-10. Left: I_q values of each of the produced ICA components.
Right: The corresponding spatial maps.

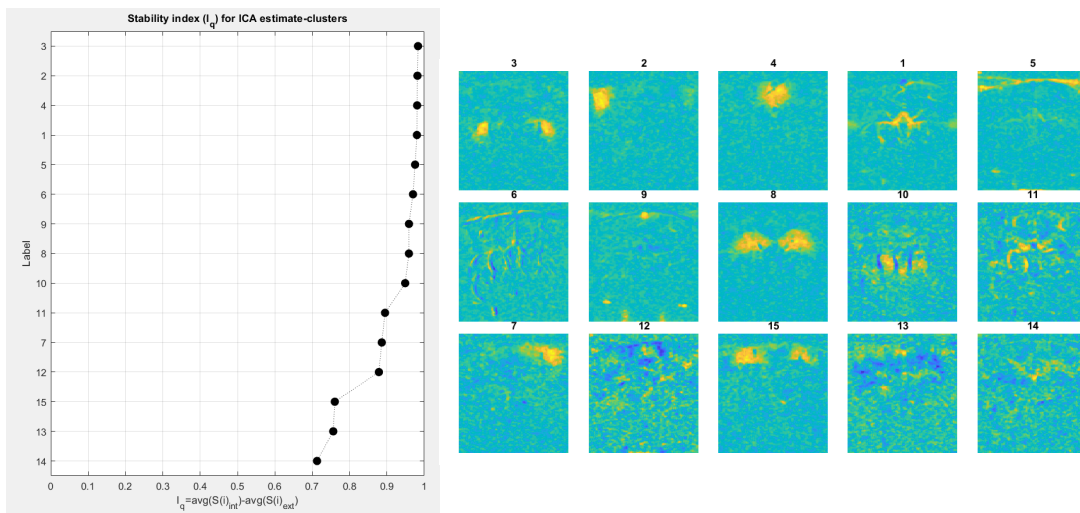


Figure A.5: ICASSO-15. Left: I_q values of each of the produced ICA components.
Right: The corresponding spatial maps.

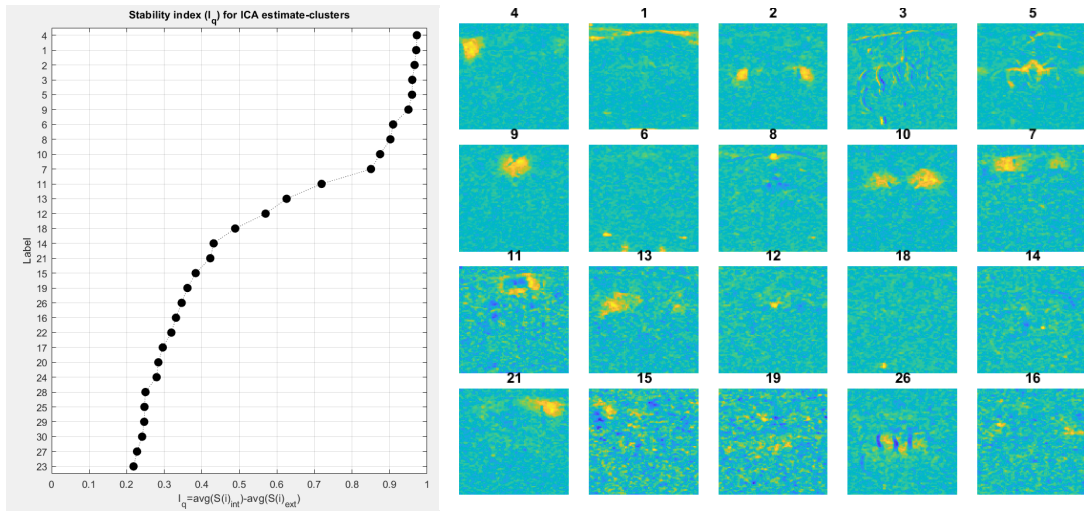


Figure A.6: ICASSO-30. Left: I_q values of each of the produced ICA components. Right: The corresponding spatial maps. From the number of 30 ICs, the I_q values start forming an L-curve.

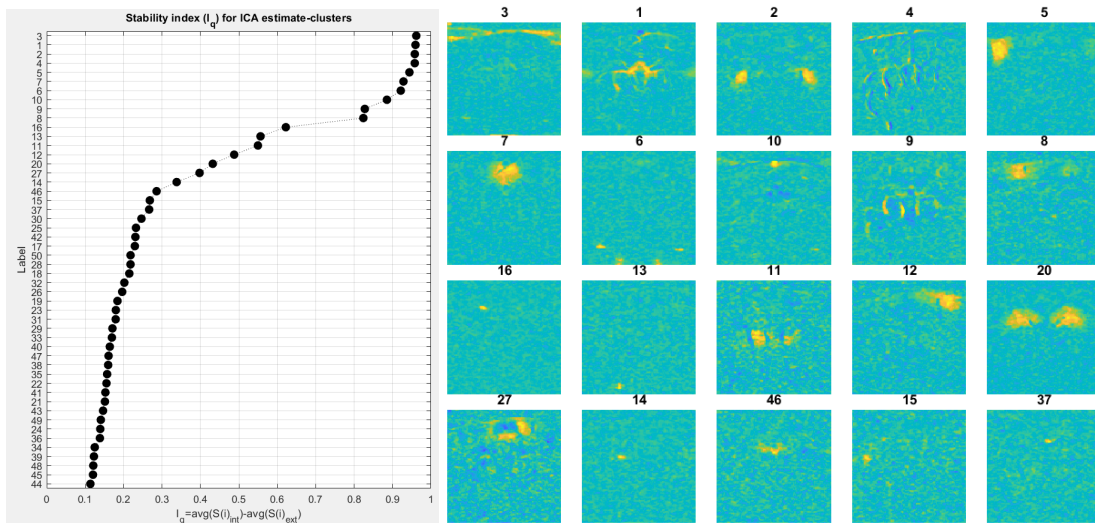


Figure A.7: ICASSO-50. Left: I_q values of each of the produced ICA components. Right: The corresponding spatial maps.

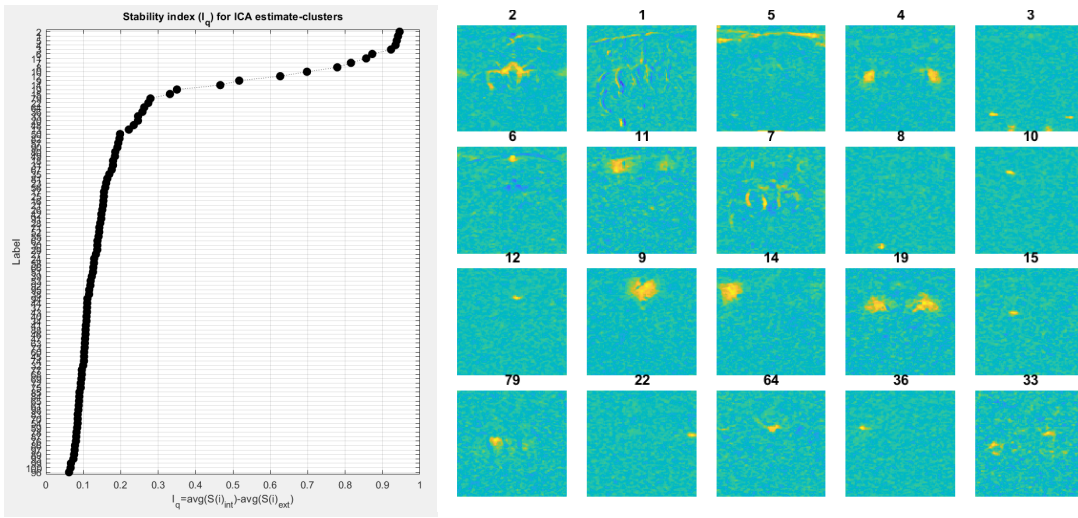


Figure A.8: ICASSO-100. Left: I_q values of each of the produced ICA components. Right: The corresponding spatial maps.

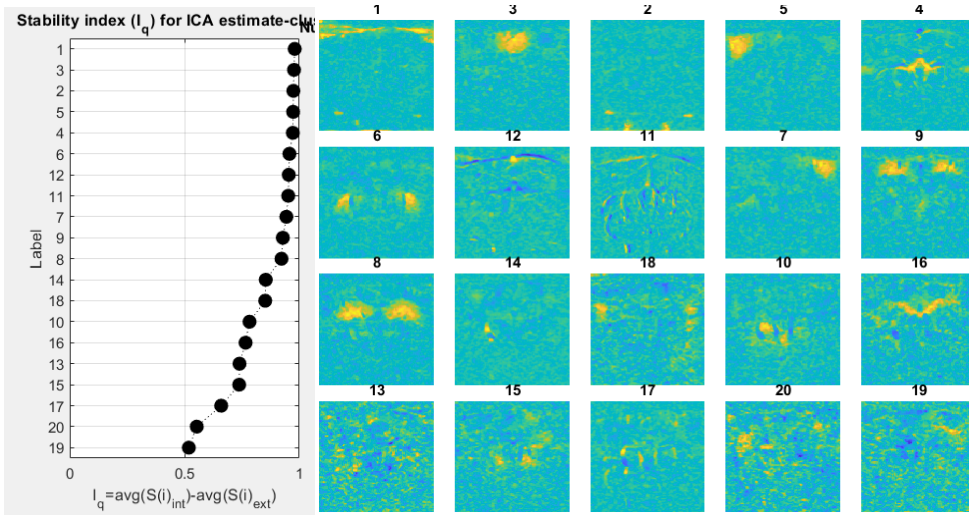


Figure A.9: Dataset-1. Left: I_q values of each of the produced ICA components. Right: The corresponding spatial maps.

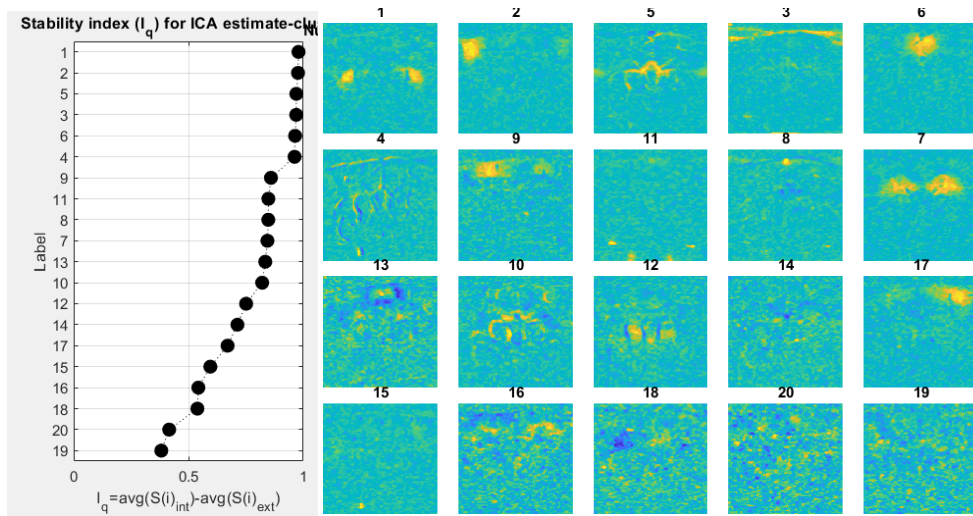


Figure A.10: Dataset-2. Left: I_q values of each of the produced ICA components. Right: The corresponding spatial maps.

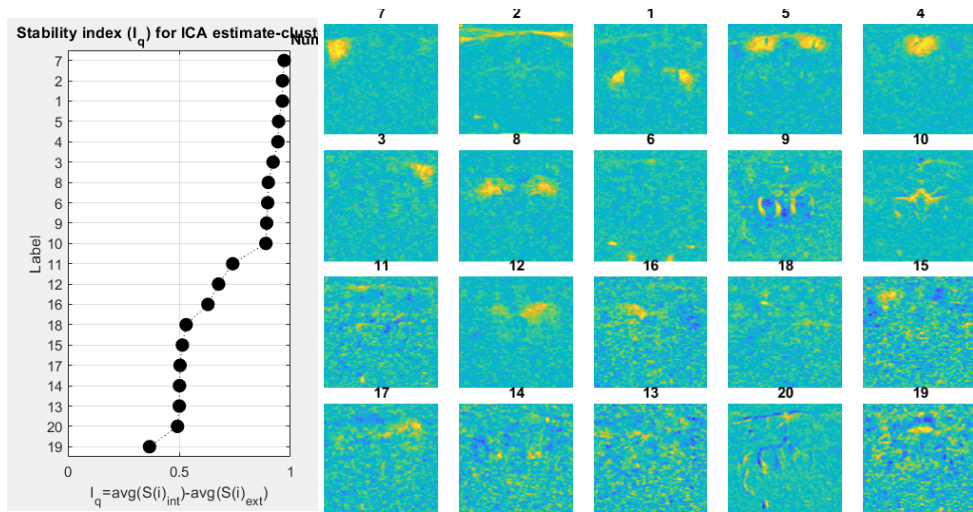


Figure A.11: Dataset-3. Left: I_q values of each of the produced ICA components. Right: The corresponding spatial maps.

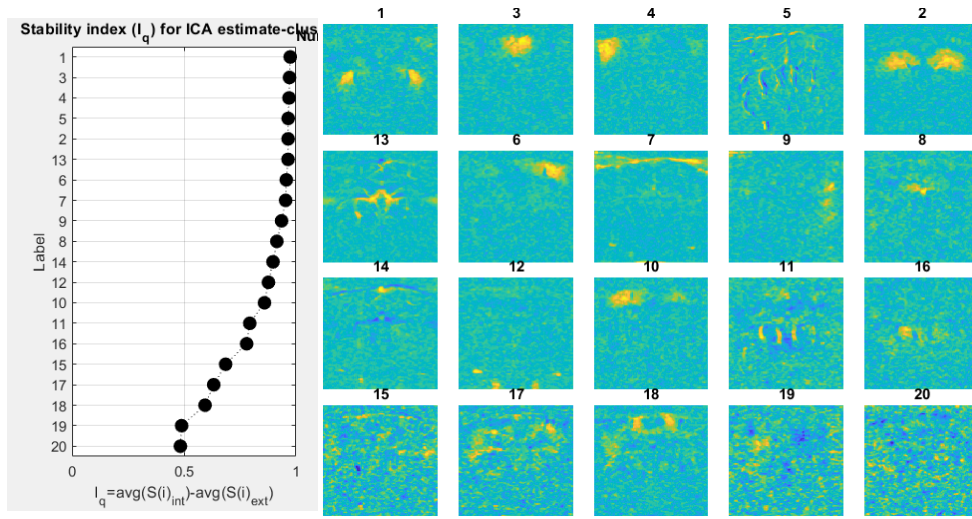


Figure A.12: Dataset-4. Left: I_q values of each of the produced ICA components. Right: The corresponding spatial maps.

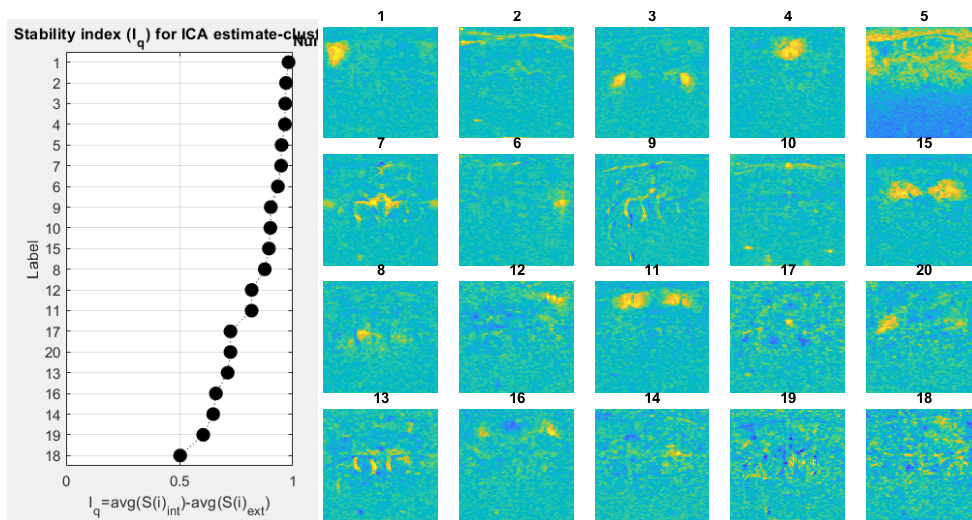


Figure A.13: Dataset-5. Left: I_q values of each of the produced ICA components. Right: The corresponding spatial maps.

B.1 Correlation of components' time-series with the stimulus pattern

As mentioned before, because of the single-ICA inherent variability in the time-series, the corresponding components for all the 20 produced by single-ICA could not be found. So, only the interesting components' correlation was displayed with the stimulus pattern. In order to also demonstrate the other components' task relevance, we can show the correlation values for each dataset separately. In figure B.1, we see the absolute correlation values between the time-series produced in case of the reference dataset with the stimulus pattern.

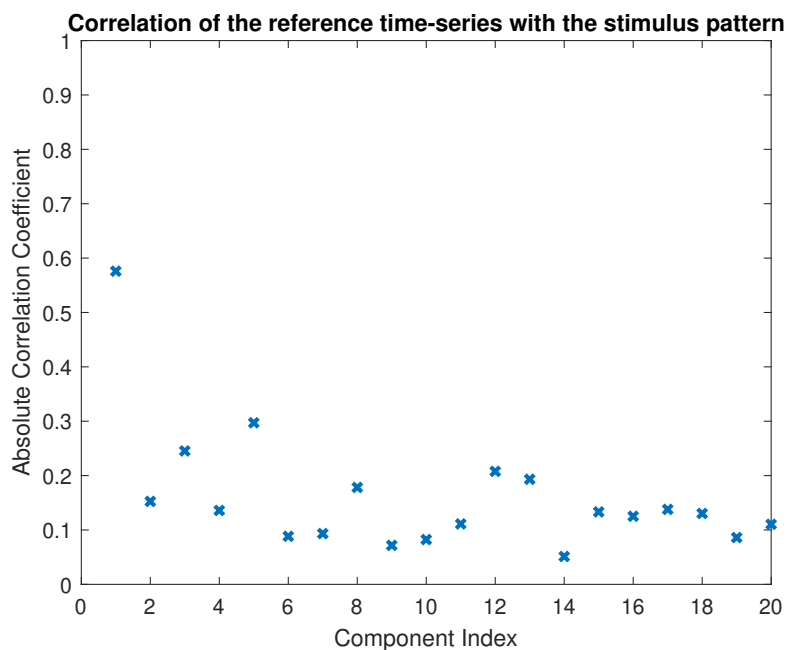


Figure B.1: Correlation of the reference dataset's time-series with the stimulus pattern.

B.2 Group-ICA

The 20 back-reconstructed, subject-specific spatial maps derived from group-ICA on the 5 datasets are shown in figures B.2 and B.3.

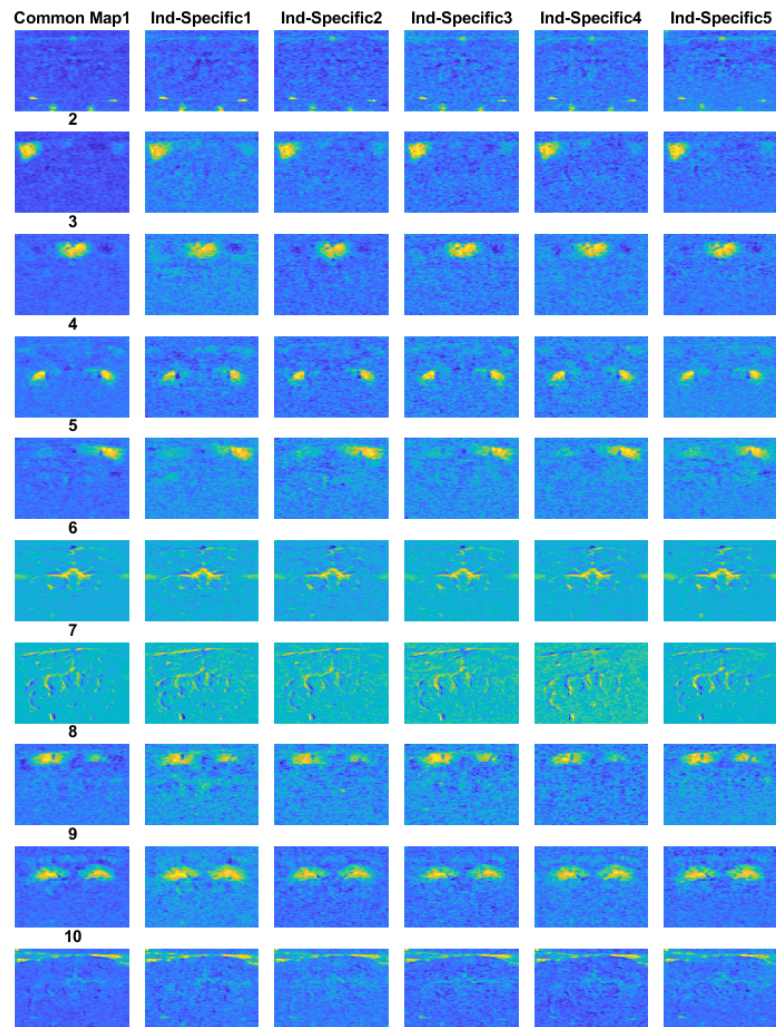


Figure B.2: Group-ICA common spatial maps and the back-reconstructed individual-specific ones (Maps 1-10)

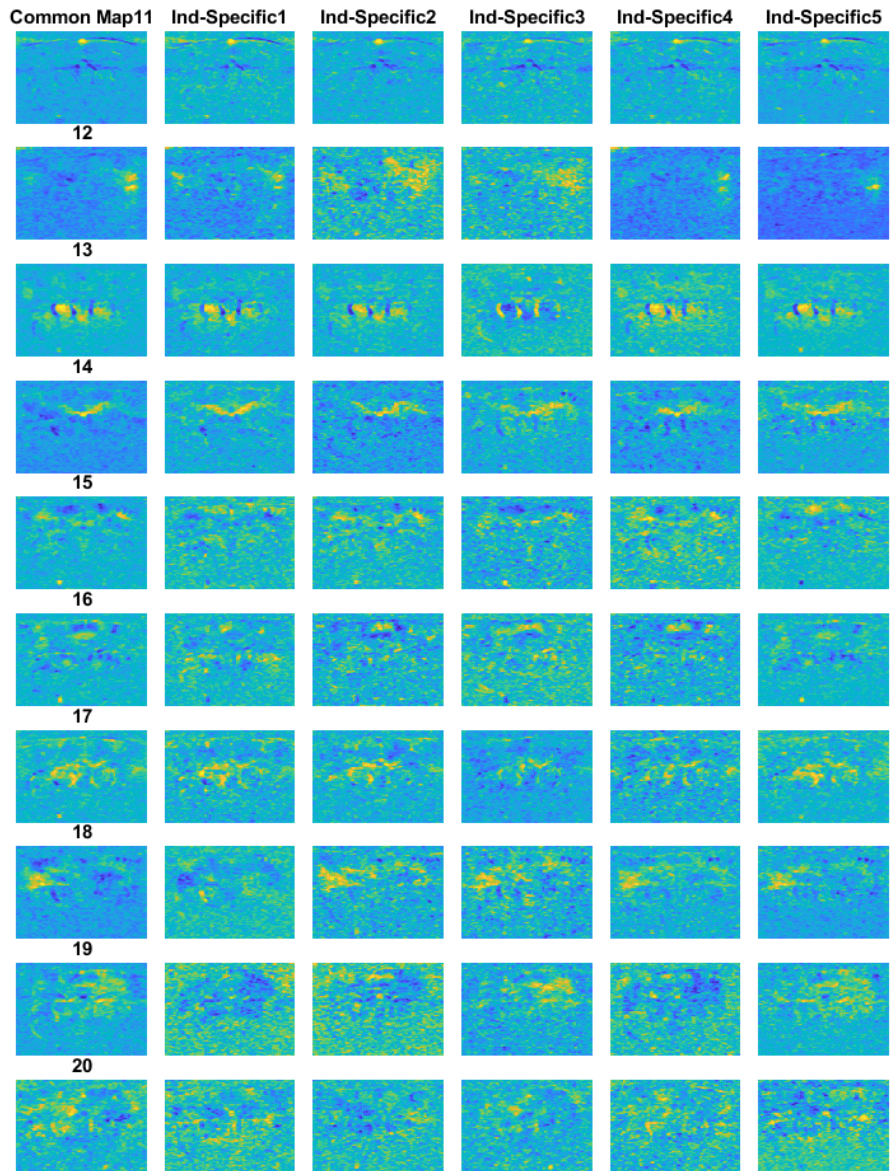


Figure B.3: Group-ICA common spatial maps and the back-reconstructed individual-specific ones (Maps 11-20)

B.4 Resting-state Experiment

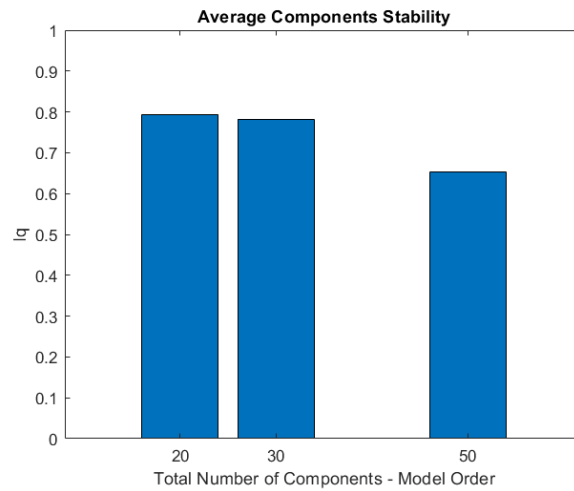


Figure B.5: Average Iq values for different number of ICs (20, 30 and 50) in case of resting-state dataset. Searching for 30 ICs was considered as the most appropriate choice.

It is observed in figure B.5 that there is no significant difference in the average Iq values, in case of 20 and 30 ICs, whereas it quite drops in case of 50 ICs. Thus, the selection of 30 ICs for the analysis led to a better separation. Even though the components were more, their Iq values were also higher.

Bibliography

- [1] Emilie Mace, Gabriel Montaldo, Bruno-Felix Osmanski, Ivan Cohen, Mathias Fink, and Mickael Tanter. Functional ultrasound imaging of the brain: theory and basic principles. *IEEE transactions on ultrasonics, ferroelectrics, and frequency control*, 60(3):492–506, 2013.
- [2] Emilie Macé, Gabriel Montaldo, Ivan Cohen, Michel Baulac, Mathias Fink, and Mickael Tanter. Functional ultrasound imaging of the brain. *Nature methods*, 8(8):662, 2011.
- [3] Jeremy Bercoff, Gabriel Montaldo, Thanasis Loupas, David Savery, Fabien Mézière, Mathias Fink, and Mickael Tanter. Ultrafast compound doppler imaging: Providing full blood flow characterization. *IEEE transactions on ultrasonics, ferroelectrics, and frequency control*, 58(1):134–147, 2011.
- [4] Charlie Demené, Elodie Tiran, Lim-Anna Sieu, Antoine Bergel, Jean Luc Gennisson, Mathieu Pernot, Thomas Deffieux, Ivan Cohen, and Mickael Tanter. 4d microvascular imaging based on ultrafast doppler tomography. *Neuroimage*, 127:472–483, 2016.
- [5] Thomas Deffieux, Charlie Demene, Mathieu Pernot, and Mickael Tanter. Functional ultrasound neuroimaging: a review of the preclinical and clinical state of the art. *Current opinion in neurobiology*, 50:128–135, 2018.
- [6] Ingeborg Stalmans, Selim Orgül, and Leopold Schmetterer. *Color Doppler Imaging*, pages 147–158. Springer Berlin Heidelberg, Berlin, Heidelberg, 2012. ISBN 978-3-540-69469-4. doi: 10.1007/978-3-540-69469-4_8. URL https://doi.org/10.1007/978-3-540-69469-4_8.
- [7] Charlie Demené, Thomas Deffieux, Mathieu Pernot, Bruno-Félix Osmanski, Valérie Biran, Jean-Luc Gennisson, Lim-Anna Sieu, Antoine Bergel, Stephanie Franqui, Jean-Michel Correas, et al. Spatiotemporal clutter filtering of ultrafast ultrasound data highly increases doppler and ultrasound sensitivity. *IEEE transactions on medical imaging*, 34(11):2271–2285, 2015.
- [8] Yi He, Maosen Wang, Xuming Chen, Rolf Pohmann, Jonathan R Polimeni, Klaus Scheffler, Bruce R Rosen, David Kleinfeld, and Xin Yu. Ultra-slow single-vessel bold and cbv-based fmri spatiotemporal dynamics and their correlation with neuronal intracellular calcium signals. *Neuron*, 97(4):925–939, 2018.
- [9] Yoshiyuki Hirano, Bojana Stefanovic, and Afonso C Silva. Spatiotemporal evolution of the functional magnetic resonance imaging response to ultrashort stimuli. *Journal of Neuroscience*, 31(4):1440–1447, 2011.

- [10] Philip G Haydon and Giorgio Carmignoto. Astrocyte control of synaptic transmission and neurovascular coupling. *Physiological reviews*, 86(3):1009–1031, 2006.
- [11] Sang-Pil Lee, Timothy Q Duong, Guang Yang, Costantino Iadecola, and Seong-Gi Kim. Relative changes of cerebral arterial and venous blood volumes during increased cerebral blood flow: implications for bold fmri. *Magnetic Resonance in Medicine: An Official Journal of the International Society for Magnetic Resonance in Medicine*, 45(5):791–800, 2001.
- [12] Vince D Calhoun, Jingyu Liu, and Tülay Adalı. A review of group ica for fmri data and ica for joint inference of imaging, genetic, and erp data. *Neuroimage*, 45(1):S163–S172, 2009.
- [13] Martin J McKeown, Lars Kai Hansen, and Terrence J Sejnowsk. Independent component analysis of functional mri: what is signal and what is noise? *Current opinion in neurobiology*, 13(5):620–629, 2003.
- [14] Jarkko Ylipaavalniemi. Variability of independent components in functional magnetic resonance imaging. *MSc, Department of Computer Science and Engineering, Helsinki University of Technology, Espoo, Finland*, 2005.
- [15] Stephen M Smith, Karla L Miller, Steen Moeller, Junqian Xu, Edward J Auerbach, Mark W Woolrich, Christian F Beckmann, Mark Jenkinson, Jesper Andersson, Matthew F Glasser, et al. Temporally-independent functional modes of spontaneous brain activity. *Proceedings of the National Academy of Sciences*, 109(8):3131–3136, 2012.
- [16] Aapo Hyvärinen and Erkki Oja. Independent component analysis: algorithms and applications. *Neural networks*, 13(4-5):411–430, 2000.
- [17] Jean-François Cardoso and Antoine Souloumiac. Blind beamforming for non-gaussian signals. In *IEE proceedings F (radar and signal processing)*, volume 140, pages 362–370. IET, 1993.
- [18] Anthony J Bell and Terrence J Sejnowski. An information-maximization approach to blind separation and blind deconvolution. *Neural computation*, 7(6):1129–1159, 1995.
- [19] Yi-Ou Li, Tülay Adalı, and Vince D Calhoun. Estimating the number of independent components for functional magnetic resonance imaging data. *Human brain mapping*, 28(11):1251–1266, 2007.
- [20] Hirotogu Akaike. Information theory and an extension of the maximum likelihood principle. In *Selected papers of hirotogu akaike*, pages 199–213. Springer, 1998.

- [21] Jorma Rissanen. Modeling by shortest data description. *Automatica*, 14(5): 465–471, 1978.
- [22] Gideon Schwarz et al. Estimating the dimension of a model. *The annals of statistics*, 6(2):461–464, 1978.
- [23] Johan Himberg and Aapo Hyvarinen. Icasso: software for investigating the reliability of ica estimates by clustering and visualization. In *2003 IEEE XIII Workshop on Neural Networks for Signal Processing (IEEE Cat. No. 03TH8718)*, pages 259–268. IEEE, 2003.
- [24] Vince D Calhoun, Jingyu Liu, and Tülay Adalı. A review of group ica for fmri data and ica for joint inference of imaging, genetic, and erp data. *Neuroimage*, 45(1):S163–S172, 2009.
- [25] Vince D Calhoun, Tulay Adali, Godfrey D Pearlson, and James J Pekar. A method for making group inferences from functional mri data using independent component analysis. *Human brain mapping*, 14(3):140–151, 2001.
- [26] CF Beckmann, CE Mackay, N Filippini, and SM Smith. Group comparison of resting-state fmri data using multi-subject ica and dual regression. *NeuroImage*, 47:S148, 2009. ISSN 1053-8119. doi: [https://doi.org/10.1016/S1053-8119\(09\)71511-3](https://doi.org/10.1016/S1053-8119(09)71511-3). URL <http://www.sciencedirect.com/science/article/pii/S1053811909715113>. Organization for Human Brain Mapping 2009 Annual Meeting.
- [27] Markus Svensén, Frithjof Kruggel, and Habib Benali. Ica of fmri group study data. *NeuroImage*, 16(3, Part A):551 – 563, 2002. ISSN 1053-8119. doi: <https://doi.org/10.1006/ning.2002.1122>. URL <http://www.sciencedirect.com/science/article/pii/S1053811902911225>.
- [28] C.F. Beckmann and S.M. Smith. Tensorial extensions of independent component analysis for multisubject fmri analysis. *NeuroImage*, 25(1):294 – 311, 2005. ISSN 1053-8119. doi: <https://doi.org/10.1016/j.neuroimage.2004.10.043>. URL <http://www.sciencedirect.com/science/article/pii/S1053811904006378>.
- [29] Jong-Hwan Lee, Te-Won Lee, Ferenc A. Jolesz, and Seung-Schik Yoo. Independent vector analysis (iva): Multivariate approach for fmri group study. *NeuroImage*, 40(1):86 – 109, 2008. ISSN 1053-8119. doi: <https://doi.org/10.1016/j.neuroimage.2007.11.019>. URL <http://www.sciencedirect.com/science/article/pii/S1053811907010622>.
- [30] Erik Barry Erhardt, Srinivas Rachakonda, Edward J Bedrick, Elena A Allen, Tülay Adalı, and Vince D Calhoun. Comparison of multi-subject ica methods for analysis of fmri data. *Human brain mapping*, 32(12):2075–2095, 2011.

- [31] Alexandre Dizeux, Marc Gesnik, Harry Ahnine, Kevin Blaize, Fabrice Arcizet, Serge Picaud, José-Alain Sahel, Thomas Deffieux, Pierre Pouget, and Mickael Tanter. Functional ultrasound imaging of the brain reveals propagation of task-related brain activity in behaving primates. *Nature communications*, 10(1):1400, 2019.
- [32] Lim-Anna Sieu, Antoine Bergel, Elodie Tiran, Thomas Deffieux, Mathieu Pernot, Jean-Luc Gennisson, Mickaël Tanter, and Ivan Cohen. Eeg and functional ultrasound imaging in mobile rats. *Nature methods*, 12(9):831, 2015.
- [33] Charlie Demené, Mathieu Pernot, Valérie Biran, Marianne Alison, Mathias Fink, Olivier Baud, and Mickaël Tanter. Ultrafast doppler reveals the mapping of cerebral vascular resistivity in neonates. *Journal of Cerebral Blood Flow & Metabolism*, 34(6):1009–1017, 2014.
- [34] Alan Urban, Emilie Mace, Clément Brunner, Marc Heidmann, Jean Rossier, and Gabriel Montaldo. Chronic assessment of cerebral hemodynamics during rat forepaw electrical stimulation using functional ultrasound imaging. *Neuroimage*, 101:138–149, 2014.
- [35] Bruno-Félix Osmanski, Sophie Pezet, Ana Ricobaraza, Zsolt Lenkei, and Mickael Tanter. Functional ultrasound imaging of intrinsic connectivity in the living rat brain with high spatiotemporal resolution. *Nature communications*, 5:5023, 2014.
- [36] Bruno-Felix Osmanski, Claire Martin, Gabriel Montaldo, P Lanièce, Frédéric Pain, Mickaël Tanter, and H Gurden. Functional ultrasound imaging reveals different odor-evoked patterns of vascular activity in the main olfactory bulb and the anterior piriform cortex. *Neuroimage*, 95:176–184, 2014.
- [37] Claudia Errico, Bruno-Félix Osmanski, Sophie Pezet, Olivier Couture, Zsolt Lenkei, and Mickael Tanter. Transcranial functional ultrasound imaging of the brain using microbubble-enhanced ultrasensitive doppler. *NeuroImage*, 124:752–761, 2016.
- [38] Marc Gesnik, Kevin Blaize, Thomas Deffieux, Jean-Luc Gennisson, José-Alain Sahel, Mathias Fink, Serge Picaud, and Mickaël Tanter. 3d functional ultrasound imaging of the cerebral visual system in rodents. *NeuroImage*, 149:267–274, 2017.
- [39] Marion Imbault, Dorian Chauvet, Jean-Luc Gennisson, Laurent Capelle, and Mickael Tanter. Intraoperative functional ultrasound imaging of human brain activity. *Scientific reports*, 7(1):7304, 2017.
- [40] Elodie Tiran, Jérémy Ferrier, Thomas Deffieux, Jean-Luc Gennisson, Sophie Pezet, Zsolt Lenkei, and Mickaël Tanter. Transcranial functional ultrasound

- imaging in freely moving awake mice and anesthetized young rats without contrast agent. *Ultrasound in medicine & biology*, 43(8):1679–1689, 2017.
- [41] Charlie Demene, Jérôme Baranger, Miguel Bernal, Catherine Delanoe, Stéphane Auvin, Valérie Biran, Marianne Alison, Jérôme Mairesse, Elisabeth Harribaud, Mathieu Pernot, et al. Functional ultrasound imaging of brain activity in human newborns. *Science translational medicine*, 9(411):eaah6756, 2017.
- [42] Émilie Macé, Gabriel Montaldo, Stuart Trenholm, Cameron Cowan, Alexandra Brignall, Alan Urban, and Botond Roska. Whole-brain functional ultrasound imaging reveals brain modules for visuomotor integration. *Neuron*, 100(5):1241–1251, 2018.
- [43] Celian Bimbard, Charlie Demene, Constantin Girard, Susanne Radtke-Schuller, Shihab Shamma, Mickael Tanter, and Yves Boubenec. Multi-scale mapping along the auditory hierarchy using high-resolution functional ultrasound in the awake ferret. *Elife*, 7:e35028, 2018.
- [44] Charlie Demené, David Maresca, Matthias Kohlhauer, Fanny Lidouren, Philippe Micheau, Bijan Ghaleh, Mathieu Pernot, Renaud Tissier, and Mickaël Tanter. Multi-parametric functional ultrasound imaging of cerebral hemodynamics in a cardiopulmonary resuscitation model. *Scientific reports*, 8(1):16436, 2018.
- [45] Richard Rau, Pieter Kruizinga, Frits Mastik, Markus Belau, Nico de Jong, Johannes G Bosch, Wolfgang Scheffer, and Georg Maret. 3d functional ultrasound imaging of pigeons. *NeuroImage*, 183:469–477, 2018.
- [46] Kazuto Masamoto and Iwao Kanno. Anesthesia and the quantitative evaluation of neurovascular coupling. *Journal of Cerebral Blood Flow & Metabolism*, 32(7):1233–1247, 2012.
- [47] Alan Urban, Clara Dussaux, Guillaume Martel, Clément Brunner, Emilie Mace, and Gabriel Montaldo. Real-time imaging of brain activity in freely moving rats using functional ultrasound. *nature methods*, 12(9):873, 2015.
- [48] José M Soares, Ricardo Magalhães, Pedro S Moreira, Alexandre Sousa, Edward Ganz, Adriana Sampaio, Victor Alves, Paulo Marques, and Nuno Sousa. A hitchhiker’s guide to functional magnetic resonance imaging. *Frontiers in neuroscience*, 10:515, 2016.
- [49] Jingyuan E Chen and Gary H Glover. Functional magnetic resonance imaging methods. *Neuropsychology review*, 25(3):289–313, 2015.

- [50] David M Cole, Stephen M Smith, and Christian F Beckmann. Advances and pitfalls in the analysis and interpretation of resting-state fmri data. *Frontiers in systems neuroscience*, 4:8, 2010.
- [51] Martijn P Van Den Heuvel and Hilleke E Hulshoff Pol. Exploring the brain network: a review on resting-state fmri functional connectivity. *European neuropsychopharmacology*, 20(8):519–534, 2010.
- [52] Jiansong Xu, Marc N Potenza, and Vince D Calhoun. Spatial ica reveals functional activity hidden from traditional fmri glm-based analyses. *Frontiers in neuroscience*, 7:154, 2013.
- [53] Karl J Friston. Functional and effective connectivity: a review. *Brain connectivity*, 1(1):13–36, 2011.
- [54] Fangzhou Yao, Jeff Coquery, and Kim-Anh Lê Cao. Independent principal component analysis for biologically meaningful dimension reduction of large biological data sets. *BMC bioinformatics*, 13(1):24, 2012.
- [55] Jonathan D Cohen, Nathaniel Daw, Barbara Engelhardt, Uri Hasson, Kai Li, Yael Niv, Kenneth A Norman, Jonathan Pillow, Peter J Ramadge, Nicholas B Turk-Browne, et al. Computational approaches to fmri analysis. *Nature neuroscience*, 20(3):304, 2017.
- [56] Daniel S Margulies, Joachim Böttger, Xiangyu Long, Yating Lv, Clare Kelly, Alexander Schäfer, Dirk Goldhahn, Alexander Abbushi, Michael P Milham, Gabriele Lohmann, et al. Resting developments: a review of fmri post-processing methodologies for spontaneous brain activity. *Magnetic Resonance Materials in Physics, Biology and Medicine*, 23(5-6):289–307, 2010.
- [57] Andrew D Huberman and Cristopher M Niell. What can mice tell us about how vision works? *Trends in neurosciences*, 34(9):464–473, 2011.
- [58] Arun Niranjana, Isabel N Christie, Samuel G Solomon, Jack A Wells, and Mark F Lythgoe. fmri mapping of the visual system in the mouse brain with interleaved snapshot ge-epi. *Neuroimage*, 139:337–345, 2016.
- [59] Arun Niranjana, Bernard Siow, Mark Lythgoe, and Jack Wells. High-temporal-resolution bold responses to visual stimuli measured in the mouse superior colliculus. *Matters*, 3(2):e201701000001, 2017.
- [60] Anna E Mechling, Neele S Hübner, Hsu-Lei Lee, Jürgen Hennig, Dominik von Elverfeldt, and Laura-Adela Harsan. Fine-grained mapping of mouse brain functional connectivity with resting-state fmri. *Neuroimage*, 96:203–215, 2014.

- [61] Valerio Zerbi, Joanes Grandjean, Markus Rudin, and Nicole Wenderoth. Mapping the mouse brain with rs-fmri: an optimized pipeline for functional network identification. *Neuroimage*, 123:11–21, 2015.
- [62] Francesco Sforazzini, Adam J Schwarz, Alberto Galbusera, Angelo Bifone, and Alessandro Gozzi. Distributed bold and cbv-weighted resting-state networks in the mouse brain. *Neuroimage*, 87:403–415, 2014.
- [63] Jingyuan E Chen and Gary H Glover. Functional magnetic resonance imaging methods. *Neuropsychology review*, 25(3):289–313, 2015.
- [64] Arthur W Toga and Paul M Thompson. The role of image registration in brain mapping. *Image and vision computing*, 19(1-2):3–24, 2001.
- [65] Jean-François Cardoso. Dependence, correlation and gaussianity in independent component analysis. *Journal of Machine Learning Research*, 4(Dec):1177–1203, 2003.
- [66] Daniel S Margulies, Joachim Böttger, Xiangyu Long, Yating Lv, Clare Kelly, Alexander Schäfer, Dirk Goldhahn, Alexander Abbushi, Michael P Milham, Gabriele Lohmann, et al. Resting developments: a review of fmri post-processing methodologies for spontaneous brain activity. *Magnetic Resonance Materials in Physics, Biology and Medicine*, 23(5-6):289–307, 2010.
- [67] Srinivas Rachakonda, Eric Egolf, Nicolle Correa, and Vince Calhoun. Group ica of fmri toolbox (gift) manual. *Dostupné z*, 10 2010.
- [68] Wei Du, Sai Ma, Geng-Shen Fu, Vince D Calhoun, and Tülay Adalı. A novel approach for assessing reliability of ica for fmri analysis. In *2014 IEEE international conference on acoustics, speech and signal processing (Icassp)*, pages 2084–2088. IEEE, 2014.
- [69] Nicolle Correa, Tülay Adalı, and Vince D Calhoun. Performance of blind source separation algorithms for fmri analysis using a group ica method. *Magnetic resonance imaging*, 25(5):684–694, 2007.
- [70] Jari Miettinen, Klaus Nordhausen, and Sara Taskinen. fica: Fastica algorithms and their improved variants. *R J*, 10(2):148–158, 2018.
- [71] Jari Miettinen, Klaus Nordhausen, Hannu Oja, and Sara Taskinen. Deflation-based fastica with adaptive choices of nonlinearities. *IEEE Transactions on Signal Processing*, 62(21):5716–5724, 2014.
- [72] Azzouz Dermoune and Tianwen Wei. Fastica algorithm: Five criteria for the optimal choice of the nonlinearity function. *IEEE transactions on signal processing*, 61(8):2078–2087, 2013.

- [73] Ulykbek Kairov, Laura Cantini, Alessandro Greco, Askhat Molkenov, Urszula Czerwinska, Emmanuel Barillot, and Andrei Zinovyev. Determining the optimal number of independent components for reproducible transcriptomic data analysis. *BMC genomics*, 18(1):712, 2017.
- [74] Ahmed Abou-Elseoud, Tuomo Starck, Jukka Remes, Juha Nikkinen, Osmo Tervonen, and Vesa Kiviniemi. The effect of model order selection in group pica. *Human brain mapping*, 31(8):1207–1216, 2010.
- [75] Dietmar Cordes and Rajesh R Nandy. Estimation of the intrinsic dimensionality of fmri data. *Neuroimage*, 29(1):145–154, 2006.
- [76] Aapo Hyvärinen. Testing the ica mixing matrix based on inter-subject or inter-session consistency. *NeuroImage*, 58(1):122–136, 2011.
- [77] Mustafa S Salman, Yuhui Du, Dongdong Lin, Zening Fu, Alex Fedorov, Eswar Damaraju, Jing Sui, Jiayu Chen, Andrew R Mayer, Stefan Posse, et al. Group ica for identifying biomarkers in schizophrenia: ‘adaptive’ networks via spatially constrained ica show more sensitivity to group differences than spatio-temporal regression. *NeuroImage: Clinical*, 22:101747, 2019.
- [78] Kelly H Zou, Simon K Warfield, Aditya Bharatha, Clare MC Tempany, Michael R Kaus, Steven J Haker, William M Wells III, Ferenc A Jolesz, and Ron Kikinis. Statistical validation of image segmentation quality based on a spatial overlap index1: scientific reports. *Academic radiology*, 11(2):178–189, 2004.
- [79] Georgios C Papadopoulos and John G Parnavelas. Distribution and synaptic organization of dopaminergic axons in the lateral geniculate nucleus of the rat. *Journal of Comparative Neurology*, 294(3):356–361, 1990.
- [80] Rachel Aronoff, Ferenc Matyas, Celine Mateo, Carine Ciron, Bernard Schneider, and Carl CH Petersen. Long-range connectivity of mouse primary somatosensory barrel cortex. *European Journal of Neuroscience*, 31(12):2221–2233, 2010.
- [81] Rafał Czajkowski, Balaji Jayaprakash, Brian Wiltgen, Thomas Rogerson, Mikael C Guzman-Karlsson, Alison L Barth, Joshua T Trachtenberg, and Alcino J Silva. Encoding and storage of spatial information in the retrosplenial cortex. *Proceedings of the National Academy of Sciences*, 111(23):8661–8666, 2014.
- [82] Dmitry Lyamzin and Andrea Benucci. The mouse posterior parietal cortex: anatomy and functions. *Neuroscience research*, 2018.

- [83] Muwei Li, Allen T Newton, Adam W Anderson, Zhaohua Ding, and John C Gore. Characterization of the hemodynamic response function in white matter tracts for event-related fmri. *Nature communications*, 10(1):1140, 2019.
- [84] Pierre LeVan, Louise Tyvaert, Friederike Moeller, and Jean Gotman. Independent component analysis reveals dynamic ictal bold responses in eeg-fmri data from focal epilepsy patients. *Neuroimage*, 49(1):366–378, 2010.
- [85] R Matthew Hutchison, Thilo Womelsdorf, Elena A Allen, Peter A Bandettini, Vince D Calhoun, Maurizio Corbetta, Stefania Della Penna, Jeff H Duyn, Gary H Glover, Javier Gonzalez-Castillo, et al. Dynamic functional connectivity: promise, issues, and interpretations. *Neuroimage*, 80:360–378, 2013.
- [86] Elena A Allen, Eswar Damaraju, Sergey M Plis, Erik B Erhardt, Tom Eichele, and Vince D Calhoun. Tracking whole-brain connectivity dynamics in the resting state. *Cerebral cortex*, 24(3):663–676, 2014.
- [87] Vince Daniel Calhoun, T Adali, MC Stevens, KA Kiehl, and James J Pekar. Semi-blind ica of fmri: A method for utilizing hypothesis-derived time courses in a spatial ica analysis. *Neuroimage*, 25(2):527–538, 2005.
- [88] Kenneth A Norman, Sean M Polyn, Greg J Detre, and James V Haxby. Beyond mind-reading: multi-voxel pattern analysis of fmri data. *Trends in cognitive sciences*, 10(9):424–430, 2006.
- [89] Ella Bingham and Aapo Hyvärinen. A fast fixed-point algorithm for independent component analysis of complex valued signals. *International journal of neural systems*, 10(01):1–8, 2000.